POLYMERS AS DIRECTING AGENTS FOR MOTIONS OF CHEMICAL AND BIOLOGICAL SPECIES

BY

NIHAN YONET TANYERI

DISSERTATION

Submitted in partial fulfillment of the requirements
for the degree of Doctor of Philosophy in Materials Science and Engineering
in the Graduate Collage of the
University of Illinois at Urbana-Champaign, 2011

Urbana, Illinois

Doctoral Committee:

Professor Paul V. Braun, Chair and Director of Research
Professor Jennifer A. Lewis
Professor Robert M. Clegg
Assistant Professor Jianjun Cheng

ABSTRACT

This thesis involves descriptions of solid surface modifications with various polymeric materials which were used as a guiding agent for motion of chemical and biological species.

Quasi-two dimensional poly(oligoethylene glycol) acrylate polymer brush based molecular conduits have been designed with the goal of regulating and controlling the diffusive transport of molecular, e.g. organic dyes, and ionic species, e.g. $AuCl_4^-$, and Cu^{2+} ions, along predefined 2-D pathways. The transport of these chemical species has been examined by both fluorescence and dark field microscopy. The polymer brushes were formed through microcontact printing of an initiator, followed by surface-initiated Atom Transfer Radical Polymerization (SI-ATRP). SI-ATRP enables both 2-D patterning with a resolution of about 1 micrometer, and control over the resultant polymer brush thickness (which was varied from 10-100 nm). A hydrophilic poly(oligoethylene glycol) acrylate brushe was selected because of its potential to dissolve a wide range of hydrophilic species. The transport of fluorescent species can be directly followed. A non-lithographic fabrication method was developed for μfluidic devices used in the diffusion studies. Singular channel μfluidic device was utilized to study the directed organic dye diffusion. The $AuCl_4^-$, and Cu^{2+} ion transport was studied by designing molecular devices with two μfluidic channels. We have demonstrated that the various species of interest diffuse much more rapidly along the predefined pathway than along the bare (polymer brush free) regions of the substrate, demonstrating that diffusive conduits for molecular transport can indeed be formed.

The protein resistance of poly(*N*-isopropylacrylamide) (PNIPAM) brushes grafted from silicon wafers was investigated as a function of the chain molecular weight, grafting density, and temperature. Above the lower critical solution temperature (LCST) of 32°C, the collapse of the water swollen chains, determined by ellipsometry, depends on the grafting density and

molecular weight. Ellipsometry, radio assay, and fluorescence imaging demonstrated that, below the LCST, the brushes repel protein as effectively as oligoethylene oxide terminated monolayers. Above 32°C, very low levels of protein adsorb on densely grafted brushes, and the amounts of adsorbed protein increase with decreasing brush grafting densities. Brushes that do not exhibit a collapse transition also bind protein, even though the chains remain extended above the LCST. These findings suggest possible mechanisms underlying protein interactions with end-grafted PNIPAM brushes.

3D porous materials on solid surfaces were built to mimic the corneal basement membrane so that we can monitor direction of the corneal epithelia cells behaviors as the surface topography changes. We have used colloidal crystal templating approach to build the 3D porous structures. Polystyrene (PS) colloids were crystallized in a flow cell. The crystals were filled with acrylamide precursor (including photoinitiator, crosslinker) in the oxygen free aqueous solution. After polymerization of acrylamide under UV exposure, PS colloids were dissolved in chloroform. Thus, 3D porous polyacrylamide hydrogels have been fabricated. The various pore sizes at the 3D porous surface have been obtained by using PS colloids with the colloid diameters ranging from 450 nm to 4 μm. Human corneal epithelial cell growth, morphology change and adhesion studies have been conducted on the porous polyacrylamide scaffolds. The effect of pore size on human corneal epithelial cell function has been investigated.

To my parents, my husband, and my daughter

ACKNOWLEDGEMENTS

I would like to thank my advisor, Professor Paul V. Braun, for his guidance, support and patience throughout my graduate education. I am so grateful to have his continuous encouragement. I must say he is an exceptional personality in my life and I greatly appreciate having Paul as my advisor.

I would like to acknowledge my committee members, Professor Robert Clegg, Professor Jennifer Lewis, and Professor Jianjun Cheng for contributing their experiences and time. I would like to thank Professor Deborah E. Leckband for her insights, support and encouragement for the past two years. I would also like to thank Professor Paul F. Nealey for his support in the collaboration of the cell studies with the 3D porous hydrogels.

I am grateful to Dr. Huilin Tu and Rachel C. Evans for their advice and assistance at my early time in the lab. I am indebted to Dr. Mathew C. George, Dr. Margaret Shyr, Dr. Robert Barry, Dr. Xindi Yu, Dr. and Dara V. Gough for their valuable discussions and advices. I would also like to acknowledge Dr. Changying Xue and Dr. Sara J. Liliensiek for their help in the collaborations of the protein adsorption studies on PNIPAM brushes and the cell growth studies on the porous biomaterials.

I must thank Corissa Lee, Aaron C. Jackson, Austin Pickett and Sidhartha Gupta for being a great and enjoyable lab mates as “Beckman folks”.

Finally, I would especially like to thank my parents and my sisters for their endless support and encouragement throughout the years that they have given me. I am very grateful to my lovely husband, Melikhan, for having him in my life, being with me all the time, continuously feeling his love, support and patience, and his invaluable efforts to motivate me whenever I needed for the past five years that we spent together.

TABLE OF CONTENTS

CHAPTER 1

INTRODUCTION

1.1 Introduction

This thesis ties three major research projects under one objective which is to direct the motion of chemical and biological species on solid surfaces for the application of nanoscience and biotechnology. This goal has been achieved by designing “smart” surfaces with polymeric materials that can tune the motion of target species towards the desired directions.

There has been great effort to investigate the diffusive characteristics of various kinds of chemical species on solid surfaces. However these studies have mainly focused on the diffusion mechanisms, kinetics, and thermodynamics of the proposed systems. To the best of our knowledge, there has not been any research that has demonstrated “smart” surface designs which are capable of directing the diffusive transportation. It is scientifically and technologically very exciting to guide chemical species transportation which is important for a number of applications like surface-directed separation, chemical and biological sensing, and spatio-temporally controlled material gradients for nanoscaled reactions. One part of this thesis is centered upon fabrication of “smart” functional surfaces with the ability to create chemical gradients by probing the diffusion of chemical entities through the patterns of polymer brushes and emphasizes application of these chemical gradients in generation of spatio-temporally programmed nanoreactions.

Surface modifications with the intention to direct biomolecular motions provide useful coatings that can selectively guide the adhesion of biomolecules like membrane proteins and their release from the surface under external stimuli. Such “smart” surfaces, thus, promote the cell adhesion to generate singular cell-sheets which can be easily removed from the surface in the presence of a trigger. Successful implementation of this technology in tissue engineering

and regenerative medicine allows researchers to reconstruct damaged tissues. The chemical composition of the engineered surface is the key element for the responsive materials. In the second part of this thesis, the focus will be on the surface designs of responsive chemistries and their capability to direct biomolecular adhesion under external stimuli.

The fundamental concepts connected with tissue engineering and regenerative medicine take researcher's interest to the synthetic 3D models because they are better examples to represent tissue architecture. 3D scaffold designs are very crucial in directing cells to synthesize and maintain new tissues. This highly motivates us to focus on developing 3D porous "smart" biomaterials and investigating cells behavior response as a function of surface topography.

Three major routes have been followed to modify solid surfaces with "smart" materials. The first route is to utilize patterning technique. The second is to alter the surface composition with responsive chemistries, and the last one is to fabricate 3D constructs with defined surface topographies.

1.2 Surface Patterning with Functional Polymer Brushes

Polymer brushes, mostly known as surface-tethered macromolecules, are long chain polymers that are attached to a surface from one end through a strong covalent bonding. Their covalently tethered feature makes them very stable in various experimental conditions. Besides, their chain conformation is quite different than polymers in bulk. The level of polymer grafting density plays a key role in the determination of the polymer brush conformation. At low grafting densities, they will have "mushroom" conformation whose coil dimension is very close to ungrafted free chains. As the grafting density increases, polymer chains will stretch away from the surface and will form "brush" like structures.

There are three major routes to grow surface tethered polymer brushes from a surface: "grafting to", "grafting from" and grafting via surface attached monomers (Figure 1. 1) [1]. In the "grafting to" method, polymer chains whose one end is a reactive group are attached to the

surface as a result of the reaction between the polymer end-group and the surface. This method has some limitations in generating high grafting density polymer brushes. The “grafting from” approach requires functional surfaces with initiator molecules. The polymer chains, then, grow from each individual initiator molecule. It is very easy to achieve high grafting density polymer brushes with this technique. Finally, polymer brushes can be grown from a surface where monomers are immobilized. This method is very similar to “grafting from” approach in that each polymer chain grows from the surface. However, the final method is limited on finding a large monomer library that is compatible with the surface reaction. This thesis primarily involves with the polymer brushes that are prepared by “grafting from” approach.

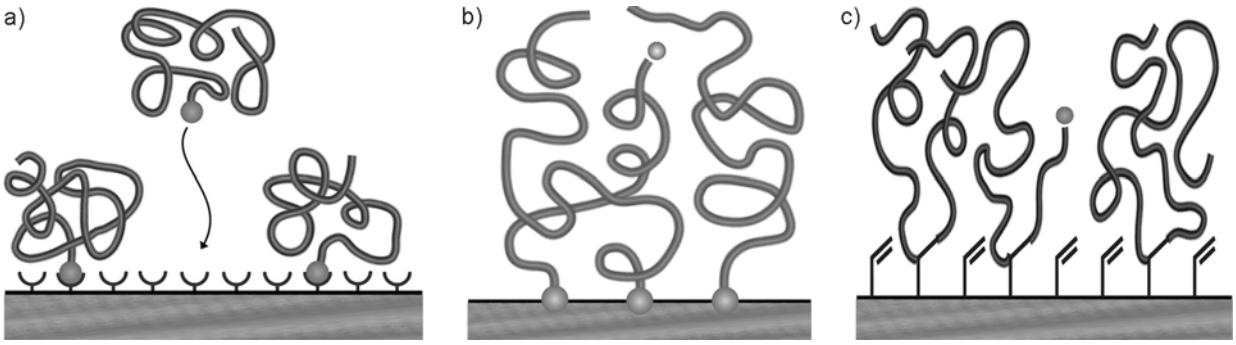

Figure 1. 1. Schematic representation of surface tethered polymer brushes via (a) “grafting to”, (b) “grafting from”, and (c) grafting via surface-bound monomer approach (Adopted from ref. [1]).

Patterned polymer brushes have been widely used in many applications ranging from microelectronics to biomaterials [2-4]. “Top-down” or “bottom-up” fabrication strategies can summarize the patterned polymer brush formation techniques. “Top-down” approaches are based on removing selected polymer brush regions from the surface whereas “bottom-up” methods include surface functionalization with patterns of initiator following surface-initiated controlled radical polymerization. The following section discusses patterning strategies of surface tethered polymer brushes.

1.2.1 Microcontact Printing

Microcontact printing (μCP) is a very efficient tool to pattern large areas with a submicron resolution [5, 6]. Functional surfaces with patterned polymer brushes can be obtained by either directly printing the initiator onto the surface (Figure 1. 2) or printing a passive pattern from which is not capable of growing polymer brushes and then backfilling unprinted regions with the initiator [7-10]. This technique is applicable onto many different substrates including silicon wafer, gold, and various polymer surfaces [11-14] and very cost-efficient method compared to other patterning techniques.

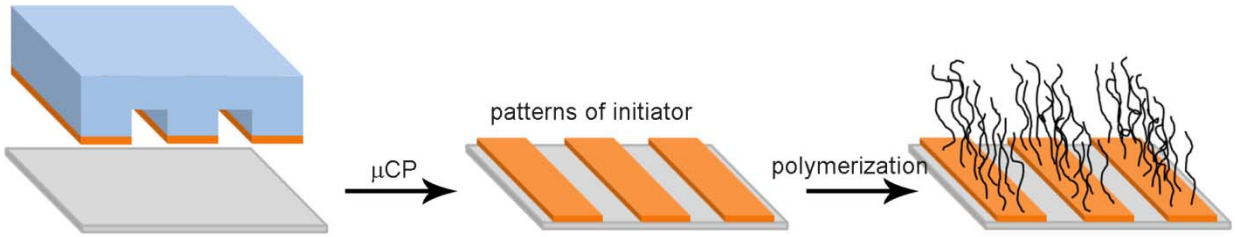

Figure 1. 2 Illustration of patterned polymer brush growth via microcontact printing (μCP) technique.

1.2.2 Patterning with Electron Beam and UV Irradiation

The fundamentals of these methods are very similar in that electron beam or UV irradiation is used to decompose the surface immobilized initiator from a mask and polymer brushes will only grow in areas that are not exposed to electron beam or UV light (Figure 1. 3) [15, 16]. Alternatively, UV light exposure onto the surface bound initiator facilitates photolytic activation of the initiator and polymer brush patterns are generated from the activated initiator regions [17, 18].

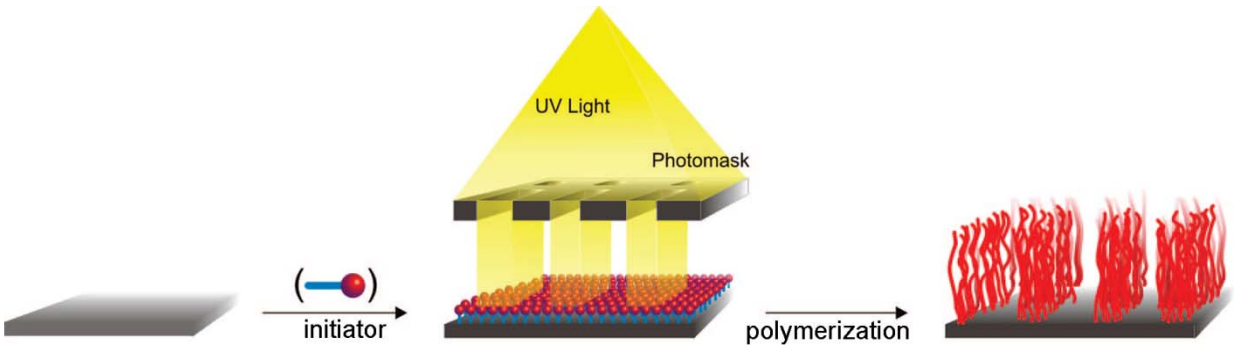

Figure 1. 3. Patterned polymer brush formation by assistance of UV light irradiation (Adopted from ref. [16]).

1.2.3 Nanoimprint Lithography

In this method, a patterned thin film of an initiator functionalized copolymer is fabricated by nanoimprint lithograpy. Once the residual polymer is removed from the surface by oxygen plasma, polymer brushes are grown from the imprinted regions [19].

1.2.4 Scanning Probe Microscopy-Based Patterning

Surface patterning with polymer brushes via scanning probe microscope (SPM) assisted methods provide patterns with a very high spatial resolution as small as 20 nm [20]. The major drawback of this technology is its very long process duration and difficulty to apply to large areas. SPM assisted patterning is based on two strategies. One is to use SPM as a nanomechanical tool to generate trenches on the surface and grow polymers from backfilled regions [21]. In the second approach, SPM directly writes the initiator molecules on the surface and polymer brushes are formed from the patterns of initiators [9].

1.3 Surface Modification with Stimuli Responsive Polymers

Significant interests of the current studies in polymer brushes has been attributed to responsive polymers for the “smart” surfaces in which responsiveness of polymer brushes refers to changes of polymer conformation under external stimuli such as temperature, electric field,

solvent, light, magnetic field, and pH [22-29]. The stimuli responsive polymer brushes can be grouped in two main categories: responsive polymer brushes with (1) switching surface wettability and (2) mechanoactuation and transduction features. The following section will briefly touch on these “smart” surface designs.

1.3.1 Responsive Polymer Brushes with Switching Surface Wettability

Temperature-responsive polymer brushes based on poly(*N*-isopropylacrylamide) (PNIPAM), which is one of the most suitable surface chemistries for biological applications because its lower critical solution temperature (LCST) is close to physiological temperature (32°C), have been studied [30, 31]. The response mechanism of PNIPAM in the case of a temperature change works as follows. PNIPAM is hydrophilic below its LCST and swells in water. Once the temperature of the aqueous environment is increased above its LCST which is accepted as 32°C, PNIPAM undergoes conformational change and collapse due to its more hydrophobic nature. Cell-sheet engineering takes the advantages of temperature-dependent switching characteristics of PNIPAM brushes to direct continuous cell-sheets formation. Cells adhere to PNIPAM surface above 32°C on which the hydrophobic surface supports cells’ adhesion and singular layer of cells is removed from the surface as the temperature is decreased below 32°C (Figure 1. 4).

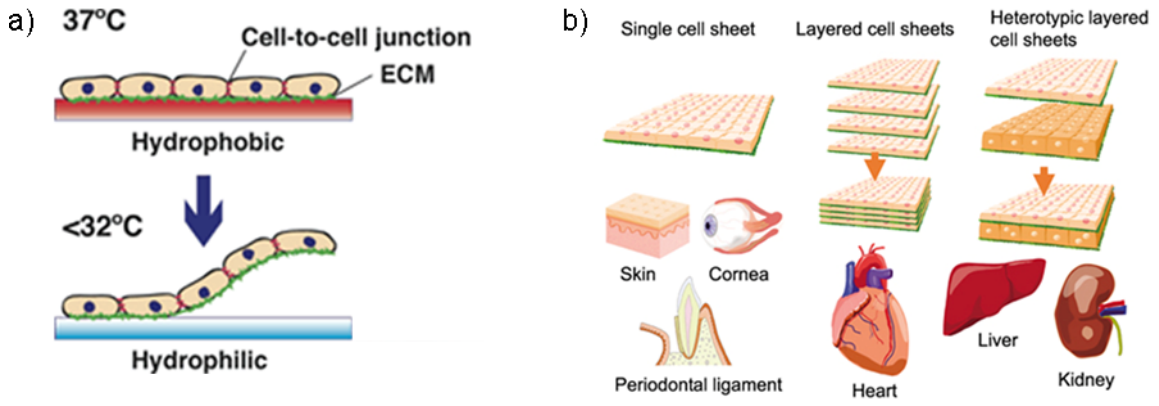

Figure 1. 4. (a) Schematic representation of cell-sheet engineering application of temperature-responsive PNIPAM brushes. (b) Examples of tissue reconstructions using cell-sheet engineering (Both illustrations are adopted from ref. [32]).

PNIPAM brushes can be grown from gold, silica or polymer surfaces [33-35] and surface-initiated controlled radical polymerization technique brings a good control on the chemical composition of the PNIPAM brushes. It is very important to be able to regulate the composition of the PNIPAM brushes for “smart” surfaces because the general transition of PNIPAM under temperature changes is believed to be dependent upon the surface composition such as grafting density, molecular weight, and the polydispersity index [33, 36-40]. Accordingly, directing the adhesion/release mechanism of the biological species on such surfaces will be affected by these surface parameters.

Polymer brushes can undergo wettability switch with photolytic stimuli. For instance, the conformation of the spiropyran group in a spiropyran-containing polymer brush can be reversibly switched by a UV light exposure from the nonpolar spyropyran form to the relatively more polar merocyanin form [41]. Visible light will reverse this process and the polymer brush returns to its original hydrophobic nature. Similar to the photo-induced wettability switch, pH or ionic strength of the aqueous environment also leads to a change in wettability of the polymer brushes which are known as polyelectrolyte brushes. Polyelectrolyte brushes are composed of ionizable pendant groups or weakly acidic or basic groups. Any change in the pH of the environment brings a change in the hydrodynamic volume of the polymer chain [42]. Likewise, polyelectrolyte

brush conformation can be affected by ionic strength change. As ionic strength increases, the electrostatic interactions will lead to collapsed conformation of the polyelectrolyte brushes [43].

1.3.2 Responsive Polymer Brushes with Mechano-action and Transduction Properties

In living systems, biological motors transform chemical energy to mechanical motions and transduce mechanical forces to biological signals. Significant number of research has been inspired by this mechanism and focused on “smart” surface designs which are capable of stimulating the similar transduction. Microcantilevers actuated by polymer brushes are one of the examples. Grafting end-tethered stimuli responsive polymer brushes onto a microcantilever allows bending the cantilever and to be able to detect surface stress under external stimuli which leads to changes in cantilever deflection. One can envision the possible variation in polymer brush chemistry that can be incorporated into microcantilevers. Solvent, pH, and ionic strength responsive polymer brushes are a few examples that demonstrated the actuation of cantilevers [44, 45].

Mechanotransduction in biological system is a concept that cells convert mechanical stimulus into an electric signal. This idea was implemented in a rudimentary mechanotransduction system in which a pH sensitive dye molecule was adsorbed in pH sensitive polymer brushes [46]. As the mechanical force is applied across the polymer film, the local ionic strength within the brush increases. Increased local ion concentration leads to a change in the degree of dissociation of the pH-sensitive dye molecules and a change in the UV-spectrum is observed.

1.4 Surface Decoration with 3D Functional Materials

Advances in fabrication techniques have opened new avenues in manufacturing three-dimensional (3D) micro- and nano-scaled periodic structures. Tissue engineering is one of the disciplines that combine the advanced macrofabrication techniques with the appropriate

chemistries to construct complex 3D architectures which mimic the in vivo tissue environment. Colloidal self assembly, direct write assembly, interference lithography, two photon polymerization, conventional lithography, and holographic lithography are just some of the widely used techniques utilized to form 3D functional structures [47-53]. Each technique has its own advantages and superiority over one another in the structural control, regularity, and reproducibility. However, this thesis mainly involves with the colloidal assemblies for building 3D porous biomaterials and their implementation in revealing the interaction between the surface structure of the porous materials and cells response.

1.4.1 Colloidal Crystal Assembly

Colloidal crystals are comprised of regular and periodic arrays of highly monodisperse spherical dielectric materials. Many research topics involving with physical problems such as phase transition, kinetics of crystallization, and physics of nucleation and growth process have been studied by colloidal crystal models [54-56]. The unique properties of colloidal crystals make them useful in a range of applications in optics, as chemical sensors, in data storage [57-59].

There are several different ways to build colloidal crystal assemblies. The simplest one is the sedimentation method where colloidal particles settle down onto vacancies in the colloid solution. Apart from its simplicity, this method does not exhibit a good control over the crystallization process. Another way to crystallize colloids is spin coating [60]. This method employs very high concentration of colloid solutions onto a substrate and high spinning rate. Solvent of the colloidal solution evaporates and colloids pack via spinning. This method is very practical to assemble colloids on a large scale. However, deep crack formation in the crystals is the major problem. In an alternative method, colloidal crystallization is driven by solvent evaporation on a substrate where colloids form a layer at the meniscus via solvent flow (Figure 1. 4) [61]. Crystallization continues by building layers over each layer as the solvent evaporates.

Even though this method produces much uniform crystals, it is limited with smaller sized colloids.

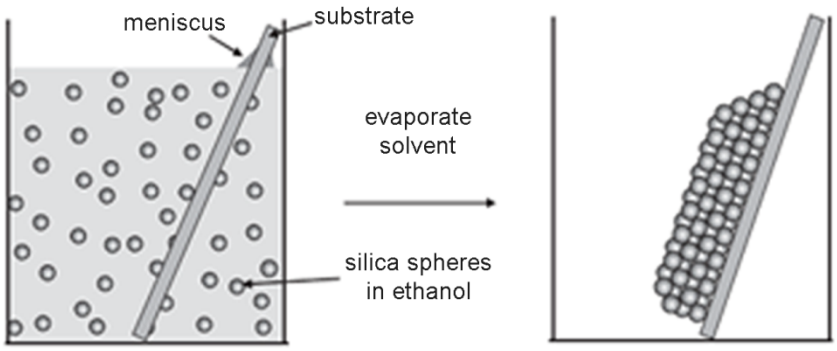

Figure 1. 5. Vertical deposition method of colloids to form monodisperse colloidal crystal (Adopted from ref. [61]).

Colloidal crystals with a very high quality and well controlled crystal thickness can be obtained by flow cell assembly method [62]. This technique consists of a spacer polymer film (Mylar film) in between two glass slides (Figure 1. 6). Colloid solution flows through a volume at the interface between the spacer and the glass slides as liquid pass through but colloids cannot. This leads colloid particles to start crystallizing at the edge of the spacer and the crystal growth continues as more colloids pack towards the inner part of the flow cell. Crystallization grows as long as the flow of the colloid solution continues but very gentle external vibration will help colloids packing more efficiently.

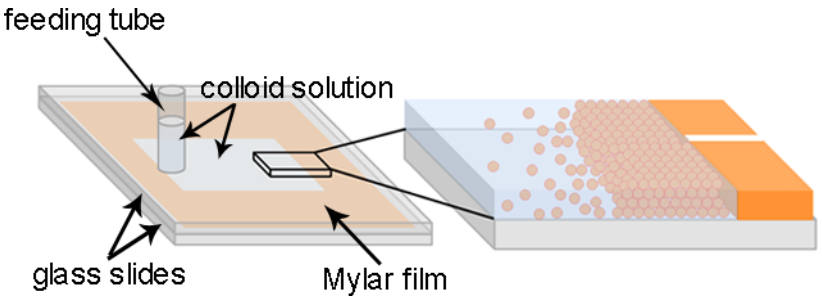

Figure 1. 6. Schematic illustration of the flow cell assembly for colloidal crystallization.

Colloidal crystal assemblies have been used as templates for generating their inverted structures. There has been significant number of efforts which were benefited from the inverted structures of colloidal crystals for tissue engineering [63-65]. In general, artificially synthesized

hydrogel scaffolds are design such that they provide mechanical support for cells to maintain structural integrity. They should also be highly porous with high surface area to increase the number of cells integrated in the structure. Therefore, hydrogel scaffolds made by inverted colloidal structures are one of the best local environments for cell growth and tissue engineering (Figure 1. 7). Inverted colloidal crystal hydrogel scaffolds provide an ordered geometry which is an important factor for cell signaling in 3D [66, 67].

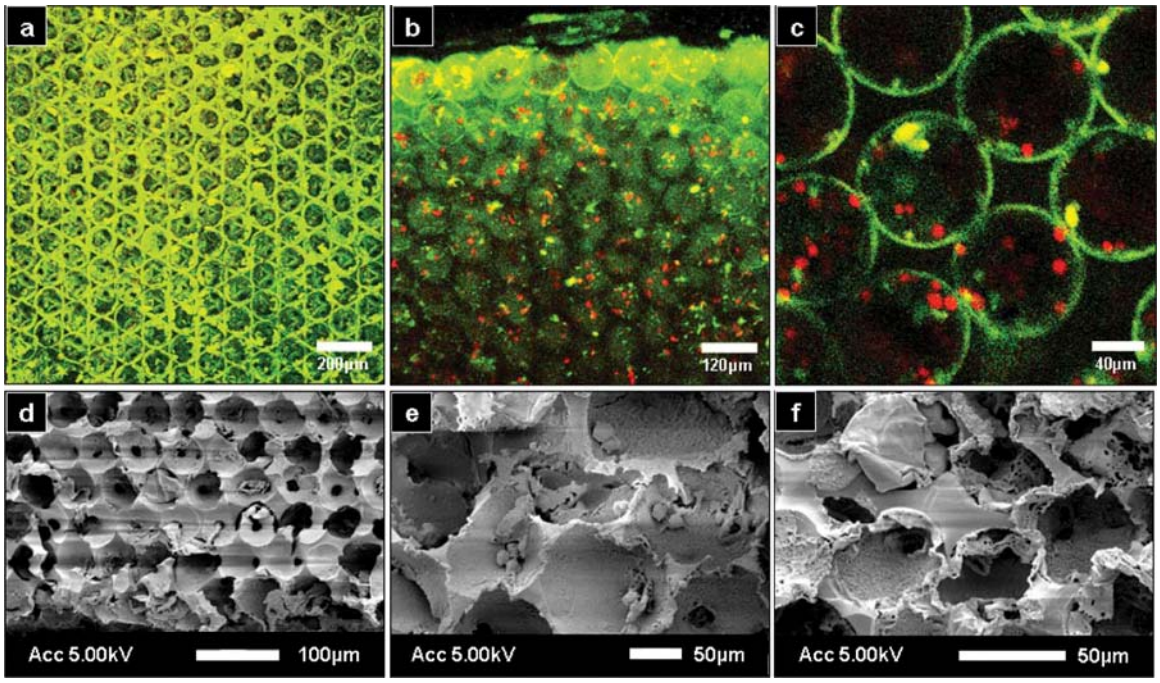

Figure 1. 7. Cross-sectional confocal images (a-c) of inverse colloidal crystal scaffold with thymic epithelial cells (green) and monocytes (red). Cross-sectional SEM images of (d) inverted colloidal crystal, (e) monocytes and (f) thymic epithelial cells in the scaffold (Adopted from ref. [66]).

We are interested in investigating how surface topography of porous synthetic biomaterials alters the cell function. Recent studies have demonstrated that topographic features on surfaces influence cell behavior. Typically studied surface features are grooves and ridges with a regular and repeating patterns. Generally, cytoskeleton elements known as actin and microtubules align along the wall and edges (Figure 1. 8) [68-70]. It was revealed with other studies that depth of the features is more critical than the width size in determining cell orientation [71-73]. As shown in Figure 1. 8d, the lamelipodia can contact with the floor of the

grooves. These findings highly motivated us to fabricate 3D porous hydrogels with surface porosity which is much smaller than the cell dimension via colloidal crystal templating and we focused on understanding cell functions as a function of pore size at the surface of the porous biomaterials.

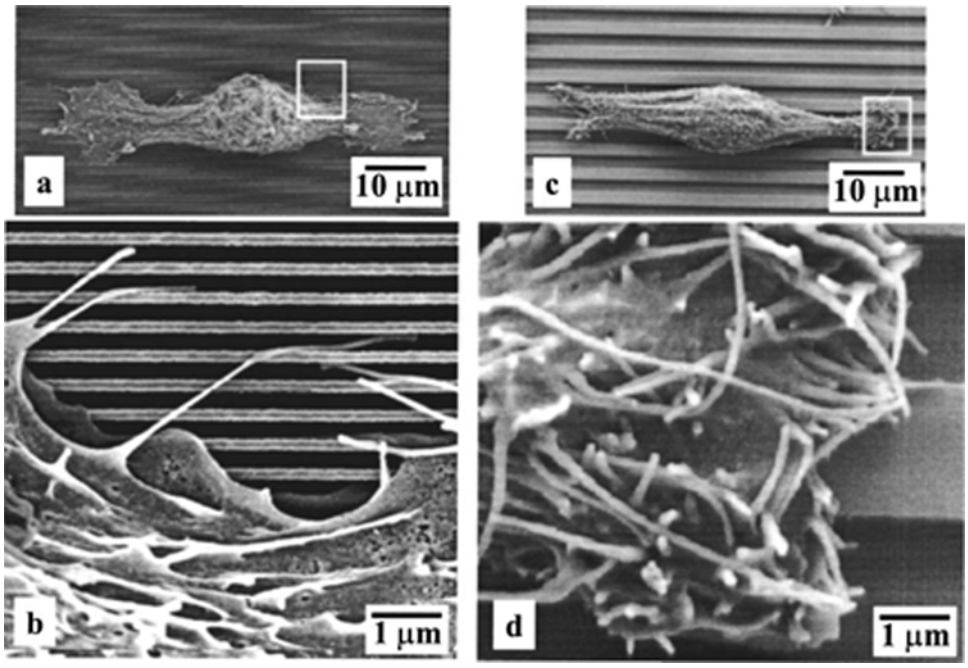

Figure 1. 8. SEM images of human corneal epithelial cells guided by surface topography. Feature sizes are (a-b) 70 nm wide ridges on a 400 nm pitch and (c-d) 1900 nm wide ridges on a 4000 nm pitch (Adopted from ref. [73]).

1.5 References

1. Advincula R. C., Brittain W. J., Caster K. C., Ruhe J., Polymer Brushes: Synthesis, Characterization, Applications (John Wiley & Sons, New York, 2004).
2. Zhao, B., Brittain, W. J., Prog. Polym. Sci., 200, 25, 677.
3. Jones, D. M., Smith, J. R., Huck, W. T. S., Alexander, C., Adv. Mater., 2002, 14, 1130.
4. Werne T. A. V., Germack D. S., Hagberg E. C., Sheares V. V., Hawker C. J., Carter K. R., J. Am. Chem. Soc., 2003, 125, 3831.
5. Kumar, A., Whitesides, G. M., Appl. Phys. Lett., 1993, 63, 2002.
6. Xia, Y., Whitesides, G. M., Angew. Chem. Inter. Ed., 1998, 37, 550.

7. Jones, D. M., Huck, W. T. S., AdV. Mater., 2001, 13, 1256.

8. Osborne, V. L., Jones, D. M., Huck, W. T. S., Chem. Commun., 2002, 1838.

9. Ma, H., Hyun, J., Stiller, P., Chilkoti, A., AdV. Mater., 2004, 16, 338.

10. Edmondson, S., Vo, C.-D., Armes, S. P., Unali, G.-F., Macromolecules, 2007, 40, 5271.

11. Benetti, E. M., Zapotoczny, S., Vancso, G. J., Adv. Mater., 2007, 19, 268.

12. Farhan, T., Huck, W. T. S., Eur. Polym. J., 2004, 40, 1599.

13. Tu, H., Heitzman, C. E., Braun, P. V., Langmuir, 2004, 20, 8313.

14. Jung, J., Kim, K. W., Na, K., Kaholek, M., Zauscher, S., Hyun, J., Macromol. Rapid Commun., 2006, 27, 776.

15. Maeng, I. S., Park, J. W., Langmuir, 2003, 19, 4519.

16. Tugulu, S., Harms, M., Fricke, M., Volkmer, D., Klok, H.-A., Angew. Chem., Int. Ed., 2006, 45, 7458.

17. Higashi, J., Nakayama, Y., Marchant, R. E., Matsuda, T., Langmuir, 1999, 15, 2080.

18. Nakayama, Y., Matsuda, T., Langmuir, 1999, 15, 5560.

19. Genua, A., Alduncı´n, J. A., Pomposo, J. A., Grande, H., Kehagias, N., Reboud, V., Sotomayor, C., Mondragon, I., Mecerreyes, D., Nanotechnology, 2007, 18, 215301.

20. Zapotoczny, S., Benetti, E. M., Vancso, G. J., J. Mater. Chem., 2007, 17, 3293.

21. Kaholek, M., Lee, W.-K., LaMattina, B., Caster, K. C., Zauscher, S., Nano Lett., 2004, 4, 373.

22. Gutowska, A., Bae, Y. H., Jacobs, H., Feijen, J., Kim, S. W., Macromolecules, 1994, 27, 4167-4175.

23. Asaka, K., Oguro, K. J., Electroanal. Chem., 2000, 480, 186-198.

24. Ionov, L., Sidorenko, A., Stamm, M., Minko, S., Zdyrko, B., Klep, V., Luzinov, I., Macromolecules, 2004, 37, 7421-7423.

25. Edmondson, S., Osborne, V. L., Huck, W. T. S., Chem. Soc. Rev., 2004, 33, 14-22.

26. Yuan, W. F., Jiang, G. Y., Wang, J. X., Wang, G. J., Song, Y. L., Jiang, L., Macromolecules, 2006, 39, 1300-1303.

27. Xulu, P. M., Filipcsei, G., Zrinyi, M., Macromolecules, 2000, 33, 1716-1719.

28. Casalbore-Miceli, G., Chen, Y. S., Girotto, E. M., Li, Y., Rinaldi, A. W., Yang, M. J., Zanelli, A., Sens. Actuators B, 2006, 119, 577-582.

29. Feil, H., Bae, Y. H., Feijen, J., Kim, S. W., Macromolecules, 1992, 25, 5528-5530.

30. Ohki, T., Yamato, M., Murakami, D., Takagi, R., Yang, J., Namiki, H., Okano, T., Takasaki, K., Gut, 2006, 55, 1704-1710.

31. Yaji, N., Yamato, M., Yang, J., Okano, T., Hori, S., Biomaterials, 2009, 30, 797-803.

32. Shimizu, T. , Yamato, M., Kikuchi, A., Okano, T., Biomaterials, 2003, 24, 13, 2309.

33. Balamurugan, S., Mendez, S., Balamurugan, O'Brien II, S., M. J., Lopez, G. P., Langmuir, 2003, 19, 2545.

34. Cunliffe, D., Alarcon, C. d. l. H., Peters, V., Smith, J. R., Alexander, C., Langmuir, 2003, 19, 2888.

35. Yamada, N., Okano, T., Sakai, H., Karikusa, F., Sawasaki, Y., Sakurai, Y., Makromol. Chem., Rapid Commun., 1990, 11, 571.

36. Plunkett, K. N., Zhu, X., Moore, J. S., Leckband, D. E., Langmuir, 2006, 22, 4259-4266.

37. Zhulina, E. B., Borisov, O. V., Pryamitsyn, V. A., Birshtein, T. M., Macromolecules, 1991, 24, 140.

38. Shan, J., Chen, J., Nuopponen, M., Tenku, H., Langmuir, 2004, 20, 4671.

39. Baulin, V. A., Zhulina, E. B., Halperin, A., J. Chem. Phys., 2003, 119, 10977.

40. Yim, H., Kent, M. S., Huber, D. L., Satija, S., Majewski, J., Smith, G. S., Macromolecules, 2003, 36, 5244.

41. Samanta S., Locklin J., Langmuir, 2008, 24, 9558.

42. Zhou, F., Huck, W. T. S., Chem. Commun., 2005, 5999.

43. Azzaroni, O., Brown, A. A., Huck, W. T. S., Adv. Mater., 2007, 19, 151.

44. Abu-Lail, N. I., Kaholek, M., LaMattina, B., Clark, R. L., Zauscher, S., Sens Actuators B, 2006, 114, 371.

45. Zhou, F., Shu, W., Welland, M. E., Huck, W. T. S., J. Am. Chem. Soc., 2006, 128, 5326.

46. Azzaroni, O., Trappmann, B., van Rijn, P., Zhou, F., Kong, B., Huck, W.T.S., Angew. Chem. Int. Ed., 2006, 45, 7440.

47. Vlasov, Y. A., Bo, X. Z., Sturm, J. C., Norris, D. J., Nature, 2001, 414, 289.

48. Gratson, G. M., Xu, M., Lewis, J. A., Nature, 2004, 428, 386.

49. Jeon, S., Park, J.U., Cirelli, R., Yang, S., Heitzman, C.E., Braun, P.V., Kenis, P.J.A.,

50. Rogers, J. A., PNAS 2004, 101, 12428-12433.

51. Lin, S. Y., Fleming, J. G., Hetherington, D. L., Smith, B. K., Biswas, R., Ho, K. M., Sigalas, M. M., Zubrzycki, W., Kurtz, S. R., Bur, J., Nature, 1998, 394, 251.

52. Cumpston, B. H., Ananthavel, S. P., Barlow, S., Dyer, D. L., Ehrlich, J. E., Erskine, L. L., Heikal, A. A., Kuebler, S. M., Lee, I. Y. S., McCord-Maughon, D., Qin, J., Rockel, H., Rumi, M., Wu, X. L., Marder, S. R., Perry, J. W., Nature 1999, 398, 51-54.

53. Campbell, M., Sharp, D. N., Harrison, M. T., Denning, R.G., Turberfield, A. J., Nature, 2000, 404, 53-56.

54. A. P. Gast and W. B. Russel, Phys. Today, 1998, 51, 24.

55. S. Auer and D. Frenkel, Nature, 2001, 409, 1020.

56. U. Gasser, E. R. Weeks, A. Schofield, P. N. Pusey and D. A. Weitz, Science, 2001, 292, 258.

57. V. L. Colvin, MRS Bull., 2001, 26, 8, 637.

58. J. H. Holtz and S. A. Asher, Nature, 1997, 389, 829.

59. I. Gourevich, H. Pham, J. E. N. Jonkman and E. Kumacheva, Chem. Mater., 2004, 16, 1472.

60. Mihi, A.; Ocana, M.; Miguez, H. Adv. Mat., 2006, 18, (17), 2244.

61. Norris, D.J., Arlinghaus, E.G., Meng, L., Heiny, R., Scriven, L.E., Adv. Mat., 2004, 16, 1393.

62. Lu, Y., Yin, Y., Gates, B., Xia, Y., Langmuir 2001, 17, 6344.

63. Stachowiak, A. N., , Irvine, D. J., J. Biomed. Mater. Res. A., 2008, 85, 3, 815.

64. Zhang, Y., Wang, S., Eghtedari, M., Motamedi, M., Kotov, N. A., Adv. Func. Mater, 15, 5, 725.

65. Lee, J., Shanbhag, S., Kotov, N. A., J. Mater. Chem., 2006, 16, 3558.

66. Abbott, A., Nature, 2003, 424, 870.

67. Xie, Y., Yang, S. T., Kniss, D. A., Tissue Eng., 2001, 7, 585.

68. Meyle, J., Gultig, K., Wolburg, H., von Recum, A. F., J. Biomed. Mater. Res., 1993, 27, 1553.

69. Wojciak-Stothard, B., Madeja, Z., Korohoda, W., Curtis, A., Wilkinson, C., Cell Biol. Int., 1995, 19, 485.

70. Oakley, C., Brunette, D. M., Biochem. Cell. Biol. 1995, 73, 473.

71. Clark, P., Connolly, P., Curtis, A. S. G., Dow, J. A. T, Wilkinson, C. D. W., J. Cell. Sci., 1991, 99, 73.

72. Dunn, G. A, Brown, A. F., J. Cell. Sci. 1986, 83, 313.

73. Teixeira, A. I., Abrams, G. A., Murphy, C. J., Nealey, P. F., J. Vac. Sci. Technol. B, 2003, 21, 2, 683.

CHAPTER 2

MOLECULAR TRANSPORT DIRECTED VIA PATTERNED FUNCTIONALIZED SURFACES

Significant portions of this chapter were published as:

N. Yonet-Tanyeri, R. C. Evans, H. Tu, and P. V. Braun, Molecular Transport Directed via Patterned Functionalized Surfaces, Advanced Materials, 23, 1739-1743, 2011.

2.1 Introduction

Advances in micro and nanofabrication, coupled with recent developments in polymer science, provide powerful tools for fabricating functional surfaces with high degrees of spatial and chemical control. Numerous patterning strategies including conventional lithographic methods and modern printing strategies can be coupled with emerging chemistries to grow polymers into micro- and nanoscale polymer patterns on surfaces. Such surfaces are utilized for a diverse array of applications in fields ranging from biology to physics, including studies on biosensing, controlled wetting, and optical and microelectronic devices [1-4]. Here we demonstrate a new direction for patterned polymer brushes, namely that functionalized patterned polymer brushes can direct the diffusive transport of small molecules within well-defined microscale pathways, a potential new paradigm for defined molecular transport.

The two-dimensional transport of chemical species including synthetic polymers, DNA, ions, small particles and proteins on surfaces has attracted substantial interest [5-9]. These studies have benefited from a variety of surface functionalizations including surface tethered poly(triphenylamine acrylate), poly(*N*-isopropylarcylamide), polystyrene, and spin coated poly(methyl methacrylate), poly(isobutyl methacrylate) and poly(ethyl methacrylate) films [10-14]. We have for example studied the diffusion of prodan, a small molecule dye, on bare glass and on various self-assembled monolayers (SAMs) [15]. These studies have contributed to the detection and monitoring of the diffusion characteristics of small molecules on functional

surfaces, however, in all these studies, the direction of the transport has been uncontrolled. We ask if the diffusive transport of molecules can be directed across a surface, in rough analogy to the transport of fluids in a microfluidic device. Here we report the defined diffusive transport of a model probe molecule using a two-dimensionally patterned polymer brush. This required formation of both transporting and barrier surface chemistries.

2.2 Experimental

2.2.1 Materials

(Oligoethylene glycol) acrylate (OEGA), 10-undecen-1-ol (98 %), copper (I) bromide (CuBr, 99.999%), 8-hydroxypyrene-1,3,6-trisulfonic acid trisodium salt (HPTS), Nile Blue chloride, inhibitor removers for removing hydroquinone and monomethyl ether hydroquinone were purchased from Aldrich. 2-Bromoisobutyryl bromide (98%), 1,1,4,7,7-pentamethyldiethylenetriamine (PMDETA, 99+%) were obtained from Acros. Trichlorosilane and Karstedt's catalyst were obtained from Gelest. Poly(dimethyl) siloxane (PDMS) prepolymer was purchased from Sylgard. Phosphate pH 6 buffer was from Fisher Scientific. Pluronic 127 was from BASF. OEGA was purified by passing through a column packed with inhibitor removers. All other chemicals were used as they were received.

2.2.2 Functional Surfaces with Patterned Polymer Brushes

The initiator, (11-(2-bromo-2-methyl)propionyloxy)undecyltrichlorosilane, was synthesized by following previously reported procedure [16]. Following the printing process of the initiator on the solid substrate, the functionalized surface was washed with ethanol and dried in a nitrogen flow. Substrates with surface-initiated patterns of the initiator were placed in a reaction vessel and degassed with three freeze-pump-thaw cycles. Then, OEGA (4.8 g, 12.86 mmol) was diluted with methanol/water mixture (v/v=1/4) in a Schlenk tube and degassed for at

least 30 min. The ligand, PMDETA (27 μL, 0.12 mmol) and the catalyst, CuBr (0.02 mg, 0.12 mmol) were added to the OEGA solution. A sacrificial initiator, ethyl 2-bromoisobutyrate (0.5 μL, 0.003 mmol), was added to the polymerization solution. The solution of the monomer, catalyst and ligand was transferred through a cannula into the reaction vessel containing solid substrates with patterns of initiator self-assembled monolayers. The polymerization reaction took place at room temperature under a nitrogen atmosphere. After 18 hours, the substrates were rinsed with acetone, ethanol, and water and dried in a nitrogen flow. The solvent was removed from the polymerization solution by evaporation. The bulk POEGA was purified by passing through a silica column. A mixture of THF and methanol (7:3) (v/v) was used as the eluent of the column. After evaporating the solvent, pure POEGA was diluted in THF for molecular weight measurement by Gel Permeation Chromatography (GPC). GPC analyses were performed to determine number average molecular weight of polymer, M_n, on a system composed of a Waters 515 HPLC pump, a Thermoseparations Trace series AS100 autosampler, a series of three Waters HR Styragel columns (7.8×300 mm, HR3, HR4, and HR5), and a Viscotek TDA Model 300 triple detector array, in THF at 30°C. An Asylum Research MFP-3D AFM was used to characterize the thickness of the patterned POEGA brushes in dry and swollen forms by using a Veeco NP-S tapping mode probe.

2.2.3 Molecular Device Preparation

Fabrication of a microfluidic channel in the PDMS device is based on a non-lithographic process. In this technique, direct–write assembly of a fugitive organic ink that possesses temperature dependent rheological characteristics facilitates deposition of a singular channel and vertical posts on the substrate at ambient temperature [20]. The fugitive ink which is a water soluble triblock copolymer of poly(ethylene oxide) (PEO) and poly(propylene oxide) (PPO), also known as Pluronic F127A, forms micelles at temperatures that are higher than ~10ºC when its

concentration exceeds 20 w/w%. Below this micellization temperature, it completely liquefies. Once the channel and two posts were deposited perpendicular to the linear patterns of POEGA brushes on the solid substrate, the PDMS prepolymer was spread over covering the copolymer ink channel and the vertical inks. After the PDMS was cured at elevated temperatures for an hour, the molecular device was cooled down to 4-5ºC. The softened ink was easily removed from the device by washing with several cycles of cold water. This resulted in formation of the microchannel in a non-lithographic fabrication technique and vertical posts were converted to holes that pass through the device. Before delivering the HPTS solution, the microchannel was filled with HPTS-free pH 6 buffer solution for two days.

2.2.4 Directed Probe Transportation

Once the POEGA brushes were swollen with the buffer, 0.03 mM HPTS in buffer solution was introduced in the channel. The molecular device was kept in a humid environment during the diffusion process to reduce any water evaporation from the device. Images of the desired locations were acquired after washing the microchannel with the buffer solution. Each imaging session took approximately one hour. At the end of the imaging process, the microchannel was filled with the HPTS solution and the device was left in the humid chamber up to 240 hours. A Zeiss inverted microscope (Model 200M) equipped with a metal-halide lamp (X-Cite 120), a DAPI filter set (31000v2, Chroma Technology) designed to transmit light with wavelengths greater than 412 nm and reflect below 412, and a CCD camera (EM CCD 512B, Roper Scientific) was used to image the molecular devices. The imaging study was performed using 10X and 20X objectives (Zeiss) with NAs of 0.3 and 0.6, respectively.

2.3 Results and Discussion

A hydrophilic poly(oligoethylene glycol) acrylate (POEGA) brush (Figure 2. 1a) was specifically selected because of its potential to dissolve a wide range of hydrophilic species and

its low glass transition temperature. The substrate was patterned with a POEGA brush using microcontact printing (μCP) of the atom transfer radical polymerization (ATRP) initiator 10-undecyl-1-yl 2-bromo-2-methylpropionate followed by surface-initiated ATRP of oligo(ethylene glycol) acrylate in the presence of a sacrificial initiator [16-18]. We were able to determine the grafting density of the patterns of POEGA brushes (σ) by using the molecular weight of the POEGA that grew in solution off the sacrificial initiator [19]. POEGA brush grafting density was calculated by (Eq. 2. 1)

$$\sigma = \frac{h\rho N_A}{M_n} \qquad \text{(Eq. 2. 1)}$$

where σ is polymer grafting density, ρ is polymer density, *h* is dry thickness of polymer, M_n is taken as number average molecular weight of polymer grown in bulk solution, and N_A is Avogadro's number [19]. σ was determined to be 0.7 chains/nm^2 using the following inputs to Eq.2 1: *h* is 64 nm, ρ is assumed to be 1.07 g/cm^3, the density of PEG, M_n is 59981 g/mol (from GPC measurement). 8-hydroxypyrene-1,3,6-trisulfonic acid trisodium salt (HPTS) was selected as the fluorescent probe molecule (Figure 2. 1b) because it is soluble in both water and the POEGA brush, is photolitically stable, and its excitation wavelength is in the 370-400 nm region, allowing for direct imaging the dye diffusion without the use of UV light, which may damage the POEGA brushes.

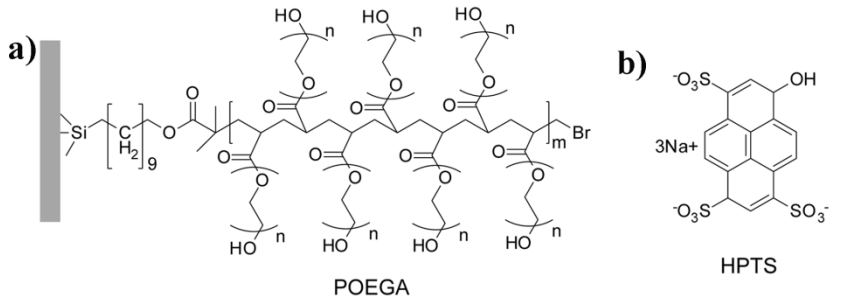

Figure 2. 1. Chemical structures of the POEGA brush (a) and the probe molecule, HPTS (b).

AFM thickness measurements revealed that the patterned POEGA brush thickness increased as expected from ~64 nm to ~145 nm when immersed in water (Figure 2. 2). In the swollen form, the surface tethered POEGA pattern provides a quasi two-dimensional space on the silica surface for small molecule transport.

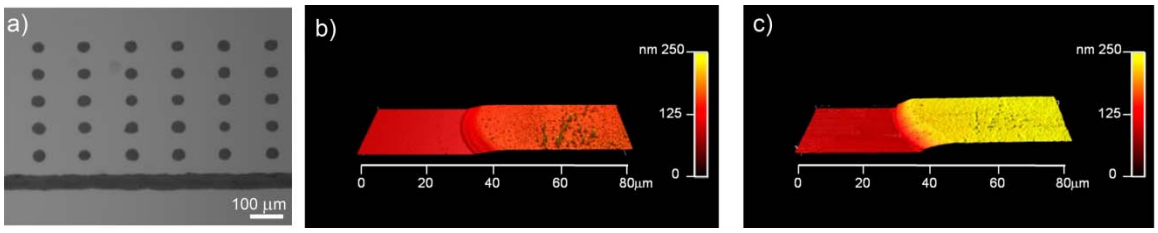

Figure 2. 2. (a) Optical image of patterned POEGA brushes showing both the continuous lines and isolated dots. 3-D AFM surface plots of (b) dry and (c) water swollen patterned POEGA brushes.

Assuming the POEGA brush and water densities are the same, the aqueous volume fraction was estimated to be ~0.56. The swollen POEGA brush volume fraction (f_p) can be estimated as

$$f_p = \frac{h}{h_{wet}} \qquad \text{(Eq. 2. 2)}$$

where h is dry thickness and h_{wet} is wet thickness of POEGA brush. f_p was determined to be 0.44 when h is 64 nm and h_{wet} is 145 nm.

The regions surrounding the polymer brush are left as bare glass (Figure 2. 3a). The water swollen patterned polymer brush serves to direct the two-dimensional diffusive transport of molecules due to the very large contrast between the rate of diffusion of probe molecules within the polymer brush and along the bare substrate (Figure 2. 3b).

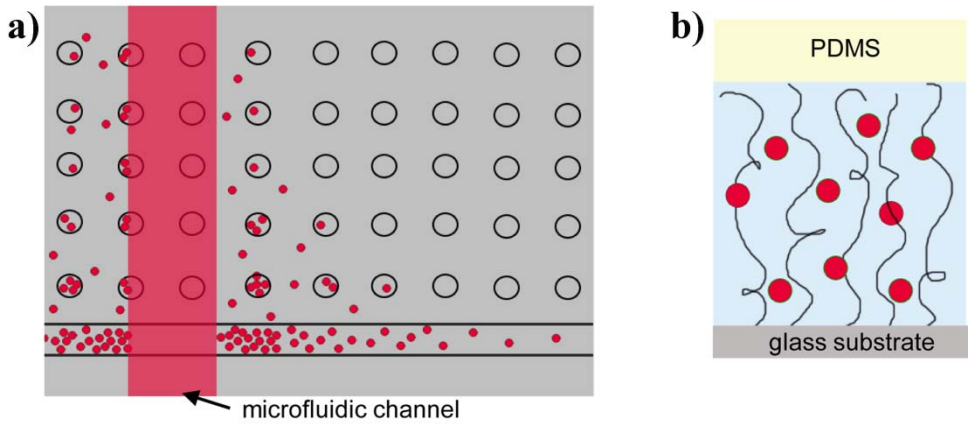

Figure 2. 3. (a) Schematic top-view illustration of microfluidic dye-delivery device. (b) Side-view of water (blue) and HPTS swollen surface tethered POEGA brushes capped with PDMS. In (a) and (b), the HPTS is represented by red dots, and the regions between the two lines and inside of the circles are POEGA brushes.

Following formation of the patterned polymer brush, a fugitive line of ink (800 µm wide and 400 µm high) is written perpendicular to the polymer brush lines via the direct-write assembly of a mixture of the non-ionic surfactant Pluronic F127 and water (Figure 2. 4) [20]. The entire substrate is capped by curing poly(dimethyl) siloxane (PDMS) directly on this substrate. Small holes are formed through the PDMS down to the fugitive ink line, and the fugitive ink is removed with water. If the PDMS was removed, the interface with the substrate failed cohesively, indicating strong, leak-free attachment of the PDMS to the substrate.

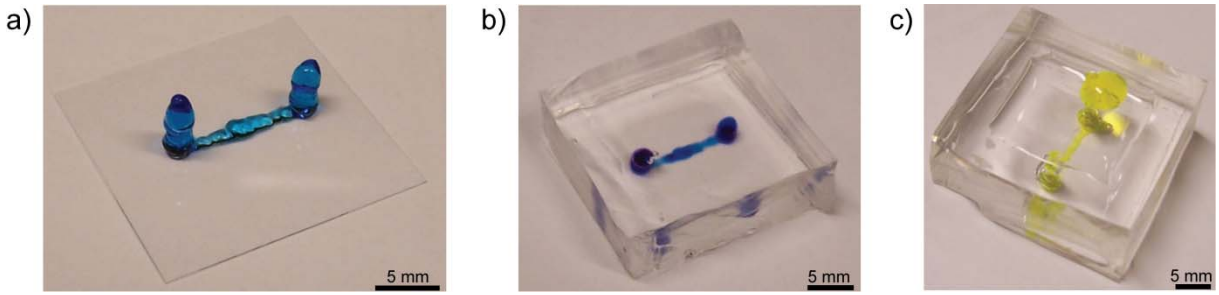

Figure 2. 4. Optical images of the molecular device preparation procedure. The optical image of (a) direct-write assembly of fugitive organic ink (Pluronic F127A) stained with Nile Blue chloride on a cover glass, (b) the PDMS and copolymer ink molecular device after curing process of the PDMS prepolymer, (c) the PDMS device after removing the ink. In (c), the microchannel is filled with the HPTS solution.

The microfluidic channel is filled with probe-free buffer solution for several days to allow the system to reach equilibrium. An aqueous pH 6 buffer solution of the probe molecule is then

introduced into the channel delivering the probe (HPTS) to a small region of the surface (Figure 2. 3a). Once the HPTS reaches the polymer brush, it diffuses laterally along the substrate. The position of the probe molecules is determined by fluorescence microscopy.

When the HPTS solution was introduced into the microfluidic channel, two domains become apparent under the fluorescence microscope: the microfluidic channel, which has a high concentration of HPTS and the rest of the device, which initially contains no HPTS. It is important to note that HPTS is not soluble in PDMS and POEGA brushes are not fluorescent in the wavelengths used to observe dye diffusion. Over time, the fluorescence spreads down the patterned polymer brush, starting from regions adjacent to the microfluidic channel to regions further away (Figure 2. 5 and 7a). As shown in Figure 2. 3a, surrounding the patterned line is an array of polymer brush “islands”. These islands serve as markers. They do not fluoresce, even after extended times, indicating dye molecules do not appreciably diffuse across the bare substrate. Figure 2. 5 contrasts the fluorescence from linear versus zigzag POEGA patterns after 168 hours. The microchannel is at the furthest left side of the fluorescence image as a dark region perpendicular to the POEGA line. The HPTS transportation in the x-direction is retarded along the zigzag pattern compared to the linear one because of the greater path length of the zigzag feature for a given x-direction. The total distance the dye molecules diffuse is about 1.3 mm for both the linear and zigzag features. The distance diffused by the HPTS in Figure 2. 5 appears greater than in Figure 2. 7b; however this is not the case. The different appearance is due to the enhanced brightness of Figure 2. 7b. Note, for all experiments, the HPTS filled channel appears dark, as it is rinsed with buffer prior to imaging because it leads to an unacceptably large background signal if the dye is not removed.

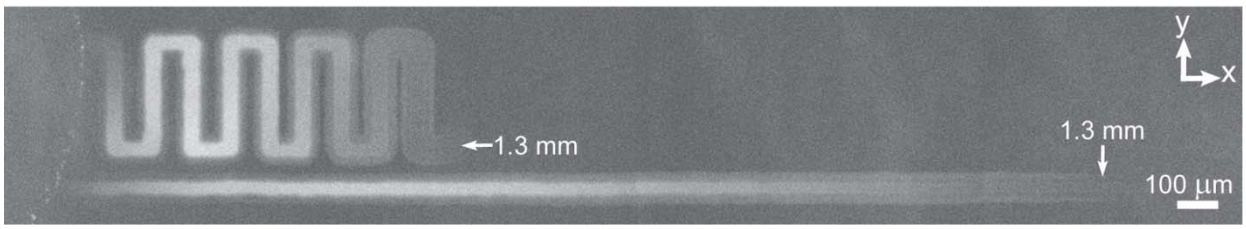

Figure 2. 5. Fluorescence image showing HPTS diffusion through the zig-zag and linear patterned POEGA brush 168 hours after HPTS delivery.

We have prepared the molecular device via conventional lithographic fabrication methods. The PDMS slab including singular μfluidic channel was activated by ozone treatment just before its assembly with the glass slide that was functionalized with the patterned POEGA brushes. Directed HPTS diffusion study was carried out as following the previous experiment. The fluorescence microscope observations revealed that HPTS molecules follow the linear pathway of the POEGA brushes (x direction) but also there is a surface diffusion at the interface between the PMDS and the unpatterned-bare glass regions (both x and ±y directions) leaving the isolated POEGA brush islands fluorescently bright. Figure 2. 6 demonstrates the HPTS diffusive transport in a device that was prepared by traditional lithographic methods 168 hours after the probe delivery.

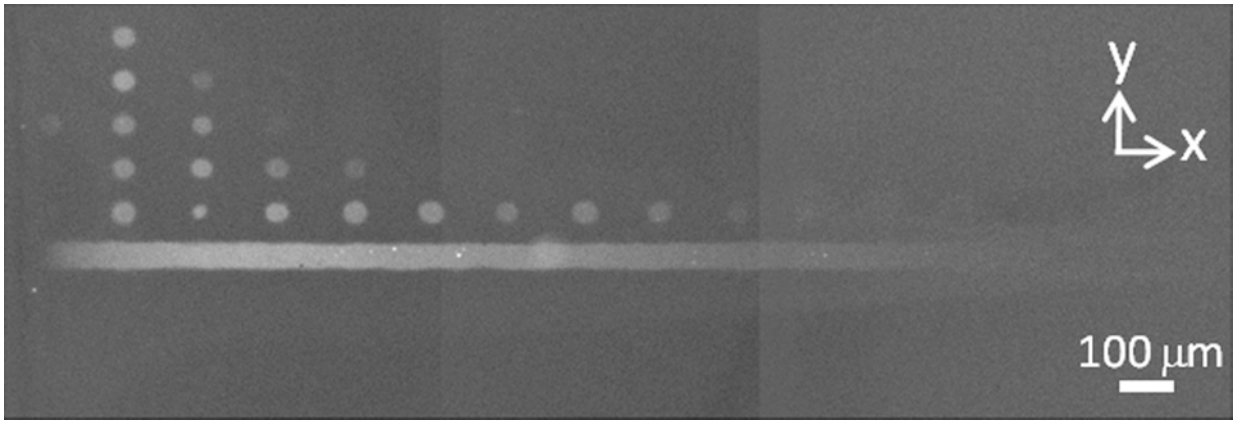

Figure 2. 6. Fluorescence image of HPTS transportation through linear patterned POEGA brush 168 hours after HPTS deliver. The device was prepared by conventional lithographic fabrication methods.

To quantify the rate of HPTS diffusion in the POEGA brushes, and confirm that dye diffusion does not occur on the bare substrate, a pattern consisting of continuous line and

unconnected indicator islands was designed. In the fluorescence image of Figure 2. 7a, the channel was at the furthest left side perpendicular to the POEGA line and the isolated POEGA islands were located only above (y-direction) the POEGA line. As time progresses, HPTS molecules travel along the preswollen continuous POEGA line in the x-direction. Once a probe molecule leaves the fluid-filled channel, it can either diffuse through the polymer brush, or along the substrate-PDMS interface. If HPTS travels along this interface, the isolated POEGA islands would become bright as HPTS diffused into them. The indicator POEGA islands remained non-fluorescent even at the end of 10 days of HPTS delivery (Figure 2. 7b). This is a clear indication that HPTS does not appreciably travel along the glass surface. The microchannel in the fluorescence images appears darker than the HPTS saturated POEGA line because it was rinsed with the buffer solution before each image acquisition; otherwise it results in excess background fluorescence. This washing step results in back-diffusion of probe molecules in the brush line close to the channel back into the channel. That is why the highest intensity value in HPTS diffusion profiles does not correspond to the reservoir which has the highest probe concentration during the diffusion process (Figure 2. 7c). Over the total 240 hours experiment, the channel is dye-free for only about 4 hours, so we do not expect this to significantly impact the results presented here.

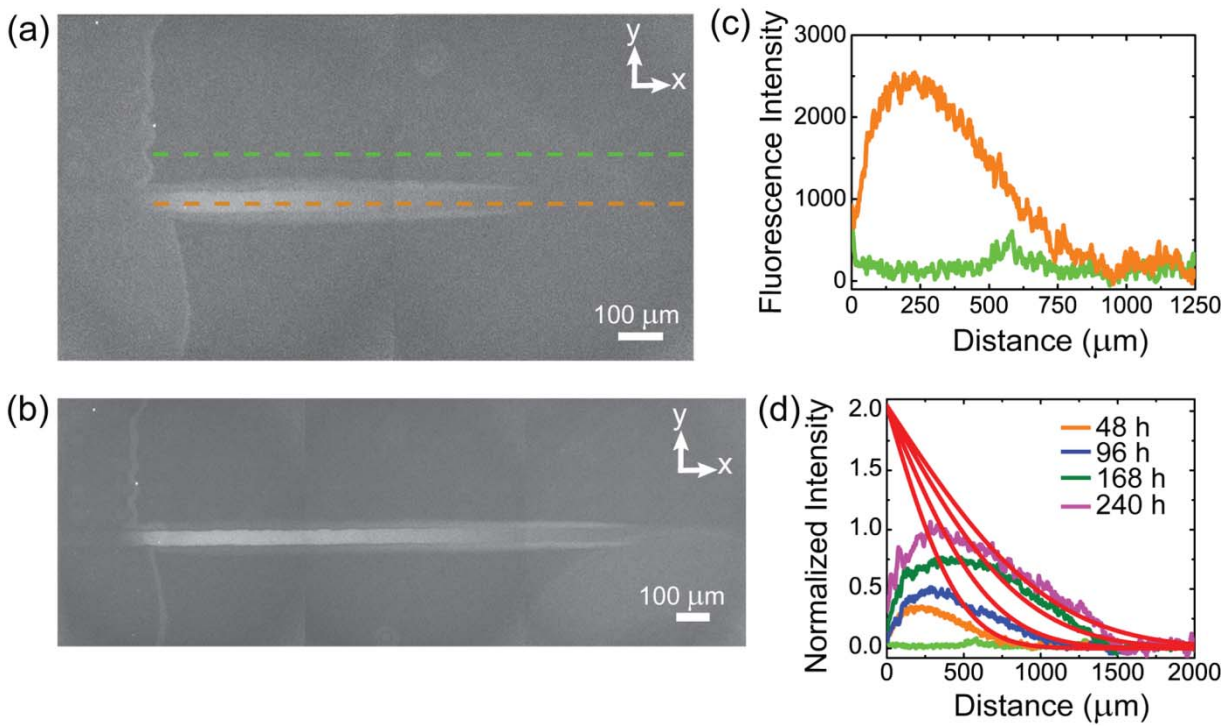

Figure 2. 7. Fluorescence images of HPTS diffusion across the substrate patterned with POEGA brush lines and islands (a) 48 hours and (b) 240 hours after the introduction of HPTS. The substrate is patterned as illustrated in Figure 1b. (c) Fluorescence intensity profiles in the POEGA brush line (orange) and on the bare substrate (green) for the fluorescence image in (a). (d) Fluorescence line profiles in the POEGA brush line as a function of time from 48 to 240 hours after HPTS introduction. The red lines are the expected profile for 1-D diffusion from a constant concentration source (Eqn. 2. 3).

The HPTS delivery in the patterned POEGA brushes was observed up to 10 days (Figure 2. 7b and Figure 2. 8). Fluorescence images and corresponding normalized intensity vs. distance plots show that after 240 hours the furthest distance that HPTS travels along the POEGA line is approximately 1.5 mm away from the microfluidic channel. The device is constructed such that C_0, the HPTS concentration in the microfluidic channel remains constant throughout the experiment and the HPTS concentration is zero in the polymer brush at time (t) = 0. Thus, the HPTS concentration as a function of distance and time, C(x, t), can be modeled as a simple one-dimensional diffusion (Eq. 2. 3).

$$C(x,t)=C_0\,\mathrm{erfc}\left(x/\sqrt{4Dt}\right) \qquad \text{(Eq. 2. 3)}$$

For these calculations, we assume that the emitted light intensity is directly proportional to the concentration, C(x, t), of the HPTS molecules and ignore the effect of the washing step of the microchannel.

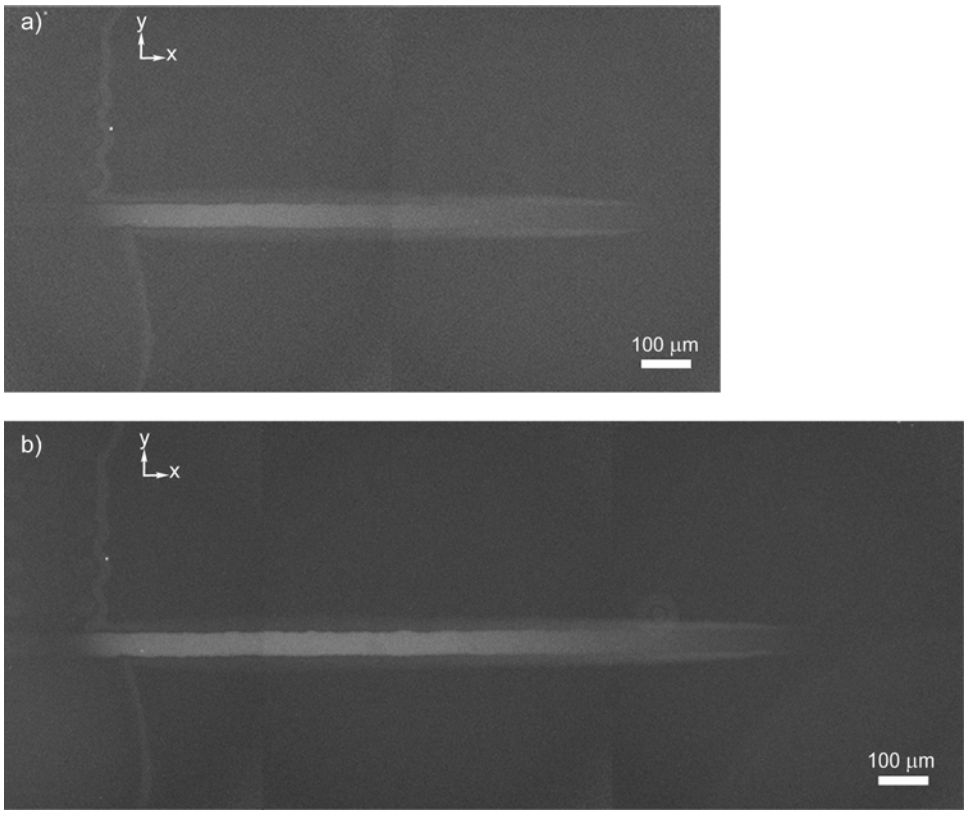

Figure 2. 8. Fluorescence images of directed HPTS transportation along the linear patterns of POEGA brushes (a) 96 and (b) 168 hours after probe delivery.

We performed experiments at various HPTS concentrations in solution ranging from 0.03 mM to 1 mM to confirm fluorescence quenching was not impacting the analysis (Figure 2. 9). At HPTS concentrations up to 0.03 mM, the fluorescence intensity within the dye solution swollen POEGA polymer brush increases with time as expected. For higher concentrations (0.1 and 1 mM), self-quenching was observed as a steady (Figure 2. 9b) or descending (Figure 2. 9c) fluorescence intensity as a function of diffusion time (the opposite of the excepted response). Self-quenching of HPTS in the swollen POEGA brushes occurs before self-quenching in the free solution, perhaps because the HPTS preferentially segregates into the polymer brush [21]. We do not have a way to measure the absolute concentration of HPTS in

the brush, and thus simply lowered the HPTS concentration until quenching was not observed. The best fit to the data gives a lateral diffusion coefficient of HPTS in the swollen POEGA brush of 0.5×10^{-8} cm^2/s. We do not try to fit the data in the first 500 μm due to the aforementioned effect of washing. The slow diffusion of HPTS molecules in the POEGA brushes relative to the free diffusion of HPTS in water (2.3×10^{-6} cm^2/s) is a direct result of the inhibition of the HPTS diffusion by the water swollen polymer brushes [22].

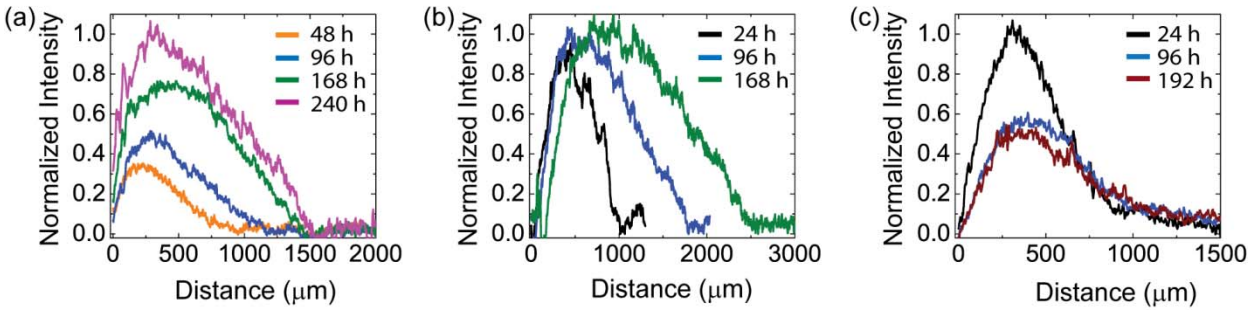

Figure 2. 9. Fluorescence intensity profiles along the POEGA brush line as a function of HPTS concentration as a function of time and HPTS concentration. (a) 0.03 mM, (b) 0.1 mM, (c) 1 mM.

There have been numerous theoretical models that attempt to explain the retardation of small molecule diffusion in polymer solutions [23, 24]. The simplest model only requires an estimate of the polymer fraction, however this model is not very accurate for a system such as ours [25]. The more complex models require knowledge of the solvent free volume in the polymer solution or the polymer chain-solvent-diffusing species interactions, which are not parameters we can easily determine, limiting implementation of these models to our system [26, 27].

2.4 Conclusions

In conclusion, by using a fluorescent dye molecule, we have shown that patterned polymer brushes can spatially direct the transportation of molecular species on solid substrates. As expected, the rate of diffusion through the polymer brush is significantly slower than for free

diffusion in solution. The rate of dye diffusion across the unpatterned regions of the substrate was below the detectable limit. This approach to directed molecular transport brings a well defined control over the direction of solid-state molecular diffusion and potentially represents a new paradigm for on-chip transport of molecules. Although to date we have only demonstrated the directed molecular transport of a polar dye through a hydrophilic polymer brush, we believe this approach will become a general method for the directed transport of molecular species.

2.5 References

1. Nie, Z., Kumacheva, E., Nat. Mater, 2008, 4, 277.
2. Valsesia, A., Colpo, P., Silvan, M. M., Meziani, T., Ceccone, G., Rossi, F., Nano Lett., 2004, 4, 1047.
3. Lenz, P., Adv. Mat, 1999, 11, 1513.
4. Kim, D. H., Lau, K. H. A., Robertson, J. W. F., Lee, O.-J, Jeong, U., Lee, J. I., Hawker, C. J., Russell, T. P., Kim, J. K., Knoll, W., Adv. Mat, 2005, 17, 2442.
5. Sukhishvili, S. A., Chen, Y., Muller, J. D., Gratton, E., Schweizer, K. S., Granick, S., Macromolecules, 2002, 35, 1776.
6. Maier, B., Radler, J. O., Phys. Rev. Lett., 1999, 82, 1911.
7. Reznik, C., Darugar, Q., Wheat, A., Fulghum, T., Advincula, R. C., Landes, C. F., J. Phys. Chem. B, 2008, 112, 10890.
8. Filippidi, E., Michailidou, V., Loppinet, B., Ruhe, J., Fytas, G., Langmuir, 2007, 23, 5139.
9. Yang, Z. H., Galloway, J. A., Yu, H. U., Langmuir, 1999, 15, 8405.
10. Whiting, G. L., Snaith, H. J., Khodabakhsh, S., Andreasen, J. W., Breiby, D., Nielsen, M. M., Greenham, N. C., Friend, P. H., Huck, W. T. S., Nano Lett., 2006, 6, 573.
11. Tu, H., Hong, L. , Anthony, S. M., Braun, P. V., Granick, S., Langmuir, 2007, 23, 2322.
12. Michailidou, V. N., Loppinet, B., Vo, C. D., Ruhe, J., Tauer, K., Fytas, G., Eur. Phys. J. E., 2008, 26, 35.

13. Cao, T., Johnston, K. P., Webber, S. E., Macromolecules, 2005, 38, 1335.

14. Deppe, D. D., Dhinojwala, A., Torkelson, J. M., Macromolecules, 1996, 29, 3898.

15. Heitzman, C. E., Tu, H., H. L., Braun, P. V., J. Phys. Chem. B, 2004, 108, 13764.

16. Matyjaszewski, K., Miller, P. J., Shukla, N., Immaraporn, B., Gelman, A., Luokala, B. B., Siclovan, T. M., Kickelbick, G., Vallant, T., Hoffmann, H., Pakula, T., Macromolecules, 1999, 32, 8716.

17. Tu, H., Heitzman, C. E., Braun, P. V., Langmuir, 2004, 20, 8313.

18. Tu, H., Heitzman, C. E., Evans, R. C., Braun, P. V., Abstracts of Papers of the American Chemical Society 2005, 229, 394-POLY.

19. Bhat, R. R., Tomlinson, M. R., Wu, T., Genzer, J., Adv. Polym. Sci., 2006, 198, 51.

20. Hansen, C. J., Wu, W., Toohey, K. S., Sottos, N. R., White, S. R., Lewis, J. A., Adv. Mater., 2009, 21, 4143.

21. Siwick, B. J., Bakker, H. J., J. Am. Chem. Soc., 2007, 129, 13412.

22. Xia, P., Bungay, P. M., Gibson, C. C., Kovbasnjuk, O. N., Spring, K. R., Biophys. J., 1998, 74, 3302.

23. Amsden, B., Macromolecules, 1998, 31, 8382.

24. Masaro, L., Zhu, X. X., Prog. Polym. Sci., 1999, 24, 731.

25. Mackie, J. S., Meares, P., Proc. R. Soc. London, 1955, A232, 498.

26. Yasuda, H., Lamaze, C. E., Ikenberry, L. D., Die Makro. Chem., 1968, 118, 19.

27. Cukier, R. I., Macromolecules, 1984, 17, 252.

CHAPTER 3

DIRECTED ION TRANSPORTATION AND ITS APPLICATION IN NANOPARTICLE SYNTHESIS

3.1 Introduction

Metal nanoparticles can be synthesized using several methods in various sizes and shapes which define their optical, chemical, and electronic properties. Some of the very first synthetic methods for very small noble-particles continue to be used as standard techniques. One of the well-known methods developed by Turkevich to produce ~10 nm Au nanoparticles utilizes the reduction of chloroauric acid with sodium citrate [1]. The most common method, the so-called the Creighton method, to produce Ag nanoparticles, employs the reduction of $AgNO_3$ with $NaBH_4$ [2]. This method is also applicable to produce nanoparticles using other metals such as Pt, Pd, Cu, and Ni [3-6].

For many applications, it is very important to produce such nanoparticles in controlled size and distribution. Much effort on nanoparticle synthesis has been devoted to develop synthetic pathways for achieving this goal [7-9]. Recently, there has been growing interest in facilitating polymers such as dendrimers, block copolymer micelles, star block copolymers, and polymer microgels as the capping agent for nanoparticles [10-13]. Alternatively, rich physical properties of polymer brushes grown from a solid surface may lead to intriguing applications in nanoparticle synthesis as well. Surface tethered polymer brushes like 2-methacryloyloxy)ethyltrimethylammonium chloride, poly(2-hydroxyethyl methacrylate), poly 2-methacryloyloxy) ethyltrimethyl ammoniumchloride are only a few examples of compatible chemistries used in nanoparticle synthesis [14-16]. In this chapter, end-grafted poly(oligoethylene glycol) acrylate (POEGA) brushes were used as the capping agent in polymer brush mediated nanoparticle synthesis.

Our ultimate goal is to design molecular devices that are capable of generating spatio-temporally controlled surface nanoreactions. In this work, we utilized patterned polymer brushes to direct the diffusive transport of multiple reactive ionic species (Specifically, metal ions and reducing agent) to facilitate controlled formation of nanoparticles. Directed transportation of reactive ions constructs surface gradients of reactive chemistries which are used for one-pot synthesis of nanoparticles with various particle size and distribution. Directed transportation mechanism of small chemical species, i.e. fluorescence dye molecules, via molecular devices was explained in details in Chapter 2. This chapter mainly focuses on implementation of this technology to directed ion transportation with the purpose of nanoparticle synthesis.

3.2 Experimental

3.2.1 Materials

$HAuCl_4.3H_2O$, $CuCl_2.2H_2O$, $NaBH_4$ were purchased from Sigma-Aldrich and used as received. pH 6 (potassium phosphate monobasic-sodium hydroxide) and pH 2 (potassium chloride/hydrochloric acid) buffer solutions were purchased from Fisher.

3.2.3 Dual Channel Molecular Device Preparation

Glass substrates were functionalized with patterned POEGA as described in Chapter 2. The molecular device consisting of two fluidic channels was fabricated. Here, two parallel channels with vertical posts were generated by direct-writing Pluronic 127A on the patterned POEGA surface. Polydimethylsiloxane (PDMS) prepolymer was cast on this surface to cover the organic ink channels and the vertical posts. Once the PDMS was cured, the device was cooled down to 4-5 ºC to soften the ink. Then, the ink was washed with cold water resulting in two microchannels in the PDMS device.

3.2.4 Directed Ion Diffusion for Generation of Nanoreactor

The two channels were filled with buffer solution or Milli-Q water such that the patterned POEGA brushes became water swollen (and in equilibrium with water) as water diffused through the patterns. Subsequently, aqueous ion solution was introduced into one of the microchannels. The second channel was filled with the reducing agent solution. The holes of the both channels were capped with vacuum grease to prevent solvent evaporation throughout the diffusion process. A Zeiss Axio observer.D1m inverted light microscope was used in dark field mode to visualize the device. Images were taken by using 20X (NA = 0.4, WD = 2.8 mm) and 100X (NA = 0.75, WD = 0.95 mm) objectives.

3.3 Results and Discussion

We have developed on-chip platforms to build spatio-temporal controlled nanoreactors by directing diffusive transport of ionic species that react with each other. The molecular device design was composed of two microchannels which provided reservoir for the two reactive ion solutions. Figure 3. 1a is an example of such devices. Dual channels were filled with 2 different dye solutions for demonstration. The substrate was functionalized with linear patterns of POEGA brushes that guide two reactive ionic species to diffuse towards one another in between the two microchannels. The direction of ion transportation in this device is shown in red and black arrows in Figure 3. 1b.

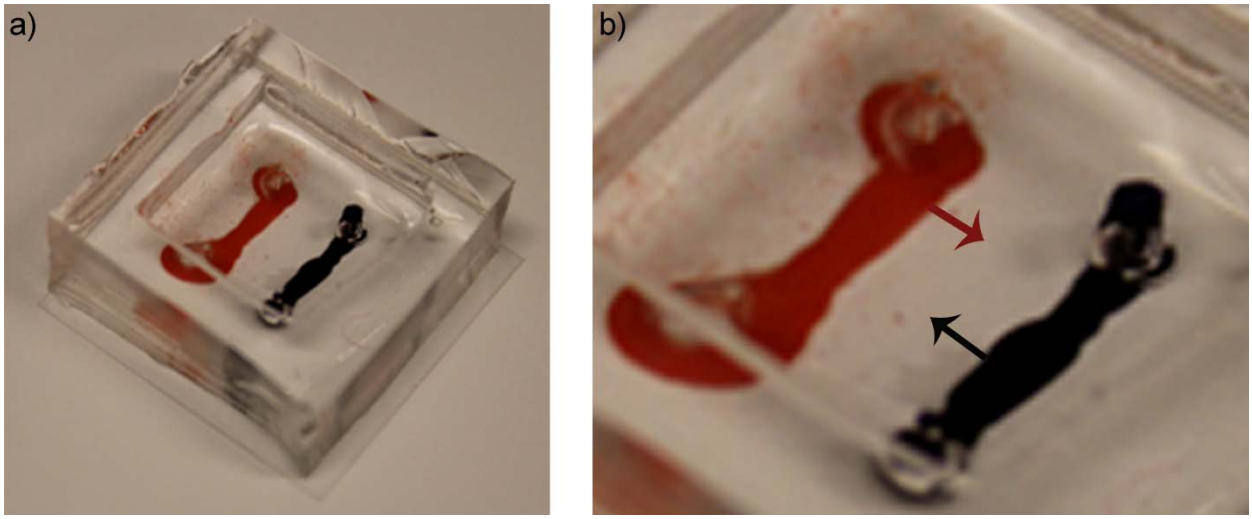

Figure 3. 1. (a) Optical image of a dual channel molecular device. Each channel was filled with two different dye solutions; red is aqueous rhodamine solution whereas black is aqueous nile blue solution. (b) Red and black arrows show the direction of diffusion for rhodamine and nile blue respectively.

For the nanoparticle synthesis, one channel is filled with metal ion solution whereas the other channel is filled with aqueous solution of reducing agent. Over time, reactive ions diffuse through the linear pattern of polymer brushes towards the other microchannel (Figure 3. 2). At the location where two ion solutions encounter, metal ions are reduced to form metal nanoparticles. Spatio-temporal control over the reduction reaction is achieved by developing molecular devices with desired polymer brush patterns. In this study, we have used linear and isolated circular POEGA patterns (Figure 3. 3).

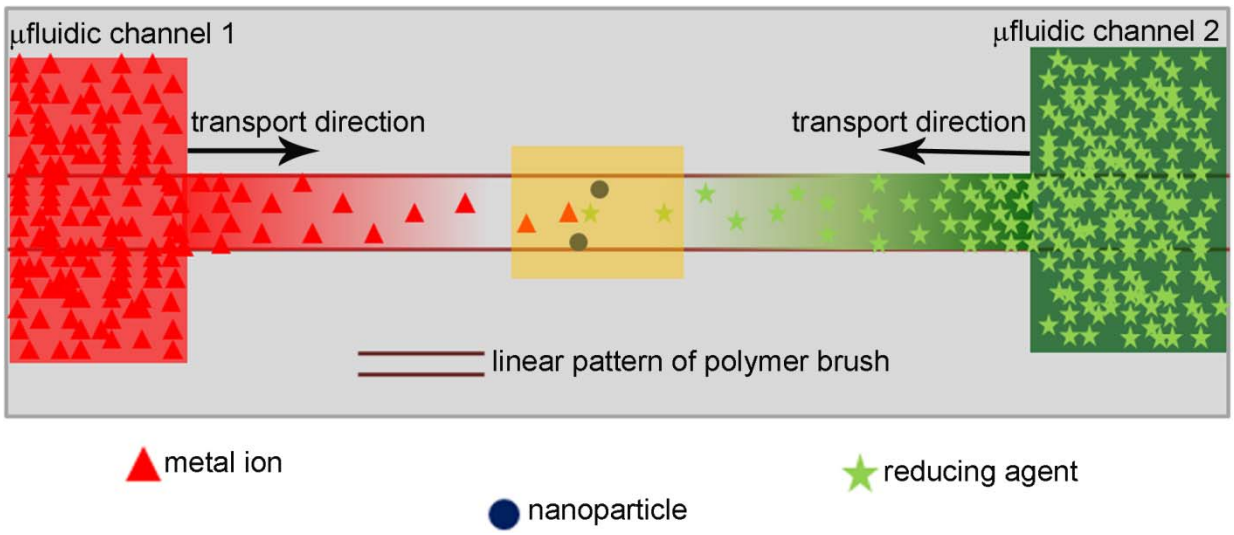

Figure 3. 2. Schematic representation of dual channel molecular devices (top view) for the spatio-temporally controlled synthesis of nanoparticles through reduction of metal ions.

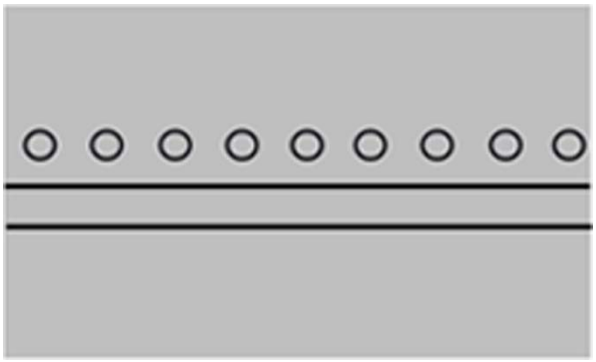

Figure 3. 3. Illustration of POEGA brush patterns (top view) on glass surface. Polymer brushes are grown in the regions between the two lines and inside the circles.

The reduction of $AuCl_4^-$, and Cu^{2+} ions were widely studied in bulk solution by many research groups and the reduction chemistry of these metal ions are well [17, 18]. Therefore, we chose to work on directed transportation and subsequent reduction of these metal in the dual channel molecular devices. Nanoparticle synthesis was investigated for $AuCl_4^-$ ions as a function of pH and the concentration of ion solutions. $NaBH_4$ was used as the reducing agent for the reduction of all ion types. The reduction reactions were monitored via nanoparticle formation using dark field microscopy.

Figure 3. 4 demonstrates a typical dark field image of nanoparticles synthesized following the introduction and transportation of $AuCl_4^-$ and BH_4^- solutions within the molecular

device. $AuCl_4^-$ and BH_4^- reservoirs are furthest to the left and right on the image respectively. The linear pattern of POEGA brushes, not visible under dark field microscope, is located in between the two channels (reservoirs) and forms a “nanochannel” directing molecular transport between the two microfluidic reservoirs. Direction of diffusion for both ions is shown with red and green arrows. After 24 hours, $AuCl_4^-$ ion reduction was observed along the POEGA line that was highlighted with the orange box. In this device, an array of isolated, circular POEGA brush islands are located above the POEGA brush line as a control for unintended isotropic diffusion of ions.

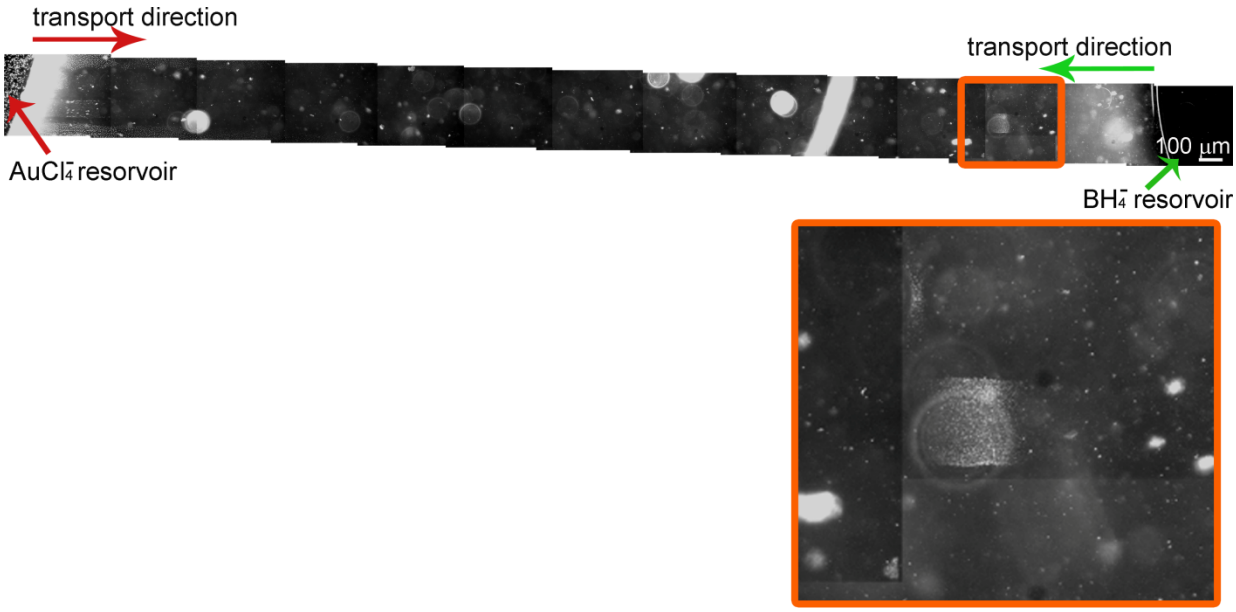

Figure 3. 4. Dark field optical image of $AuCl_4^-$ and BH_4^- transportation along the linear POEGA pattern and Au nanoparticles formation (aqueous solutions were prepared in pH 6 buffer).

It is important to note that the dark field image includes several bright spots in various locations which are due to impurities (bubbles, particles) in the PDMS. Furthermore, it was reported in an earlier study that $AuCl_4^-$ ions can be reduced to Au nanoparticles spontaneously in aqueous Pluronic solution at ambient temperature without any other reducing agent [19]. In our molecular device, we also observed that the $AuCl_4^-$ ions were reduced to Au nanoparticles spontaneously in the $AuCl_4^-$ reservoir. The undesired reduction in the microchannel can be explained by trace amount of Pluronic remaining in the channel after the fabrication process.

Another limitation in studying directed $AuCl_4^-$ ion transportation in our device was the self-reduction of $AuCl_4^-$ ions in the POEGA brushes as they diffused through. There are several reports that explain the effect of polyethylene glycol (PEG) chemistry on promoting stabilization of $AuCl_4^-$ ions and their reduction reaction [20]. The surface functionality of the molecular device with POEGA brushes should exhibit a similar effect on $AuCl_4^-$ ions. Thus, the self-reduction of $AuCl_4^-$ ions in the POEGA brush was observed in the region adjacent to the $AuCl_4^-$ reservoir where $AuCl_4^-$ ions concentration was maximum.

The transportation of ions in pH 6 and pH 2 buffers were studied in order to investigate the effect of pH on nanoparticle formation (Figure 3. 4, 5). Directed diffusion studies using these buffer solutions were performed in two different molecular devices at the same ion concentration (100 mM). Particle formation within the molecular devices was observed at fixed time intervals. Unfortunately, the distance between the two reservoirs was not the same in each device due to variability in the direct writing of the Pluronic solution. The reservoir microchannels were approximately 6,300 μm apart in the device with ion solutions in pH 6 buffer (Figure 3. 4). However, the distance between two reservoirs with ion solutions in pH 2 buffer was approximately 4,300 μm (Figure 3. 5). We analyzed the nanoparticle synthesized in both devices (see the orange boxes). It is clear that the nanoparticles formed in lower pH solution are less dense than the particles generated in higher pH solution. The dark field images indicate that the reduction reaction is faster and the travel distance is longer for $AuCl_4^-$ ions in higher pH buffer compared to that in lower pH buffer along the swollen POEGA brush pattern. Yet again, the problem of self-reduction of $AuCl_4^-$ ions along the POEGA brushes persist in lower pH buffer.

Figure 3. 5. Dark field optical image of $AuCl_4^-$ and BH_4^- transportation along the linear POEGA pattern and Au nanoparticles formation (aqueous solutions were prepared in pH 2 buffer).

The dependence of ion concentration on nanoparticle formation was observed in a dilute system. In this case, pH 6 buffer solutions of 50 mM $AuCl_4^-$ and BH_4^- ions were introduced to the dual channel device. After 41 hours, the molecular device was imaged (Figure 3. 6). As expected, directed transportation of $AuCl_4^-$ and BH_4^- ions within the POEGA brush nanochannel resulted in development of relatively sparse population of Au nanoparticles.

Figure 3. 6. Dark field optical image of $AuCl_4^-$ and BH_4^- transportation along the linear POEGA pattern and Au nanoparticles formation in a dilute system (aqueous solutions were prepared in pH 6 buffer). Scale bar is 100 μm.

Experimental limitations in directed $AuCl_4^-$ ion diffusion in terms of its uncontrolled self-reduction led us to investigate better alternative chemistries for directed ion transportation such

that the problem of self-reduction of metal ions in the microchannel or along the POEGA brush is eliminated. Therefore, we decided to study the reduction of Cu^{2+} ions with BH_4^-. In this case, one of the microchannels in the dual channel device was filled with aqueous $CuCl_2$ solution (100 mM) whereas the other channel was filled with aqueous $NaBH_4$ solution (100 mM). As shown in Figure 3. 7, Cu^{2+} and BH_4^- ions diffused in the blue and green arrow direction along the linear POEGA brush pattern respectively. The nanoreaction region is indicated by the yellow squares, wherein the Cu nanoparticles were formed.

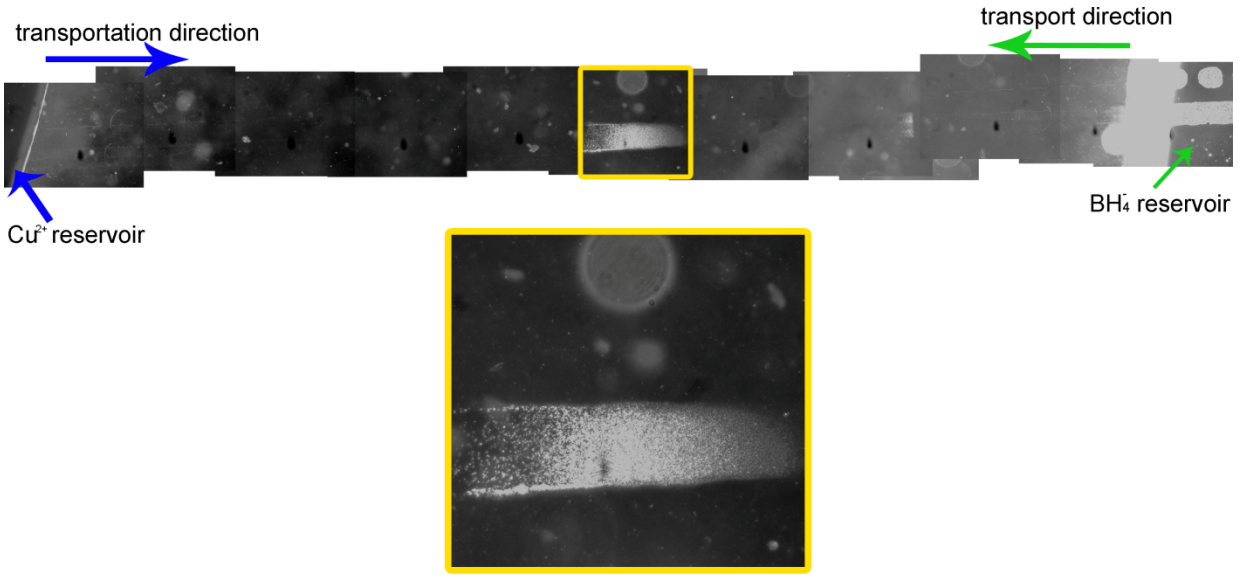

Figure 3. 7. Dark field optical image of Cu^{2+} and BH_4^- transportation along the linear POEGA pattern and Cu nanoparticles formation (aqueous solutions were prepared in Milli-Q water).

In order to investigate the kinetics of Cu^{2+} reduction, a series of molecular devices were prepared. Each device was fabricated such that the separation between the two channels was the same (~3000 μm). Aqueous $CuCl_2$ and $NaBH_4$ concentration was kept constant (100 mM) in each device. Cu nanoparticle formation was monitored by recording dark field optical images every 6 hours as Cu^{2+} and BH_4^- ions diffused along the POEGA brush line. The optical images showed that the formation of Cu nanoparticles can be observed anytime in between 24 hours and 30 hours of diffusion. Figure 3. 8 demonstrates nanoparticles formed by the reduction of

Cu^{2+} ions in the POEGA brush line 30 hours after the introduction of ion solutions into microchannels.

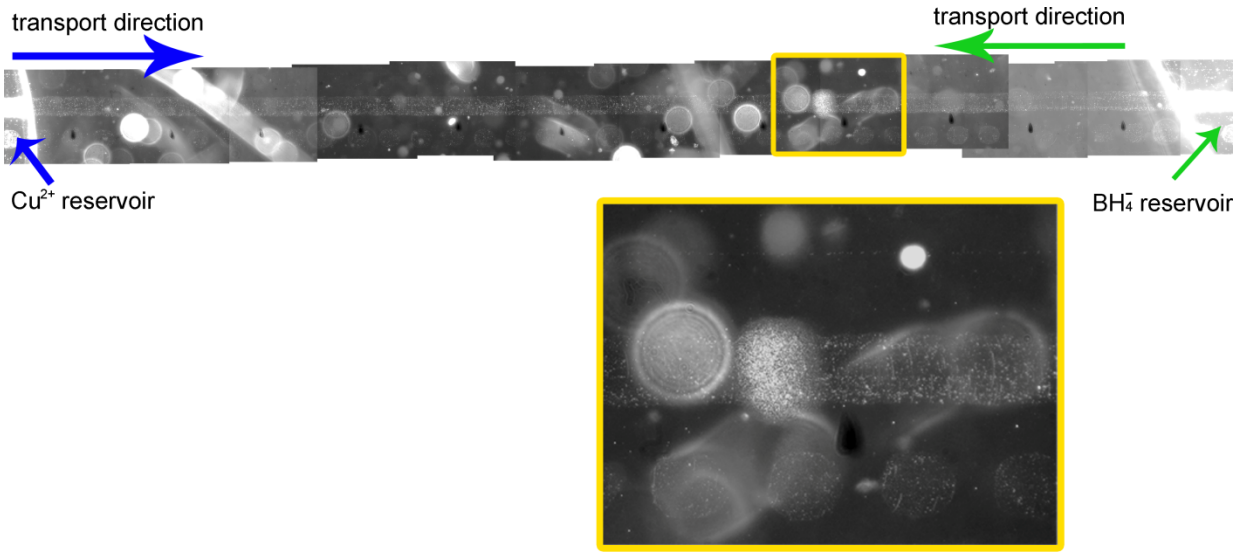

Figure 3. 8. Dark field optical image of Cu^{2+} and BH_4^- transportation along the linear POEGA pattern and Cu nanoparticles formation at the end of 30 hours of diffusion (aqueous solutions were prepared in Milli-Q water).

Studying directed diffusion and reduction of Cu^{2+} ions has significant advantages over the directed diffusion studies of $AuCl_4^-$ chemistry in the molecular devices described in this work. Cu^{2+} solution remained intact in the reservoir throughout the diffusion process. In addition, self-reduction of Cu^{2+} ions was not observed along the POEGA brushes. Despite these important advantages, characterization of the synthesized Cu nanoparticles is a major challenge. We were unable to determine the particle size using diffraction limited optical imaging techniques (Figure 3. 9).

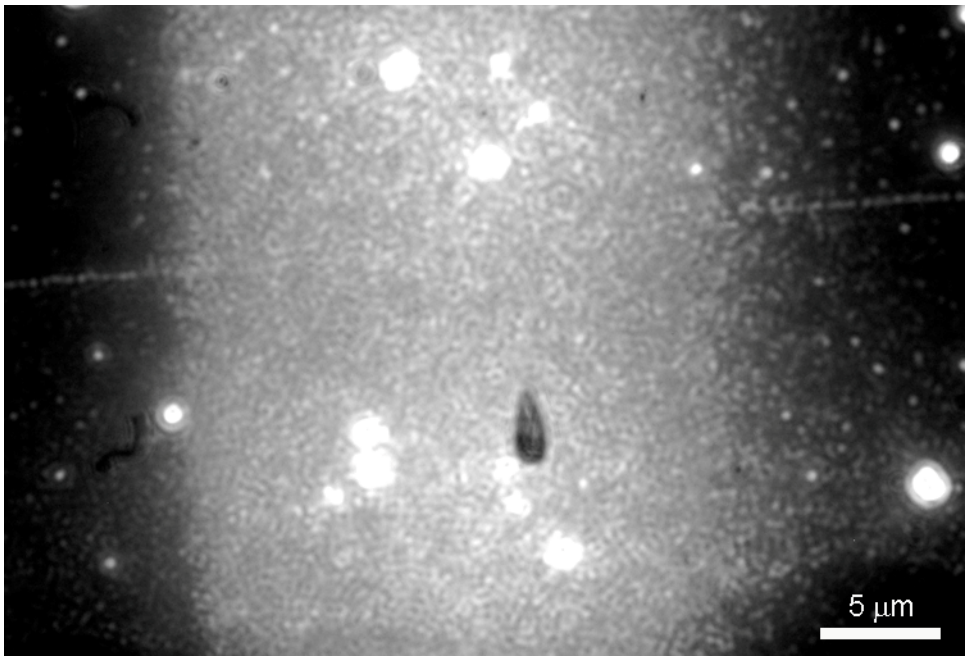

Figure 3. 9. Dark field optical image of Cu nanoparticles at the end of 30 hours of Cu^{2+} and BH_4^- diffusion along the POEGA brush line (aqueous solutions were prepared in Milli-Q water).

On the other hand, transition electron microscopy (TEM) is one of the most efficient tools to characterize nanoparticles. In order to acquire a TEM image of the nanoparticles formed, we need to cut the molecular device and carefully remove Cu nanoparticles from the surface. Despite of the difficulties in the sample preparation, we have observed the Cu nanoparticles under TEM (Figure 3. 10). Similar sample preparation requirement in terms of breaking the molecular device apart applies for the scanning electron microscopy (SEM) imaging. Unfortunately, the image contrast between the patterned and non-patterned regions was so low under SEM and it was hard to find the same location where was imaged with the dark field microscopy.

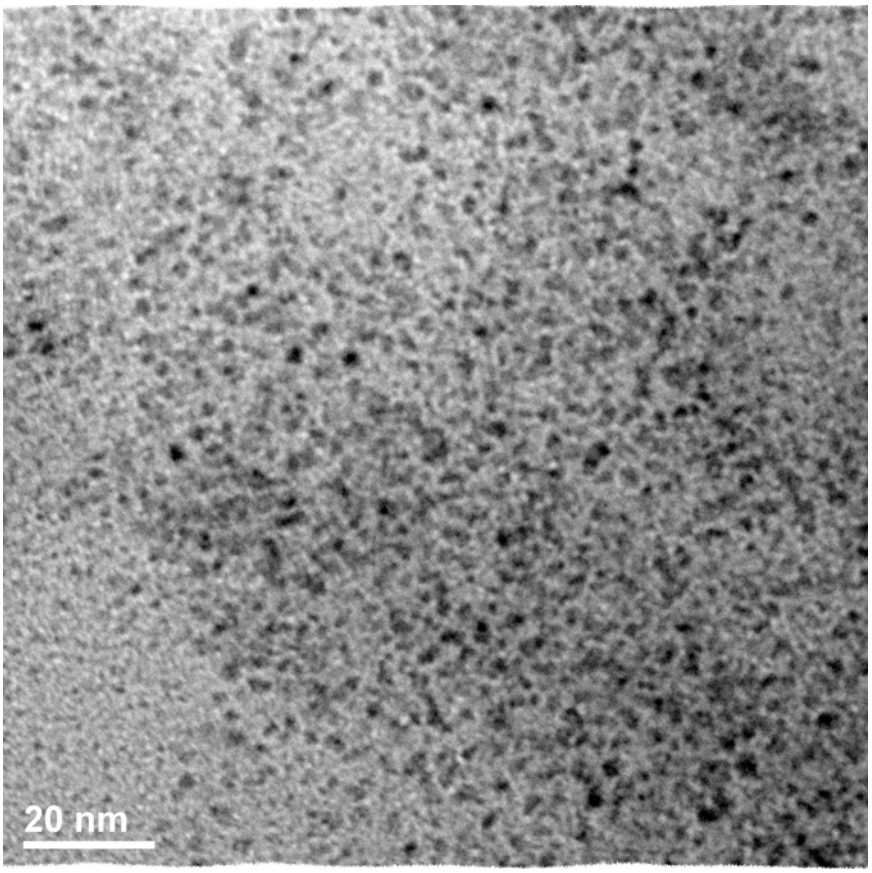

Figure 3. 10. TEM image of Cu nanoparticles synthesized in the molecular device via directed Cu^{2+} and BH_4^- transportation.

3.4 Conclusions

In summary, directed transport of metal ions was investigated on solid surfaces. Successful visualization of ion transportation was achieved by imaging metal nanoparticles that were generated by metal ion reduction in the presence of reducing agent. The implementation of this type of directed ion transport mainly required new designs for molecular devices that provide reservoir for two reactive ionic species: metal ion and reductant solutions. However, the molecular device brought some limitations like uncontrolled metal ion reduction along the diffusion pathways or inside the reservoir. An alternative chemistry, Cu^{2+} and BH_4^- ions, was more compatible with the molecular device and hasn't exhibited such critical issues. We obtained a very rapid diffusivity for Cu^{2+} ions (~3000 μm travelled distance in approximately 30

hours) compared to the diffusivity of the probe molecule found in the previous chapter. This speed is reasonable for such a small molecule [21]. However, more detailed ion diffusivity calculations for this system should involve the relative diffusivity of the reacting ions in the dual channel device, the kinetics of the reduction reaction, and the critical ion concentration that is required for growing the seed particles. The next step to move this work forward will be to generate on-chip nanoreaction platforms that can produce various sized nanoparticles in a single device.

3.5 References

1. Turkevich, J., Stevenson, P. C., Hillier, J., Discuss. Faraday Soc., 1951, 11, 55.
2. Creighton, J. A., Blatchford, C. G., Albrecht, M. G., Journal of the Chemical Society-Faraday Transactions Ii, 1979, 75, 790.
3. Scott, R. W. J., Ye, H. C., Henriquez, R. R., Crooks, R. M., Chemistry of Materials, 2003, 15, 20, 3873.
4. Sinha, A., Das, S. K., Kumar, T. V. V., Rao, V., Ramachandrarao, P., J. Mater. Synth. Process., 1999, 7, 6, 373.
5. Sastry, M., Patil, V., Mayya, K. S., Paranjape, D. V., Singh, P., Sainkar, S. R., Thin Solid Films, 1998, 324, 1-2, 239.
6. Hou, Y. L., Gao, S., Journal of Materials Chemistry, 2003, 13, 7, 1510.
7. Sarathy, K. V., Kulkarni, G. U., Rao, C. N. R., Chemical Communications, 1997, 6, 537.
8. Terrill, R. H., Postlethwaite, T. A., Chen, C. H., Poon, C. D., Terzis, A., Chen, A. D., Hutchison, J. E., Clark, M. R., Wignall, G., Londono, J. D., Superfine, R., Falvo, M., Johnson, C. S., Samulski, E. T., Murray, R. W., J. Am. Chem. Soc., 1995, 50, 12537.
9. Yamamoto, M., Nakamoto, M., Chem. Lett., 2003, 32, 5, 452.
10. Lemon, B. I., Crooks, R. M., J. Am. Chem. Soc., 2000, 122, 51, 12886.
11. Zhao, H. Y., Douglas, E. P., Chem. Mat., 2002, 14, 3, 1418.

12. Youk, J. H., Park, M. K., Locklin, J., Advincula, R., Yang, J., Mays, J., Langmuir, 2002, 18, 7, 2455.
13. Zhang, J. G., Xu, S. Q., Kumacheva, E., J. Am. Chem. Soc., 2004, 126, 25, 7908.
14. Azzaroni, O., Brown, A. A., Cheng, N., Wei, A., Jonas, A., M., Huck, W. T. S., Journal of Materials Chemistry, 2007, 17, 32, 3433.
15. Costantini, F., Benetti, E. M., Tiggelaar, R. M., Gardeniers, H. J. G. E., Reinhoudt, D. N., Huskens, J., Vancso, G. J., Verboom, W., Chemistry-a European Journal, 2010, 16, 41, 12406.
16. Calvo, A., Cecilia F. M., Yameen, B., Williams, F. J., Azzaroni, O., Soler-Illia, G. J. A. A., Langmuir, 2010, 26, 8, 5559.
17. Daniel, M.C., Astruc, D., Chem. Rev., 2004, 104, 1, 293.
18. Dung, T. M., Advances in Natural Sciences: Nanoscience and Nanotechnology, 2011, 2, 1, 015009.
19. Sakai, T., Alexandridis, P., J. Phys. Chem. B, 2005, 109, 16, 7766.
20. Longenberger, L., Mills, G., J. Phys. Chem., 1995, 99, 2, 475.
21. Phillips, H. O., Marcinkowsky, A. E., Sachs, S. B., Kraus, K. A., J. Phys. Chem., 1977, 81, 7.

CHAPTER 4

PROTEIN ADSORPTION ON POLY(*N*-ISOPROPYLACRYLAMIDE) BRUSHES: DEPENDENCE ON GRAFTING DENSITY AND CHAIN COLLAPSE

Significant portions of this chapter were accepted to be published as:

Changying Xue, Nihan Yonet-Tanyeri, Nicolas Brouette, Michele Sferrazza, Paul V. Braun, and Deborah E. Leckband, Protein Resistant Poly(*N*-isopropylacrylamide) Brushes, Langmuir, 2011.

4.1 Introduction

Stimulus-responsive materials such as the temperature-responsive polymer poly(*N*-isopropylacrylamide) (PNIPAM) are used in numerous applications, including biosensors, protein purification, drug delivery, and tissue engineering [1-13]. PNIPAM, in particular, undergoes a solubility switch under mild conditions at its lower critical solution temperature (LCST) of 32°C, such that the polymer swells in water below the LCST, but becomes less soluble and collapses above the LCST. With a transition near physiological temperature and at neural pH, PNIPAM has broad potential for applications in biotechnology and the clinic.

Cell-sheet engineering is a notable example [14]. In this case, cells adhere to PNIPAM at 37°C, to form confluent cell sheets that can be detached intact, simply by decreasing the temperature, and without compromising the monolayer integrity [14-24]. The assumption is that above the LCST, cells attach to protein adsorbed on the presumably collapsed, hydrophobic polymer. Below the LCST, the polymer is predicted to be more hydrophilic and to swell in water, causing protein lift-off and cell detachment.

Several applications are founded on the assumption that substantial changes in the interfacial properties of PNIPAM coatings associated with this collapse transition promote reversible protein adsorption. The collapsed chains presumably adsorb protein, whereas the water-swollen state below the LCST is assumed to repel protein. Nevertheless, an increasing number of reports suggest that PNIPAM brushes do not always exhibit a collapse transition

above the LCST, and that proteins do not adsorb to all PNIPAM coatings. For example, PNIPAM spin-coated onto pre-conditioned silicon wafers did not adsorb human serum albumin, either above or below the LCST [25]. Cell attachment on PNIPAM hydrogels polymerized by electron beam irradiation on tissue culture polystyrene or on glass depends on the gel thickness, with thicker gels repelling cells above and below the LCST [26-28]. Cell adhesion requires adsorbed protein. In the latter example, fibronectin adsorbed on thin (15-20 nm) PNIPAM gels but not on thick (> 30 nm) coatings, despite the 10 degree increase in the water contact angle on the dry, thick gels above the LCST [27, 28]. On the other hand, plasma deposited PNIPAM coatings reversibly adsorb protein above the 32°C, regardless of film thickness [26, 29, 30].

Defining design rules for thermoresponsive coatings requires identifying key parameters governing the interfacial properties of PNIPAM and its interaction with proteins. This is challenging with some fabrication methods. However, chains grafted from immobilized initiators using atom transfer radical polymerization (ATRP) enable good control of grafting densities and molecular weights. This in turn facilitates investigations of the impact of these parameters on the thermally driven collapse transition, and on the mechanism and extent of protein adsorption. Prior studies with PNIPAM grafted from alkanethiols on gold showed that their temperature-dependent collapse transition depends on the polymer molecular weight and grafting density [31, 32]. This intriguing finding suggested that some PNIPAM brushes might remain protein resistant above the LCST, and motivated the present investigation of the impact of grafting parameters on protein adsorption onto PNIPAM brushes.

Here, ATRP was used to generate controlled PNIPAM brushes. The results document the influence of brush architecture on i) the temperature-dependent collapse of PNIPAM brushes grafted from silicon wafers and ii) temperature-dependent protein adsorption onto those brushes. Ellipsometry, use of radio-isotope-labeled proteins, and fluorescence measurements in turn determined protein adsorption as a function of the brush architecture and temperature.

4.2 Experimental

4.2.1 Materials

N-isopropylacrylamide (NIPAM), and 1,1,4,7,7-pentamethyldiethylenetriamine (PMDETA) were purchased from Acros. NIPAM monomer was re-crystallized from hexane. 2-[methoxy(polyethyleneoxy)propyl]-trimethoxysilane (OEG) was from Gelest Inc. CuBr, methanol and anhydrous toluene were purchased from Aldrich. The initiator, 11-(2-Bromo-2-methyl)-propionyl undecyl trichlorosilane, was synthesized as described [33]. Chicken egg white lysozyme and human serum albumin (HSA) were purchased from Sigma Aldrich. All aqueous solutions were prepared with Milli-Q purified water (Millipore, Bedford, MA) with a resistivity of 18.2 MΩ•cm.

4.2.2 Surface-Initiated Polymerization of *N*-Isopropylacrylamide Brushes

The poly(*N*-isopropylacrylamide) (PNIPAM) brush was synthesized by surface-initiated atom transfer radical polymerization (ATRP) of *N*-isopropylacrylamide from initiator functionalized silicon substrates, according to published procedures [31]. First, silicon wafers were cleaned in piranha solution (25% (v/v) hydrogen peroxide and 75% (v/v) sulfuric acid) at 60°C for 1 hour. (*Warning: piranha solution can react strongly with organic compounds. It should be handed with extreme caution and it should not be stored in closed containers.*) The silicon wafers were then rinsed with deionized water and dried under a stream of nitrogen. Next, self-assembled monolayers of the initiator (SAM-Br) and 2-[methoxy(polyethyleneoxy)propyl]-trimethoxysilane (SAM-OEG) were formed on the substrates by immersing the clean silicon wafers in a toluene solution containing 2 mM mixtures of the initiator and OEG for 4 hours. Substrates with different SAM-Br surface densities were prepared by adjusting the molar percentages of SAM-Br and SAM-OEG in solutions used to assemble the monolayers. After cleaning and drying, the substrates then were placed in a reaction vessel and degassed with

three freeze-pump-thaw cycles. NIPAM (3.955g, 35 mmol) was dissolved in a mixture of MeOH/H_2O (v/v:7/3) and degassed with nitrogen for 1 hour [31]. The catalyst, CuBr (50.75 mg, 0.35 mmol), and the ligand, PMDETA (227.92 µL, 1.05 mmol), were then added to the monomer solution. This mixture was transferred, via a cannula, into the reaction vessel containing the silicon wafers functionalized with only SAM-Br or with a SAM-Br: SAM-OEG mixture. The polymerization reaction was at room temperature under a nitrogen atmosphere, for specified times. After the reaction, the vessels were disconnected from the nitrogen line and the substrates were rinsed with methanol, followed by sonication in methanol, ethanol, and then water before drying under a stream of nitrogen.

4.2.3. Ellipsometric Determination of PNIPAM Brush Thickness

The thickness of the PNIPAM brushes was measured with a Gaertner ellipsometer (Model L116C) and LGEMP software (Gaertner Scientific Corp, USA). The incident angle of 632.8 nm light was 70° in all experiments. The refractive index and extinction coefficient of the clean silicon wafer were 3.85 and -0.02, respectively. The PNIPAM brush thickness on the silicon wafer was obtained by fitting the data to a single-layer box model. The native oxide thickness was subtracted to give the monolayer thickness. For thickness measurements in air, a refractive index of 1.46 was used for the organic layer. Three measurements were done at each of six different locations on each sample. A custom-built environmental cell was used to vary the temperature, in order to study the temperature response of the PNIPAM brushes in water. The temperature was increased at a rate of ~0.5°C/min. Given the rapid polymer response to temperature changes, this should be sufficient to enable brush equilibration during the heating cycle [34, 35]. Thicknesses and refractive indices of the water swollen PNIPAM films were also determined by ellipsometry, as a function of temperature.

4.2.4 Contact Angle Measurement

The advancing water contact angle on the different dry PNIPAM brushes was measured with a Ramè-Hart goniometer (Model 100-00) in a temperature-controlled room (± 0.2°C). The advancing static water contact angles were measured for each water droplet at room temperatures and at 37°C. Measurements were taken from several different positions on each substrate, and the average of these values was determined.

4.2.5 X-Ray Photoelectron Spectroscopy (XPS)

The surface chemical composition was determined by XPS, using a Kratos Axis ULTRA spectrometer with monochromatic Al Kα radiation at 1486.6 eV (225W, 40 eV pass energy) at a pressure of 10^{-9} Torr. The samples were loaded on a rectangular metal support, using double-sided adhesive tape. The C 1s hydrocarbon peak at 285.0 eV was used as the reference peak for all binding energy measurements. Surface chemical compositions were obtained from the integrated area under the peaks in the XPS spectra, normalized with the appropriate sensitivity factors.

4.2.6 Ellipsometric Determination of Adsorbed Protein on PNIPAM Brushes

The proteins investigated were chicken egg white lysozyme (Sigma Aldrich - L6876) and human serum albumin (HSA, Sigma Aldrich - A9511). Lysozyme is small and positively charged at neutral pH (pI = 10.9), while HSA is a larger, negatively charged protein (pI = 4.4), and the predominant globular protein in serum. The proteins were dissolved in phosphate buffered saline (pH 7.0, ionic strength 0.1).

The instrument used for these studies is a Horiba Jobin–Yvon MM-16 spectroscopic phase modulated ellipsometer. The light sources are halogen and LED lamps with the wavelength range 430-850 nm. Measurements were performed near the Brewster angle at an incident angle of 70°. All measurements were obtained over the entire spectral range.

The samples were contained in a home built cell used for *in situ* studies of protein adsorption at solid/liquid interfaces. The incident light enters the liquid via a thin glass window, reflects from the solid/liquid interface, and is detected after passing through another thin glass window. The temperature is regulated by a thermostatic water bath that circulates water at the base of the cell. The lid consists of poly(tetrafluoroethylene).

The adsorbed amount of protein Γ (mg/m^2) was determined from [36]:

$$\Gamma = \frac{h(n-n_0)}{10(dn/dc)} \quad \text{(Eq. 4. 1)}$$

where *h* is the thickness (in Å) of the layer (box) in which the protein is adsorbed, n_0 is the refractive index of the medium in the thin layer before protein insertion, *n* is the refractive index of the medium with adsorbed protein, and *dn/dc* is the refractive index increment of the protein (mL/g). In the case of protein insertion into the brush, *h* is the brush thickness, n_0 is the refractive index of the brush without protein and *n* is the refraction of the brush with adsorbed protein. Both for the lysozyme and HSA, dn/dc is about 0.19 mL/g [37].

A 1 mg/mL or 3.5 mg/mL solution of lysozyme was injected into the cell containing the PNIPAM brush. The PNIPAM samples were immersed into the protein solution, order to avoid flushing, which could disturb the brush and prevent weak protein adsorption. The PNIPAM brushes were first incubated with the protein solution at a given temperature (25°C or 37°C) for up to 5 hours to equilibrate the system, and then the solution was heated to 37°C or cooled to 25°C, respectively. The protein absorption onto the PNIPAM brushes was monitored as a function of the temperature change.

4.2.7 Radio-assays of Adsorbed Protein

To detect protein levels below the detection limit of ellipsometery, BSA adsorption on PNIPAM brushes was quantified with 125-iodine-labeled protein. BSA was iodinated with Iodobeads (Pierce) and carrier free Na^{125}[I] (Perkin Elmer). The labeled protein was desalted

with a PD-10 column (GE Healthcare Bioscience) to remove unbound ^{125}[I], and the determined specific activity of labeled protein was 25-30 cpm/ng.

Replicate (N = 4) samples were affixed with SecureSeal™ Imaging Spacers (Grace Biolabs) with a 13 mm circular cutout. This constrained the sample within a well-defined area. The sample was then overlayed with 200 μL of labeled BSA (1mg/mL). The incubation was carried out for 2 hours at 23°C (room temperature) or at 37°C in an incubator. After the incubation, the solution was gently aspirated, and the samples were rinsed ten times by displacement with 100 μL buffer that was maintained at the incubation temperature. That is, for samples heated to 37°C, the buffer and sample were maintained at 37°C during all rinsing steps, to prevent brush reswelling. Substrates were placed in vials containing 5 mL of scintillation cocktail and the counts were recorded with an LS 6500 scintillation counter (Beckman Instruments) with specified settings for 125-iodine detection. Control measurements were with oligoethylene oxide terminated silane monolayers. Each set of measurements was repeated to insure reproducibility.

4.2.8 Patterned PNIPAM Brush Formation

To visualize temperature-dependent differences in protein adsorption on the PNIPAM brushes above and below the LCST, patterns of the initiator were microcontact printed on clean glass slides. For comparison, we similarly patterned OEG-SAMs. A second, positive control used octadecyl trimethoxy silane (OTS) patterns with the non-patterned region backfilled with OEG-SAM. Stamps were fabricated by casting a mixture of poly(dimethyl siloxane) (PDMS) prepolymer and curing agent (v/v:10/1) onto the silicon master that was photolithographically patterned. The PDMS was cured overnight at 65°C.

Silicon (111) wafers and glass substrates were cleaned in piranha solution for 1 hour. After rinsing with excess ultra pure water (18.2 MΩ•cm), substrates were dried with a steam of

nitrogen. Silicon wafers were used for reference thickness measurements of patterned PNIPAM brushes. Glass slides were used for obtaining fluorescence microscopy images of PNIPAM patterns, after incubation with fluorescein isothiocyanate (FITC) labeled albumin. The image was obtained with a Zeiss Axiovert 200 M fluorescence microscope (Thornwood, NY).

The PDMS stamp was inked with a 10 mM solution of the initiator in hexane and dried with a steam of nitrogen for 3 seconds. The inked PDMS was brought contact with a clean silicon wafer (or glass) for 10 seconds. Subsequently, the initiator-printed surface was washed with ethanol and dried with nitrogen. For backfilled samples, the unprinted regions were coated with OEG silane by immersing the substrates in a 2 mM toluene solution of OEG silane for 1 hour at room temperature. Finally, surfaces were washed with toluene, ethanol, and then deionized water, before drying with nitrogen. Patterned PNIPAM brushes were grown from patterns of SAM-Br by following the same procedure as the non-patterned PNIPAM brushes, except that the polymerization took place for 2 hours.

4.2.9 Statistical Analyses

The student's t-test was used for pairwise comparisons of data [38]. The difference between two measurements was considered to be statistically significant, if $p < 0.05$.

4.3 Results and Discussion

Self-assembled monolayers of the initiator (SAM-Br) and OEG (SAM-OEG) were first characterized by ellipsometry. The measured values for the SAM-Br and SAM-OEG monolayer are 18 ± 2 Å and 12 ± 1 Å respectively, and compare well with prior studies [39, 40].

To control the initiator coverage, SAMs were prepared from mixtures of initiator silane and OEG silane. The surface composition of the mixed initiator:OEG monolayers was determined by XPS (Figure 4. 1). Table 1 shows the surface densities of the initiator (#/nm^2) determined for the mixed-SAMs, as a function of the solution composition of the mixture from

which the monolayers were assembled. The decreasing amount of initiator on mixed SAMs with decreasing percentage of initiator in solution demonstrates the ability to control the initiator surface density. The SAM-Br surface coverage does not depend linearly on the mole percent of the initiator in the initiator/OEG solutions. This may reflect differences in their relative diffusivity and reactivity.

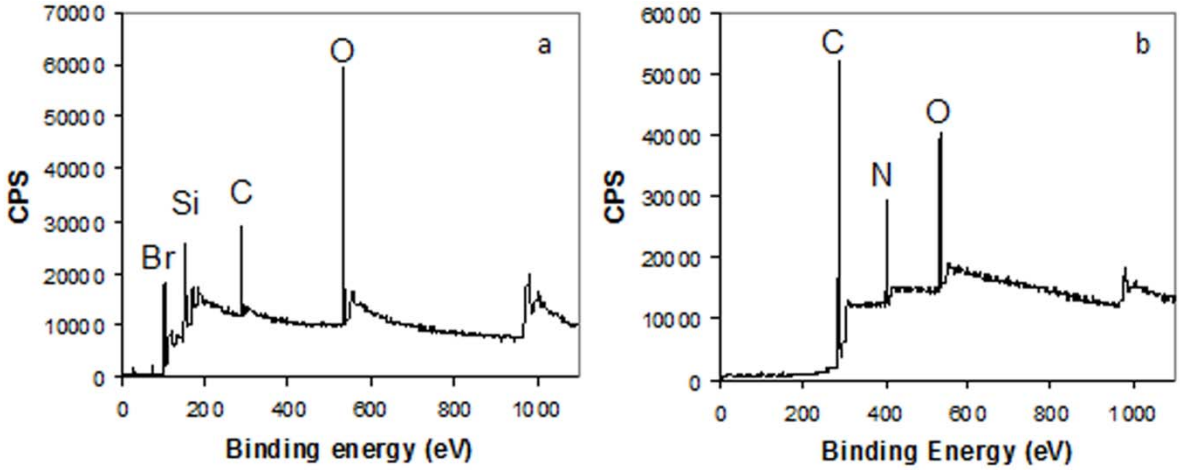

Figure 4. 1. XPS spectra of a self-assembled monolayer of initiator silane on a silicon wafer before (a) and after (b) the polymerization of PNIPAM from the monolayer.

Table 4. 1. Surface chemical composition of self-assembled silane monolayers on silicon wafers, determined by XPS. The initiator coverage was estimated from the Br/Si ratios.

Mole% of SAM-Br in solution of SAM-Br and SAM-OEG	O	C	Si	Br	Br/Si	SAM-Br Coverage	σ(#/nm^2)
100	22.37	30.52	44.6	2.51	0.056	100%	2.1
80	26.24	20.93	51.19	1.64	0.032	57.1%	1.1
50	26.14	20.28	52.22	1.35	0.0259	46.3%	0.9
20	26.28	23.46	49.21	1.06	0.0215	38.4%	0.8

PNIPAM brushes were then synthesized from surfaces that were functionalized with SAM-Br or mixed SAM-Br:SAM-OEG. A comparison of XPS spectra before and after polymerization in Figure 4. 1 showed that the nitrogen peak appears and the bromide peak disappears after polymerization, which indicates that PNIPAM has been grafted on surface. Table 4. 2 summarized the thicknesses of dry and water swollen PNIPAM brushes. The wet brush thicknesses were determined at 23°C and 37°C. The swelling ratio, which is the ratio of the hydrated PNIPAM thickness to dry PNIPAM brush thickness at 23°C, increases with decreasing grafting density (Table 4. 2). This trend might be expected since the chains in more densely packed brushes are already highly stretched and should swell less upon full hydration. The decrease in refractive index (Figure 4. 2a) with decreasing initiator density also agrees with the expected increase in the water content of the more dilute chains. In addition, from the estimated initiator densities and dry film thicknesses, the molecular weight of the grafted PNIPAM was estimated from Eq. 4. 2:

$$\sigma = \frac{h\rho N_A}{M_n} \qquad \text{(Eq. 4. 2)}$$

Here, σ is the chain density, determined from the surface density of initiator and chain initiation efficiency, h is the measured brush thickness (Å), ρ is the density of dry NIPAM, N_A is Avogadro's number, and M_n is the number average molecular weight of the chains. The surface coverage σ and M_n (Table 4. 3) were estimated from XPS data, the maximum packing density of 2.1 bromine initiator/nm^2, a monomer density of 0.95 mg/cm^3, and a chain initiation efficiency of ~10%, reported for polystyrene [41-43].

Table 4. 2. Determined thicknesses of dry and water swollen PNIPAM brushes, after subtracting the alkane monolayer thickness.

Mole% Initiator in the mixture of OEG and initiator (polymerization time)	Initiator monolayer (Å)	Dry film thickness (Å) at 23°C	Wet film thickness (Å) at 23°C	Wet film thickness (Å) at 37°C	Swelling ratio at 23°C
100 (2 hours)	18 ± 1	707 ± 4	1043 ± 4	876 ± 16	1.5
100 (10 min)	18 ± 1	352 ± 2	668 ± 9	519 ± 3	1.9
80 (10 min)	16 ± 1	243 ± 1	652 ± 3	516 ± 3	2.7
50 (10 min)	16 ± 1	134 ± 1	594 ± 11	484 ± 3	4.4
50 (4min)	16 ± 1	76 ± 5	490 ± 20	491 ± 7	6.5
20 (10 min)	12 ± 1	62 ± 2	490 ± 40	488 ± 8	7.9

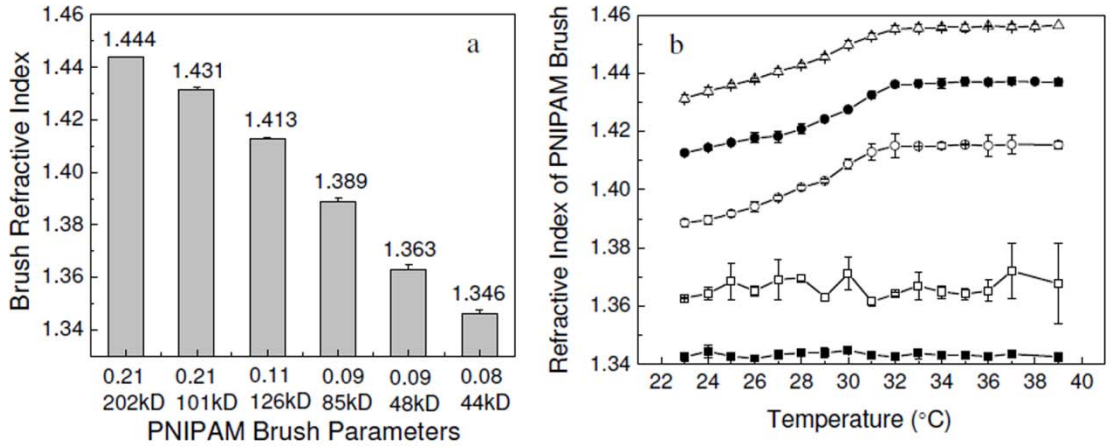

Figure 4. 2. (a) The measured refractive indices of the PNIPAM brushes in pure water at 23°C, and (b) the measured changes in refractive indices of the PNIPAM brushes in pure water as a function of temperature. The curves correspond to different brush preparations: black squares (0.08 chains/nm^2, 44 kDa); open squares (0.09 chains/nm^2, 48 kDa); open circles (0.09 chains/nm^2, 85 kDa); black circles (0.11 chains/nm^2, 126 kDa); open triangles (0.21 chains/nm^2, 101 kDa).

Table 4. 3. Summary of poly(*N*-isopropylacrylamide) brush parameters.

Mole% Initiator in mixture of OEG and initiator (reaction time)	Estimated grafting density (#/nm^2)	Estimated Molecular Weight (g/mol)	Degree of polymerization	R_F (Å)	s (Å)	s/(2R_F)	Config-uration
100 (2 hours)	0.21	202,000	1789	268	22	0.04	brush
100 (10 min)	0.21	101,000	891	176	22	0.06	brush
80 (10 min)	0.11	126,000	1118	202	30	0.07	brush
50 (10 min)	0.09	85,000	753	159	33	0.10	brush
50 (4 min)	0.09	48,000	427	113	33	0.15	brush
20 (10 min)	0.08	44,000	392	107	35	0.16	brush

To determine whether the grafted polymers are in the brush regime, we calculated the distance between grafting sites **s** relative to the Flory radius $R_F = L \bullet n^{3/5}$, assuming that water at 23°C is a good solvent for PNIPAM [44]. Here L is the estimated monomer size (~3 Å), and n is the polymerization degree. If **s** << 2R_F, then the chains form stretched brushes [44]. The values of R_F and distances between grafting sites **s** = $\sigma^{-1/2}$ are in Table 4. 3. Based on these calculations, all PNIPAM preparations used here produced brushes.

A comparison of the distance between grafting sites relative to the protein dimensions also determined the feasibility of primary protein adsorption by penetrating the brush to adsorb on the underlying substrate [45]. The dimensions of lysozyme are 45×35×35 Å and those of HSA are 140×40×40 Å, such that, even at the lowest grafting density, the chain density and molecular weight should be sufficient to repress primary adsorption [45]. Proteins could still penetrate the brush (ternary adsorption), but they would not likely adsorb to the underlying surface.

The dry PNIPAM brushes were characterized with advancing water contact angle measurements at 37°C and at 23°C (Figure 4. 3). Advancing water contact angles generally tracked with the extent of the brush collapse above 32°C. The difference in contact angles above and below the LCST was greatest with the PNIPAM brush at the highest grafting density, and then decreased somewhat with decreasing grafting density. However, no change was observed with the most dilute brush (0.08/nm^2) or with the lower molecular weight PNIPAM synthesized at the intermediate initiator density (0.09/nm^2; Table 4. 3).

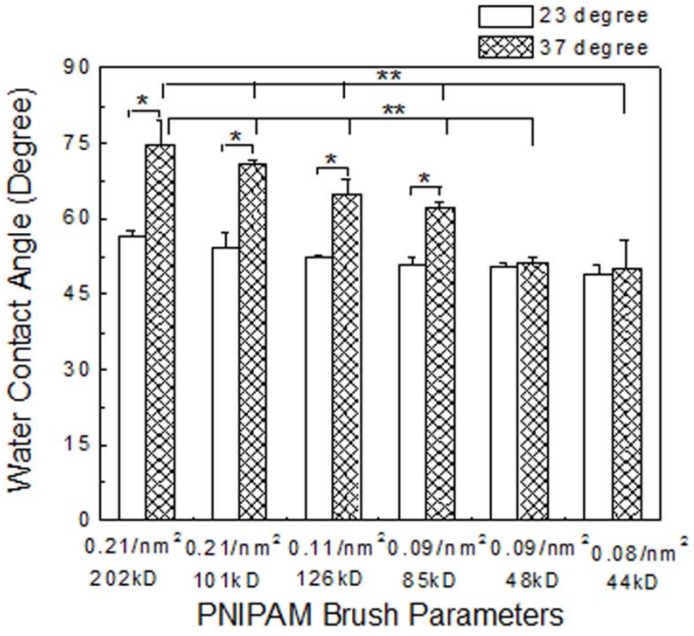

Figure 4. 3. Advancing water contact angle on dry PNIPAM brushes at 23°C and 37°C. Here * indicates a significant difference between the values measured at 23°C and 37°C for each sample ($p < 0.001$), and ** indicates a significant difference between the water contact angle at 37°C on the low density brush (0.08 chains/nm^2 at 44 kDa or 0.09 chains/nm^2 at 48 kDa) relative to the other samples ($p < 0.01$).

Figure 4. 4 shows the measured thickness of the water swollen PNIPAM brushes at increasing temperatures. Two observations can be made. First, changes in the hydrated thicknesses similarly depended on the chain grafting density, when PNIPAM was synthesized under otherwise identical conditions. Different from the swelling ratios at 23°C, chains at the higher grafting densities exhibited the greatest decrease in brush thickness above 32°C. The

thickness changes of the two most densely packed brushes were similar, and refractive index changes (Figure 4. 2b) suggest a decrease in the water content of the brushes. There was no apparent change in the thickness of swollen chains grafted from the least dense initiator monolayers (0.08/nm^2). The initial thickness of PNIPAM at the intermediate grafting density (0.09/nm^2) was less than brushes grafted from initiator densities of 0.11/nm^2 and 0.21/nm^2, as expected, and the brush similarly collapsed above the LCST. PNIPAM grafted from SAM-Br at 0.09/nm^2 appears to lie at a crossover between two regimes: namely, higher molecular weight chains (~85 kDa) collapsed above the LCST, but the thinner monolayers (~48 kDa) remained swollen above 32°C. This agrees with a prior report, in which the collapse of PNIPAM grafted from alkanethiols on gold depends on the grafting density and on the polymer molecular weight [31]. Second, for the dense PNIPAM brush, the chain collapse was not abrupt, but exhibited a more gradual decrease over the temperature range of ~26°C to 32°C.

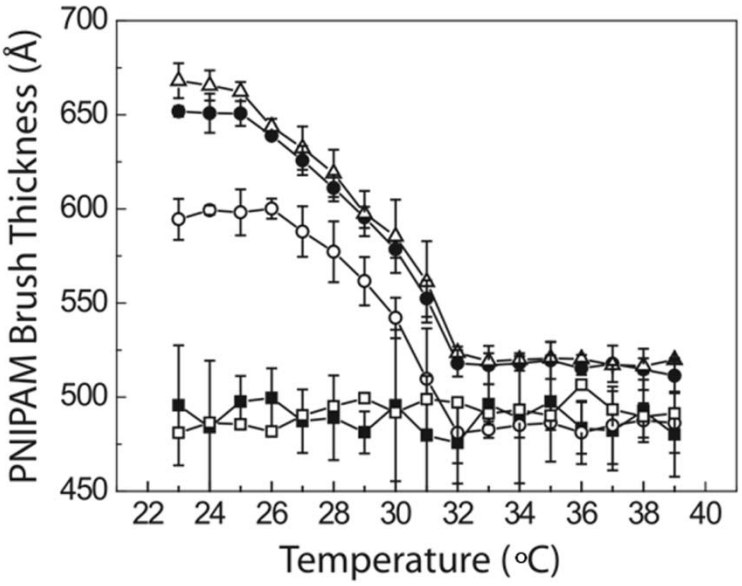

Figure 4. 4. Measured changes in the ellipsometric thickness of PNIPAM brushes in pure water as a function of temperature. The curves correspond to different brush preparations: black squares (0.08/nm^2, 44 kDa); open squares (0.09/nm^2, 48 kDa); open circles (0.09/nm^2, 85 kDa); black circles (0.11/nm^2, 126 kDa); open triangles (0.21/nm^2, 101 kDa).

Next, protein adsorption measurements determined whether the grafting density and molecular weight dependence of the chain collapse generate corresponding differences in

protein adsorption. Control measurements with 100 mole% SAM-OEGs first confirmed that the underlying OEG monolayer is protein resistant. The SAM-OEG regions beneath the brushes should therefore repel the adsorption of both protein and NIPAM. A total of 14 measurements were then carried out with PNIPAM brushes.

Figure 4. 5 shows the difference in the ellipsometric angles Ψ and Δ at 546 nm before and after incubation with the protein solution. The difference is maximal in this wavelength region. In all cases, there was no significant change in the Ψ and Δ spectra before and after incubation with 1mg/mL lysozyme solution. Contrary to expectations, there was no detectable protein adsorption on any of the PNIPAM brushes studied at either 25°C or 37°C [8, 10, 30]. Even with a higher lysozyme concentration (3.5 mg/mL), there were no significant changes in Ψ and Δ. Identical results were obtained with a 1 mg/mL solution of HSA. Two measurements with PNIPAM brushes grafted from dense initiator monolayers (0.11/nm^2) were carried out at initial temperatures of 25°C and at 37°C. In both cases, the thicknesses, refractive indices, and percentages of solvent in the brush were similar to the polymers in the absence of protein.

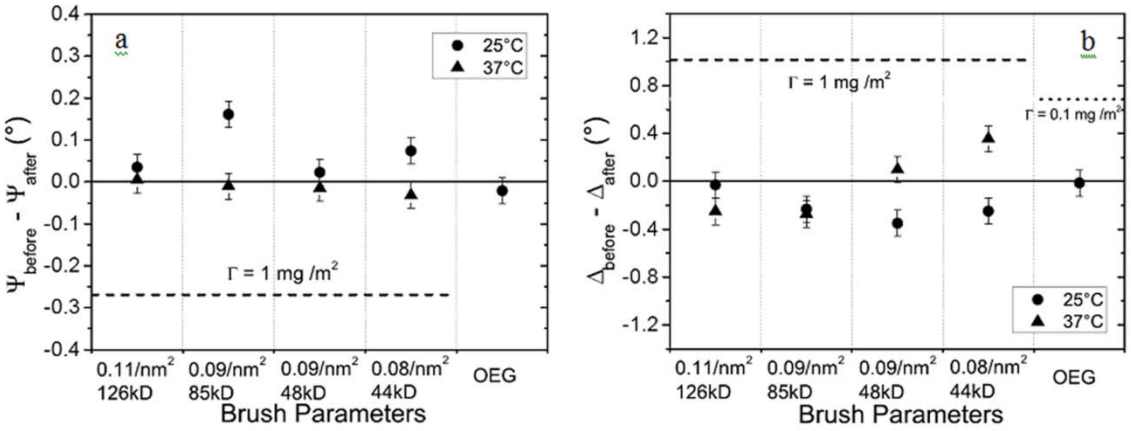

Figure 4. 5. Difference in ellipsometric angles Ψ (a) and Δ (b) determined with incident light at 546 nm, before and after immersion in a 1 mg/mL lysozyme solution. The dashed lines correspond to the simulated values for the adsorbed amount of 1 mg/m^2 on PNIPAM. The dotted line indicates the simulated shift in Δ for 0.1 mg/m^2 adsorbed protein on the OEG monolayer.

Simulations determined the instrument sensitivity to protein adsorption. Changes in Ψ and Δ spectra were simulated for adsorbed protein amounts of 0, 0.5, 1.5, 2.5 and 3.5 mg/m^2 in the PNIPAM brush (Figure 4. 6a). Spectral shifts at Γ = 0.5 mg/m^2 were barely detectable. However, the spectra are particularly sensitive to protein at Γ > 1 mg/m^2. At 1 mg/m^2, Ψ and Δ shift by, respectively 0.269° and 1.016° at 546 nm. These differences could be easily detected by ellipsometry. Comparison of these simulations with experimental data in Figure 4. 5 indicates that any adsorbed protein is below 1 mg/m^2, and supports the experimental finding of negligible protein adsorption on both swollen and collapsed PNIPAM brushes, under the experimental conditions investigated.

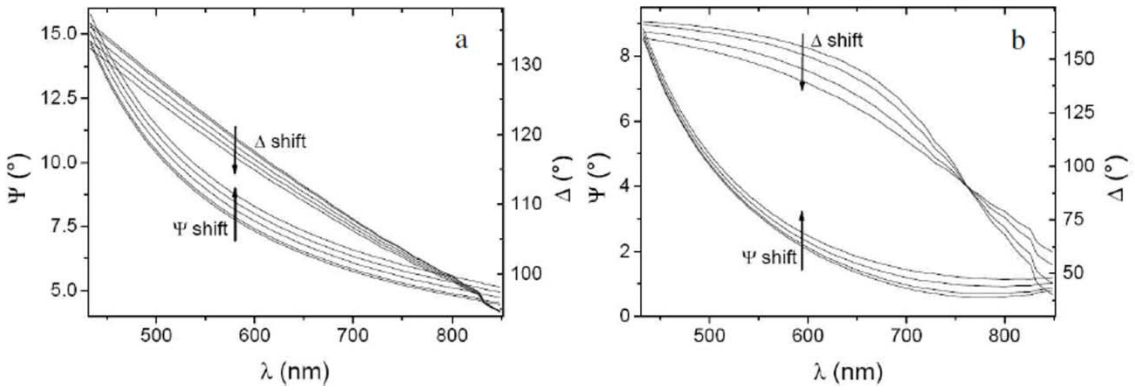

Figure 4. 6. The shift in ellipsometric angles of Ψ and Δ simulated for (a) adsorbed protein amounts of 0, 0.5, 1.5, 2.5 and 3.5 mg/m^2 on the PNIPAM brush, and (b) for adsorbed protein amounts of 0, 0.5, 1.5 and 2.5 mg/m^2 on the OEG.

Simulated ellipsometry data for protein adsorption onto the OEG monolayer at 0, 0.5, 1.5, and 2.5 mg/m^2 (Figure 4. 6b) also confirmed that such measurements would be sensitive to protein adsorption, such that 0.1 mg/m^2 would generate detectable shifts in Ψ and Δ of, respectively, 0.011° and 0.567° at 546 nm (Figure 4. 6b). At 0.1 mg/m^2, the change in Ψ is insignificant, while the change in Δ could be detected easily. Comparison with ellipsometry data indicates that any adsorbed protein on OEG must be Γ < 0.1mg/m^2.

More sensitive radioisotope assays revealed subtle differences in the low protein adsorption on the different brushes. Results are summarized in Figure 4. 7. At 23°C, the amount of adsorbed BSA on the PNIPAM brushes is comparable to the OEG control. Although the adsorbed amount of 20 ± 3 ng/cm^2 on OEG-terminated SAMs is slightly higher than reported by Yu et al., it is comparable to similar reports of protein adsorption on ethylene oxide coated surfaces [46-48].

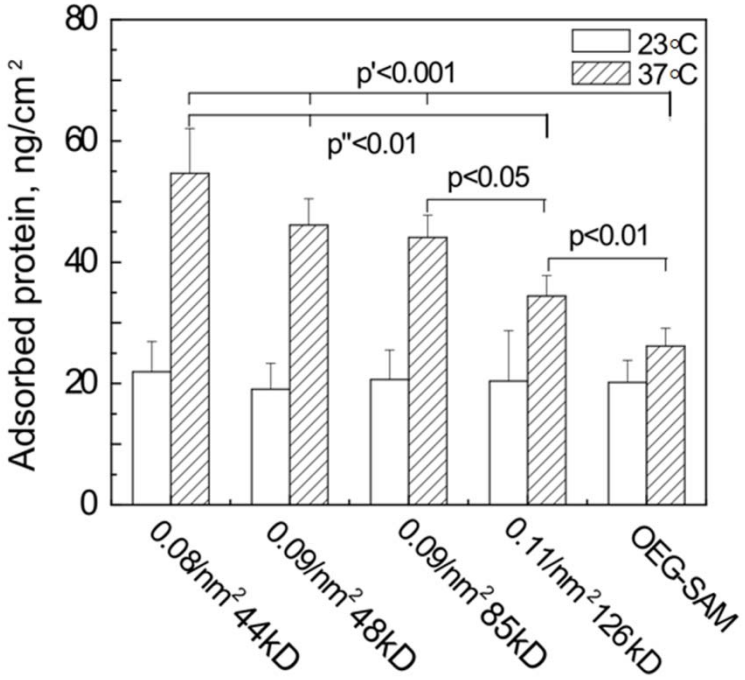

Figure 4. 7. ^{125}[I]-BSA adsorption on PNIPAM brushes at 23°C and at 37°C. The polymer grafting density and molecular weight are indicated below the bars. Adsorption on the OEG-terminated alkylsilane monolayer is shown for comparison. Statistically significant differences ($p < 0.05$) are indicated.

At higher grafting density (0.11 chain/nm^2), the large decrease in the brush thickness at 37°C did not coincide with a corresponding increase in adsorbed protein. The slight measured increase was comparable to that on OEG-terminated films at 37°C and may reflect general, temperature-dependent changes in protein and surface solvation. Conversely, the amount of adsorbed BSA on chains at 0.08/nm^2, which did not collapse at elevated temperatures, increased from 22 ± 5 ng/cm^2 to 55 ± 7 ng/cm^2. This is below the detection limit of ellipsometry.

Interestingly, at the intermediate grafting density (0.09/nm^2), there was no statically significant difference in BSA adsorption on either high or low molecular weight chains, despite differences in the collapse behavior of the different brushes. In both cases, adsorbed BSA was greater than on OEG-terminated monolayers at 37°C, but less than on the more dilute brushes (0.08/nm^2). These findings indicate that protein adsorption on PNIPAM brushes above the LCST is low in all cases. However, observed differences in the amounts of bound protein correspond to decreasing chain density. Adsorption appears to be governed by the capacity of proteins to penetrate the brush and by temperature-dependent changes in segment-solute (protein) interactions, rather than on the chain configuration.

We further visualized the adsorption of fluorescently-tagged BSA onto patterned PNIPAM, above and below the LCST. Patterned PNIPAM brushes do not have the identical grafting density as non-patterned PNIPAM brushes, due to the difference in the SAM-Br preparation methods. Nevertheless, our measurement shows that the PNIPAM brush prepared on the microcontact-printed SAM-Br is around 30 nm.

Images of printed OEG-SAM at 23°C and 37°C, are shown for comparison (Figure 4. 8a, b). The black regions are the patterned OEG and the fluorescence is from protein adsorbed on the uncoated glass. The resulting images obtained with the PNIPAM brush are consistent with the ellipsometry studies of protein adsorption; namely, the polymer patches appear black in the fluorescence images (Figure 4. 8c, d) at both 23°C and 37°C. The background fluorescence shows adsorbed protein on the unmodified glass slide, whereas there is no detectable fluorescence on the PNIPAM pattern at either temperature, similar to patterned SAM-OEG on glass (Figure 4. 8a, b). If the regions surrounding the SAM-Br pattern were instead backfilled with SAM-OEG, prior to polymerization, then there is little detectable fluorescence on the patterns and no contrast between the PNIPAM pattern and SAM-OEG background (not shown). However, fluorescence images obtained with the positive control, comprising printed SAM-OTS

with unprinted regions backfilled with SAM-OEG, show clear fluorescence on the OTS patterns, but no protein in SAM-OEG regions (Figure 4. 8e, f). These results validate the ellipsometry data, and show that the PNIPAM brushes repressed protein adsorption, both above and below the LCST.

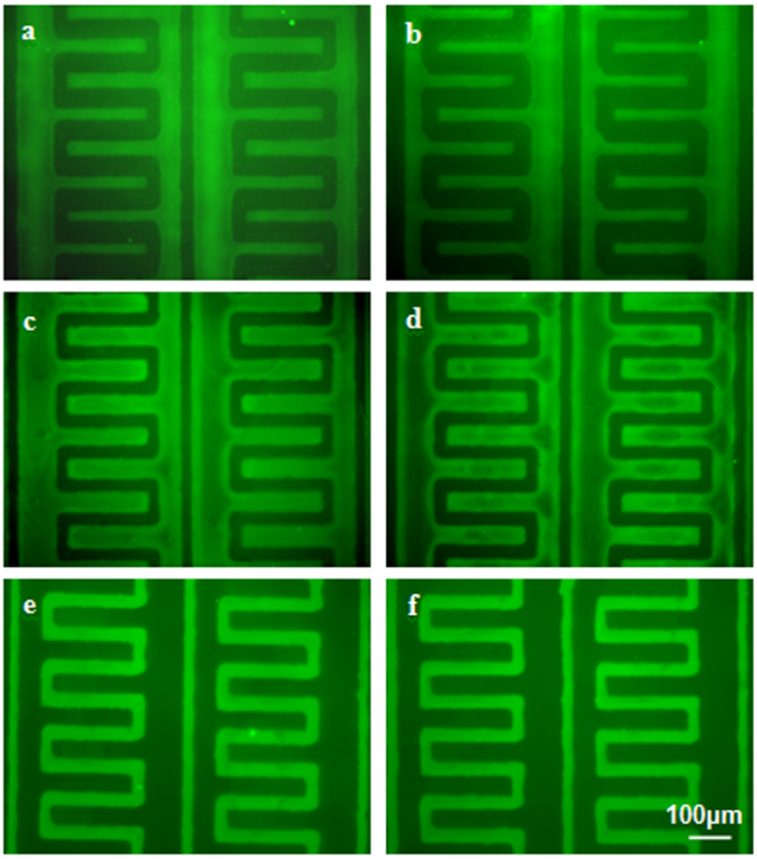

Figure 4. 8. Fluorescence images of adsorbed FITC-BSA (1 mg/mL in 0.01 M PBS buffer) on different micropatterned surfaces at two different temperatures. (a) Microcontact-printed OEG silane (dark zigzag region) on a clean glass substrate at 37°C and (b) at 23°C; (c) Microcontact-printed PNIPAM brush (dark zigzag region) on a clean glass substrate at 37°C and (d) at 23°C; (e) Microcontact-printed OTS on clean glass substrate (bright zigzag), which was backfilled with OEG silane (dark region) at 37°C and (f) at 23°C.

Prior findings by us and by others showed that the thermally driven collapse of PNIPAM brushes depends on the grafting density and molecular weight [31, 49]. These results confirm prior findings, but also show that this transition (or its absence) does not correlate with protein adsorption, under the conditions investigated [31, 49]. These results instead support an

emerging view that the reversible, temperature-dependent adsorption and lift-off of proteins and cells from PNIPAM coatings depend on the film architecture [11, 25, 50].

With grafted polymers, the chain densities and molecular weights (inferred from thicknesses) affect protein adsorption modes, which may include primary adsorption to the underlying surface, secondary adsorption at the outer edge of the brush, or ternary adsorption, involving brush penetration [45]. In this study, the high grafting densities of the brushes would prevent primary adsorption. The most densely packed brushes also appear to suppress secondary and ternary adsorption. At lower grafting densities where BSA could penetrate the brush (ternary adsorption), adsorption increases above the LCST. This suggests the formation of more extensive, attractive protein-segment interactions, which would support increased adsorption.

These results and postulated adsorption mechanisms are consistent with reported cell attachment studies. Other studies did not focus on the impact of chain density or M_w on the polymer collapse, as this study does. However, enhanced cell attachment on dilute (low grafting density) or thin, e.g. low molecular weight brushes above the LCST is consistent with greater ternary or even primary protein adsorption [45].

These studies used a model protein BSA to probe qualitative changes in the interfacial properties of PNIPAM brushes. Altered surface properties, reflected in altered BSA adsorption would similarly impact the adsorption of other proteins, including extracellular matrix proteins that support cell adhesion. Changes in PNIPAM surface properties will necessarily affect all protein adsorption, although the adsorbed amounts of different proteins will differ quantitatively, on account of the variety of shapes, sizes, charge, and melting temperatures which also contribute to protein-surface interactions.

The low protein adsorption on dense brushes differs from the increased protein adsorption on thick films reported by Yu et al [46]. However, these results agree with other reports showing negligible protein deposition and cell attachment on dense, high molecular

weight PNIPAM brushes [50]. The reason for the discrepancy with Yu et al. is presently unclear, but direct comparisons are hindered by the absence of molecular weight or grafting density information in the latter report [46].

Brushes with high PNIPAM grafting densities and molecular weights do not support reversible cell attachment [50-52]. The cell and protein resistance of dense, high molecular weight brushes above the LCST suggest that, despite the difference in water contact angles on dry PNIPAM brushes above the LCST, in water, the collapsed brush presents a hydrophilic, repulsive outer layer.

This outer, hydrated region was proposed previously to account for the unexpected resistance of some PNIPAM films to cell attachment above the LCST [27, 50]. This structure is analogous in some ways to a predicted vertical phase separation, in which more dilute, hydrated chains extend beyond a denser, collapsed core [22, 53-55]. The increased refractive index (Figure 4. 2a) indicates a less polar core, as does steroid and peptide partitioning into PNIPAM coated chromatographic packing materials, above the LCST [1, 5, 10, 11, 12, 22, 52, 56-58]. Force measurements and neutron reflectivity also support the existence of hydrated outer chains [31, 32, 55]. Here, the resistance to protein adsorption is also consistent with the solution stability of PNIPAM particles above the cloud point that is attributed to sterically stabilized polymer aggregates, or mesoglobules [59]. Although the structure and hydration of the outer edge of the dense PNIPAM brushes would be difficult to characterize, the present findings indicate that this region remains hydrophilic and does not present hydrophobic, protein adhesive segments. Instead, greater protein adsorption occurs on more dilute brushes that allow partial penetration and more extensive protein-segment interactions.

4.4 Conclusions

These results demonstrate the ability to control the collapse of PNIPAM brushes above the lower critical solution temperature of 32°C. They also provide a plausible mechanistic

understanding of protein interactions with end-grafted PNIPAM films. Adsorbed protein levels were below the detection limit of ellipsometry, and required the use of isotope labeled protein for quantification. Differences in the low levels of adsorbed protein depended on the grafting density and, in part, on molecular weight. Dense brushes prevent protein penetration, and protein also does not adsorb at the outer edge of dense brushes. However, proteins adsorb to more dilute brushes that allow proteins to penetrate the layer and interact more extensively with the grafted chains. These findings suggest that protein adsorption above the LCST is determined by the capacity of proteins to penetrate PNIPAM brush layers and interact extensively with the chains, rather than on the collapsed configuration of chains.

4.5 References

1. Galaev, I. Y., Mattiasson, B., Trends Biotechnol, 1999, 17, 335-340.
2. Hoffman, A. S., Artif Organs, 1995, 19, 458-467.
3. Stayton, P. S., Shimoboji, T., Long, C., Chilkoti, A., Chen, G., Harris, J. M., Hoffman, A. S., Nature, 1995, 378, 472-474.
4. Ayano, E., Okada, Y., Sakamoto, C., Kanazawa, H., Kikuchi, A., Okano, T., J. Chromatogr. A, 2006, 1119, 51-57.
5. Idota, N., Kikuchi, A., Kobayashi, J., Akiyama, Y., Sakai, K., Okano, T., Langmuir, 2006, 22, 425-430.
6. Kanazawa, H., Matsushima, Y., Okano, T., Trends Anal. Chem., 1998, 17, 425-440.
7. Yamanaka, H., Yoshizako, K., Akiyama, Y., Sota, H., Hasegawa, Y., Shinohara, Y., Kikuchi, A., Okano, T., Anal. Chem., 2003, 75, 1658-1663.
8. Kanazawa, H., Nishikawa, M., Mizutani, A., Sakamoto, C., Morita-Murase, Y., Nagata, Y., Kikuchi, A., Okano, T., J. Chromatogr. A, 2008, 1191, 157-161.
9. Mizutani, A., Nagase, K., Kikuchi, A., Kanazawa, H., Akiyama, Y., Kobayashi, J., Annaka, M., Okano, T., J. Chromatogr. A, 2010, 1217, 5978-5985.

10. Mizutani, A., Nagase, K., Kikuchi, A., Kanazawa, H., Akiyama, Y., Kobayashi, J., Annaka, M., Okano, T., J. Chromatogr. B Analyt. Technol. Biomed. Life Sci., 2010, 878, 2191-2198.
11. Mizutani, A., Nagase, K., Kikuchi, A., Kanazawa, H., Akiyama, Y., Kobayashi, J., Annaka, M., Okano, T. ,J. Chromatogr. A, 2010, 1217, 522-529.
12. Franzin, C. M., MacDonald, P. M., Plozova, A., Winnik, F. M., Biochim. Biophys. Acta, 1998, 1415, 219-234.
13. Kono, K., Nakai, R., Morimoto, K., Takagishi, T., FEBS Lett., 1999, 456, 306-310.
14. Yang, J., Yamato, M., Okano, T., Materials Research Society Bulletin, 2005, 30, 189-193.
15. Ohki, T., Yamato, M., Murakami, D., Takagi, R., Yang, J., Namiki, H., Okano, T., Takasaki, K., Gut, 2006, 55, 1704-1710.
16. Shiroyanagi, Y., Yamato, M., Yamazaki, Y., Toma, H., Okano, T., Tissue Eng, 2003, 9, 1005-1012.
17. Shiroyanagi, Y., Yamato, M., Yamazaki, Y., Toma, H., Okano, T., BJU Int., 2004, 93, 1069-1075.
18. Sumide, T., Nishida, K., Yamato, M., Ide, T., Hayashida, Y., Watanabe, K., Yang, J., Kohno, C., Kikuchi, A., Maeda, N., Watanabe, H., Okano, T., Tano, Y., FASEB J., 2006, 20, 392-394.
19. Takagi, R., Murakami, D., Kondo, M., Ohki, T., Sasaki, R., Mizutani, M., Yamato, M., Nishida, K., Namiki, H., Yamamoto, M., Okano, T., Gastrointest. Endosc., 2010, 72, 1253-1259.
20. Tsuda, Y., Kikuchi, A., Yamato, M., Nakao, A., Sakurai, Y., Umezu, M., Okano, T., Biomaterials, 2005, 26, 1885-1893.
21. Washio, K., Iwata, T., Mizutani, M., Ando, T., Yamato, M., Okano, T., Ishikawa, I., Cell Tissue Res., 2010, 341, 397-404.
22. Watanabe, K., Yamato, M., Hayashida, Y., Yang, J., Kikuchi, A., Okano, T., Tano, Y., Nishida, K., Biomaterials, 2007, 28, 745-749.

23. Yaji, N., Yamato, M., Yang, J., Okano, T., Hori, S., Biomaterials, 2009, 30, 797-803.

24. Yakushiji, T., Sakai, H., Kikuchi, A., Aoyagi, T., Sakurai, Y., Okano, T., Langmuir, 1998, 14, 4657-4662.

25. Burkert, S., Bittrich, E., Kuntzsch, M., Muller, M., Eichhorn, K. J., Bellmann, C., Uhlmann, P., Stamm, M., Langmuir, 2010, 26, 1786-1795.

26. Fukumori, K., Akiyama, Y., Kumashiro, Y., Kobayashi, J., Yamato, M., Sakai, K., Okano, T., Macromol. Biosci., 2010, 10, 1117-1129.

27. Akiyama, Y., Kikuchi, A., Yamato, M., Okano, T., Langmuir, 2004, 20, 5506-5511.

28. Fukumori, K., Akiyama, Y., Yamato, M., Kobayashi, J., Sakai, K., Okano, T., Acta Biomater., 2009, 5, 470-476.

29. Canavan, H. E., Cheng, X., Graham, D. J., Ratner, B. D., Castner, D. G., Langmuir, 2005, 21, 1949-1955.

30. Canavan, H. E., Graham, D. J., Cheng, X., Ratner, B. D., Castner, D. G., Langmuir, 2007, 23, 50-56.

31. Plunkett, K. N., Zhu, X., Moore, J. S., Leckband, D. E., Langmuir, 2006, 22, 4259-4266.

32. Zhu, X., Yan, C., Winnik, F. M., Leckband, D. E., Langmuir, 2007, 23, 162-169.

33. Matyajaszewski, K., Miller, P. J., Shukla, N., Immaraporn, B., Gelman, B. B., Luokala, T. M., Siclovan, G., Kickelbick, T., Vallant, H., Hoffmann, H., Pakula, T., Macromolecules, 1999, 32, 8716-8724.

34. Ye, X. D., Lu, Y. J., Shen, L., Ding, Y. W., Liu, S. L., Zhang, G. Z., Wu, C., Macromolecules, 2007, 40, 4750-4752.

35. Zhang, S. H., Chen, Y., Li, H., Weng, Y. X., Chinese Journal of Chemical Physics, 2009, 22, 447-452.

36. de Feijter, J., Benjamins, J., Veer, F., Biopolymers, 1978, 17, 1759-1772.

37. Voros, J., Biophys. J., 2004, 87, 553-561.

38. Mandel, J., The Statistical Analysis of Experimental Data. Interscience Publishers: NY, 1964.

39. Papra, A., Gadegaard, N., Larsen, N. B., Langmuir, 2001, 17, 1457-1460.

40. Yu, K., Wang, H., Xue, L., Han, Y., Langmuir, 2007, 23, 1443-1452.

41. Sindorf, D. W., Maclel, G. E., J. Phys. Chem., 1982, 86, 5208-5219.

42. Sunday, D., Curras-Medina, S., Green, D. L., Macromolecules, 2010, 43, 4871-4878.

43. Tu, H., Heitzman, C. E., Braun, P. V., Langmuir, 2004, 20, 8313-8320.

44. Israelachvili, J., Intermolecular and Surface Forces. 2 ed.; Academic Press: New York, 1992.

45. Halperin, A., Fragneto, G., Schollier, A., Sferrazza, M., Langmuir, 2007, 23, 10603-10617.

46. Yu, Q., Zhang, Y., Chen, H., Wu, Z., Huang, H., Cheng, C., Colloids and Surfaces. B, Biointerfaces, 2010, 76, 468-474.

47. Feldman, K., Hähner, G., Spencer, N. D., Harder, P., Grunze, M., J. Am. Chem. Soc., 1999, 121, 10134-10141.

48. Jenney, C., Anderson, J., J. Biomed. Mater. Res., 1999, 49, 435-447.

49. Yim, H., Kent, M. S., Satija, S., Mendez, S., Balamurugan, S., Balamurugan, S. S., Lopez, G. P., J. Polym. Sci. B, 2004, 42, 3302-3310.

50. Takahashi, H., Nakayama, M., Yamato, M., Okano, T., Biomacromolecules, 2010, 11, 1991-1999.

51. Li, L., Zhu, Y., Li, B., Gao, C., Langmuir, 2008, 24, 13632-13639.

52. Nagase, K., Kobayashi, J., Okano, T., J. R. Soc. Interface, 2009, 6 Suppl 3, S293-309.

53. Baulin, V., Halperin, A., Macromol, Theory Simul., 2003, 12, 549-559.

54. Baulin, V., Zhulina, E. B., Halperin, A., J. Chem. Phys., 2003, 119, 10977-10988.

55. Yim, H., Kent, M. S., Satija, S., Mendez, S., Balamurugan, S. S., Balamurugan, S., Lopez, G. P., Phys. Rev. E Stat. Nonlin. Soft Matter Phys., 2005, 72, 051801.

56. Ayano, E., Nambu, K., Sakamoto, C., Kanazawa, H., Kikuchi, A., Okano, T., J. Chromatogr. A, 2006, 1119, 58-65.

57. Galaev, Y., Galaev, I., Mattiasson, B., Smart polymers for bioseparations and bioprocessing. CRC Press: Lund, Sweden, 2002.

58. Ivanov, A. E., Galaev, I. Y., Kazakov, S. V., Mattiasson, B., J. Chromatogr. A, 2001, 907, 115-130.

59. Aseyev, V., Tenhu, H., Winnik, F. M., Temperature-Dependence of the Colloidal Stability of Neutral Amphiphilic Polymers in Water. Springer-Verlag: Heidelberg, 2006; Vol. 196, p 1-86.

CHAPTER 5

IMPACT OF POLYACRYLAMIDE INVERSE OPAL STRUCTURES ON HUMAN CORNEAL EPITHELIAL CELL BEHAVIOR

The work described in this chapter was performed in collaboration with Dr. Sara J. Liliensiek and Prof. Paul F. Nealey at the University of Wisconsin-Madison.

5.1 Introduction

Tissue engineering is an emerging field for the past few decades and principally focuses on building micro and nanoscaffolds for the construction of tissue-like structures from individual cells. The design and engineering of artificial tissues rely on profound understanding of how individual cells respond to various chemical and physical signals within their microenvironments. In particular, external physical cues play a crucial role in shaping essential cellular functions such as cell differentiation, motility, proliferation and apoptosis. Furthermore, conventional cell culture techniques on two dimensional (2-D) substrates may not appropriately reflect the 3-D microenvironments of extra cellular matrixes [1-4]. Therefore, engineering well-defined 3-D biostructures with desired mechanical, chemical, and biological properties is a tremendous need in the field in order to investigate cell functions vs. surface interactions.

Extra cellular matrixes, on which cells are immobilized within tissue, are comprised of individual components in nano scale. Incorporation of nanotechnology with biology brings new design rules to engineered biomaterials. There has been great advancement in microfabrication technologies to decorate surfaces with sub-micron feature sizes [5]. Successful integration of these techniques to fabricate micro- and nanoscaled biomaterials used in tissue engineering allows researchers to regulate cell microenvironment in culture and to monitor cell response accordingly.

Human corneal epithelial basement membrane is a very porous material (Figure 5. 1) [6]. Its lateral pore size ranges from 21 nm to 191 nm. *In vivo*, human corneal epithelial cells are in contact with such a porous natural substrate. In this chapter, we study the fabrication of 3D

porous biomaterials on solid surfaces with various pore sizes, engineer design parameters of uniform surface porosity on the scaffold surface, and observe human corneal epithelial cell responses such as morphology change and proliferation rate as a function of the surface pore size.

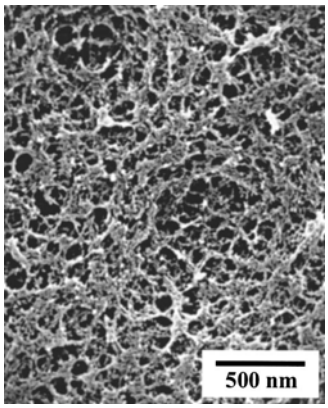

Figure 5. 1. Scanning electron microscopy (SEM) image of the human cornea epithelial basement membrane.

5.2 Experimental

5.2.1 Materials

Polystyrene (PS) colloid solutions with various sizes were purchased from Interfacial Dynamics. Acrylamide (AAm), diethoxyacetophenone, polyisobutylmethacrylate (PIBMA), 3-(trimethoxysiyl)propyl methacrylate were purchased from Acros. Methylmethacrylate was purchased from Aldrich and purified by passing through an inhibitor remover column to remove monomethyl ether hydroquinone. Acrylamidopropyl trimethyl ammonium chloride was purchased from Aldrich and used as received. Bisacrylamide was purchased from ICN biomedicals.

5.2.2 Constructing 3D Porous Polyacrylamide Hydrogel

5.2.2.1 Preparation of the Flow Cell

PS colloids were crystallized in a flow cell that was generated by a non-lithographic preparation method (Figure 5. 2) [7]. Two glass slides with specific functionalities were brought together by sandwiching a 12-micron-thick Mylar film (Dupont) that has been cut into a 1 inch square outline 2 mm wide between two glass slides. All of the fabrication processes, including the crystallization of PS colloids, backfilling the crystal with monomer mixture (a solution of AAm, photoinitiator, crosslinker), and photopolymerization of monomer mixture, were generated in the fabrication area which was an empty space between two glass slides. In this flow cell assembly, both top and bottom glasses were functionalized or coated with particular chemistries. The top glass was functionalized with 3-(trimethoxysiyl)propyl methacrylate (2% in toluene) overnight and washed with isopropyl alcohol before the flow cell assembly. The surface of the bottom glass was chemically modified by growing polymethylmethacrylate (PMMA) brushes by following a protocol from the literature [8]. Then, PIBMA solution in toluene was spun-cast on the PMMA brushes. The top glass had a 2 mm hole drilled in it and a glass tube (feeding tube) was attached to the top glass from the back side of the PIBMA coated surface. Before assembling the flow cell, the Mylar film was dipped into a dilute (0.08% PS colloids in water/ethanol, 3/1 (v/v)) solution of colloids. Finally, the flow cell was assembled by bringing these two glass slides together and the assembly was held together by a set of four paper clips.

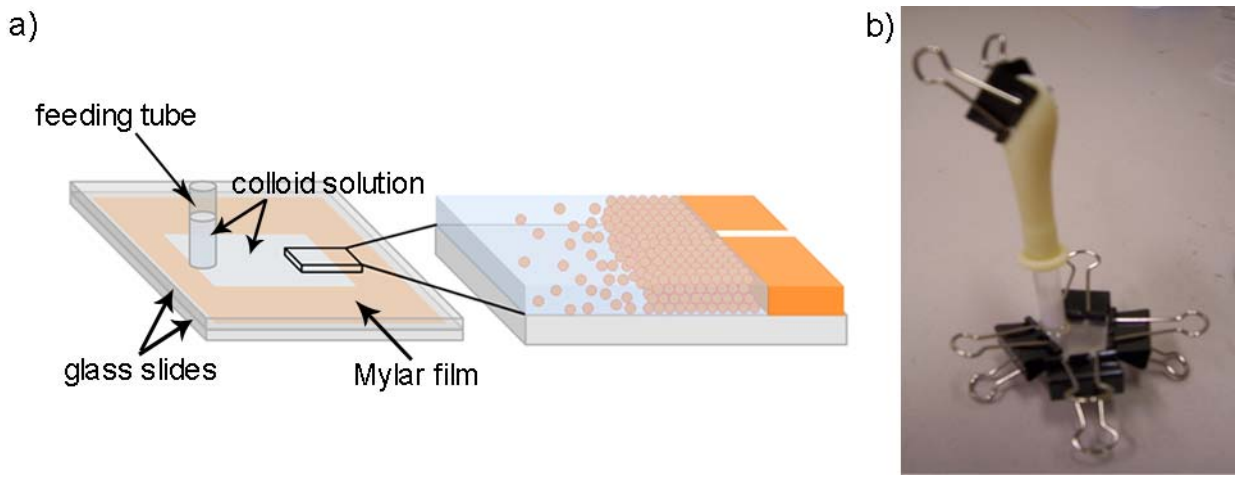

Figure 5. 2. (a) Schematic illustration of the flow cell assembly for PS colloidal crystallization. (b) Optical image of a sample flow cell.

5.2.2.2 Crystallization of PS Colloids and Hydrogel Preparation

PS colloids solution (2% in water) was added to the feeding tube. The tube was covered with a rubber bulb. The flow cell was placed on top of a sonicator. As water leaved the cell from the sides, the colloids crystallized in the fabrication area. Once PS colloid crystal filled the whole fabrication area, the excess colloid solution was removed from the feeding tube and the flow cell was placed in a desiccator for drying. The dry PS colloidal crystal was then backfilled with a solution of AAm (45.9%), bisacrylamide (3.8%), diethoxyacetophenone (0.4%), acrylamidopropyl trimethyl ammonium chloride (4%), water (22.95%), and ethanol (22.95%). AAm was polymerized with UV light (40 min) using a 100-W shortwave UV mercury lamp (UVP, B-100A). Next, the flow cell was disassembled. The top glass had PAAm hydrogel with PS colloids. It was placed in chloroform for 1 hour to dissolve PS colloids. Finally, the bottom glass was stored in 5% ethanol solution in water for the cell studies.

5.2.3 Human Corneal Epithelial Cells (HCECs) Harvest and Culture

Telomerase-immortalized human corneal epithelial cells were a generous gift from Dr. James Jester at the University of California, Irvine [9]. HCECs were cultured in epithelial

medium containing a 3:2 ratio of Ham's F12:Dulbelco's Modified Eagles medium (DMEM), supplemented with 2.5% (v/v) fetal bovine serum (FBS), 0.4 μg/mL hydrocortisone, 8.4 ng/mL cholera toxin, 5 μg/mL insulin, 24 μg/mL adenine, 10 ng/mL epidermal growth factor, 100 units penicillin, and 100 μg/mL streptomycin [10, 11]. HCECs were plated into 100 mm tissue culture plates containing a mitomycin-c treated Swiss 3T3 fibroblast layer. HCECs, between passages 45 and 60, were incubated at 37°C and 5% CO_2 until they reached approximately 70% confluence. For all experiments, 3 to 5 substrates were used and HCECs were plated at a density of $3x10^5$. Cells were incubated for 24 hours after plating to allow for cell attachment and toxicity tests.

5.2.4 HCECs Immunocytochemistry and Attachment on 3D Porous Surfaces

HCECs were stained for actin-filaments and the nuclei. After 24 hours of incubation, the surfaces were rinsed with 1x PBS buffer. Substrates were fixed in 4% paraformaldehyde–PBS (Electron Microscopy Sciences, PA) at room temperature for 20 min and then washed with 1x PBS buffer. HCECs were permeabilized with 0.1% (v/v) Triton X-100 (Sigma-Aldrich, MO) in 1x PBS for 7 min, washed in 1x PBS and soaked in 1% (w/w) bovine serum albumin (Sigma-Aldrich, MO) in 1x PBS for 20 min. They were rinsed with 1x PBS for 10 min and incubated with 5 μg/mL of TRITC-phalloidin (Sigma-Aldrich, MO) containing 0.1 μg/mL 4',6-Diamidino-2-phenylindole (DAPI) (Invitrogen, CA) in 1x PBS for 40 min, to label both filamentous actin (red), and the nucleus (blue). After a final rinse with 1x PBS, surfaces were coverslipped using DABCO® (Fluka, Switzerland), an anti-fading mounting medium, and sealed with clear nail polish. A minimum of six areas per substrate were imaged using a Zeiss Axiovert 100 microscope at 10x magnification. The average cell number and cell area for HCECs were obtained for each topographically patterned porous substrate using Axiovision software. Statistical analysis includes analysis of variance followed by a Student's t-test to determine statistical significance.

5.2.5 HCECs Morphology on 3D Porous Surfaces

For high resolution imaging of HCECs on our porous substrates, cells were plated for 24 hours onto each substrate using the protocol described previously. After 2 gentle rinses with 0.1 M Sorensons phosphate buffer, HCECs were fixed in fresh Karnofsky's-1% tannic acid fixative for 20 min. Then, substrates were rinsed twice with 0.1 M Sorensons phosphate buffer. Finally, they were immersed in ethanol solutions (in H_2O) with 10%, 15%, 20%, 30%, 50%, 70%, 80%, 90%, 100% (v/v) for 3 min. Before drying samples, they were soaked in HDMS for 10 min. SEM images of HCECs on porous PAAm hydrogels were taken.

5.3 Results and Discussion

5.3.1 Impact of Flow Cell Surface Functionality on Generation of Uniformly Porous Surfaces

The PS colloidal crystallization utilizing the flow cell assembly method required surface functionalization of the glass components with hydrophilic and hydrophobic chemistries [12]. In this method, any defects or gap between the PS crystal and the bottom glass (Figure 5. 3a) is filled with the monomer mixture as the monomer solution was introduced to the crystal. Once monomer was polymerized, this gap would be replicated to closed surface topography. Therefore, the surface porosity of the crosslinked hydrogel will be non-uniform across the surface such that some areas had uncontrolled closed surface topography (Figure 5. 3b). The problem described above is the most significant challenge in constructing 3D porous materials with uniform and flawless surface porosity.

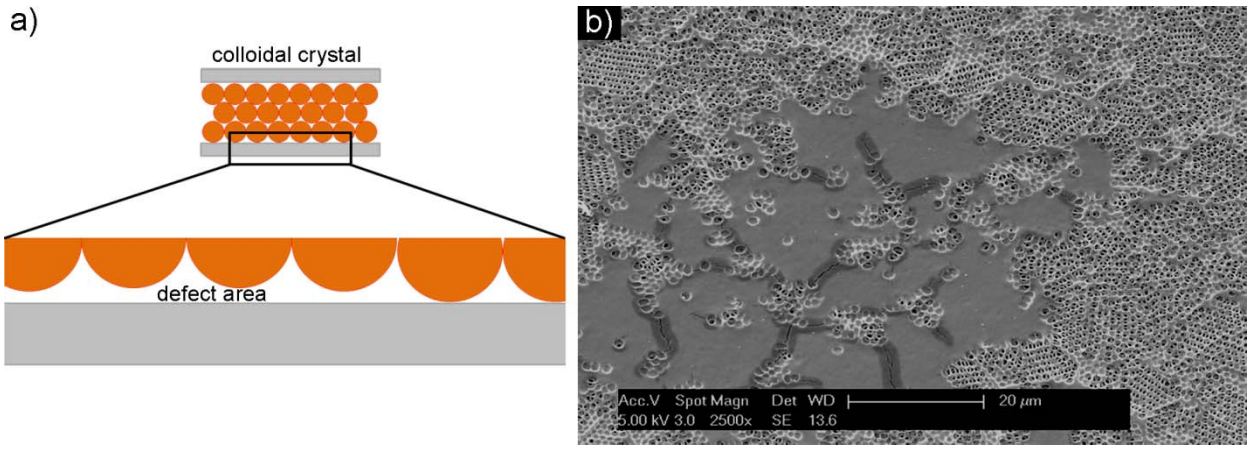

Figure 5. 3. (a) Schematic illustration of surface defects in the 3-D PS colloidal crystals. (b) SEM image of hydrogel surface (top view). Dark and smooth regions have undesired nonporous-closed topographies.

The flow cell should be designed such that the defects in the bottom glass-PS crystal interface can be minimized. For this reason, the bottom glass was coated with a thin layer of a polymer film (PIBMA) and PS colloids were crystallized on top of this thin film. After the crystal was annealed at 90ºC, PIBMA film got softened due to its lower glass transition temperature (65ºC) thereby immersing the first layer of PS colloids in the PIBMA film. The film thickness was only 20% of the colloid particle diameter (Figure 5. 4).

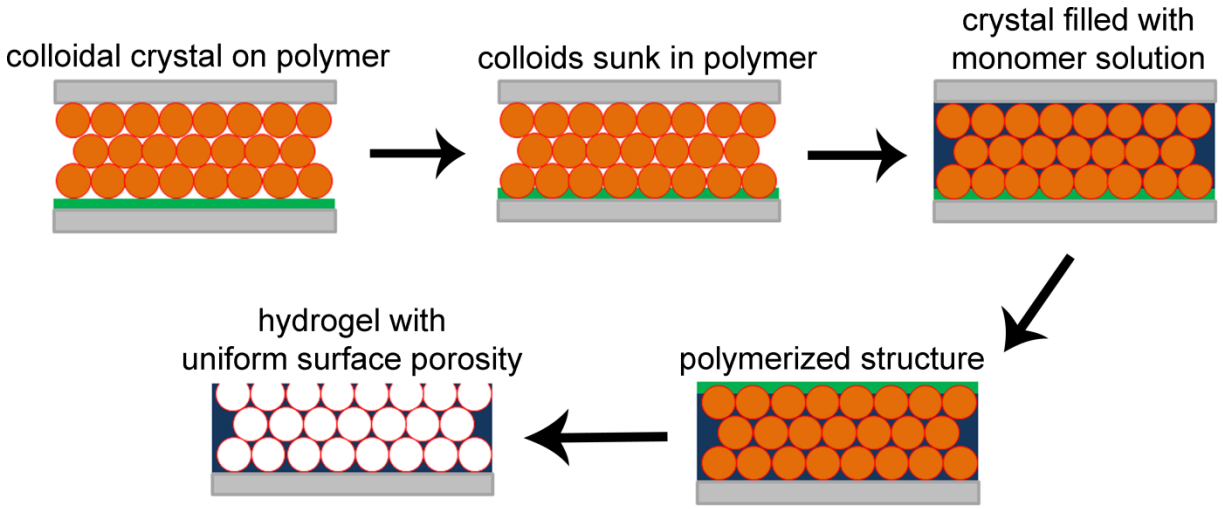

Figure 5. 4. Illustration of engineering the uniform surface porosity of the 3D hydrogel surfaces.

There are some limitations in templating the first layer of PS colloids in the PIBMA film. One of the issue is that the PIBMA film cracks randomly during the colloidal crystallization.

These cracks would expose the surface beneath the PIBMA film to the aqueous colloid solution and disrupt proper colloid crystallization (Figure 5. 5). Figure 5. 6 shows the surface and the cross-sectional images of the hydrogel in the presence of PS colloids immediately after photopolymerization. In this case, the gap at the interface between the PIBMA film and the bottom glass surface resulted in uneven surface topographies on the hydrogel surface.

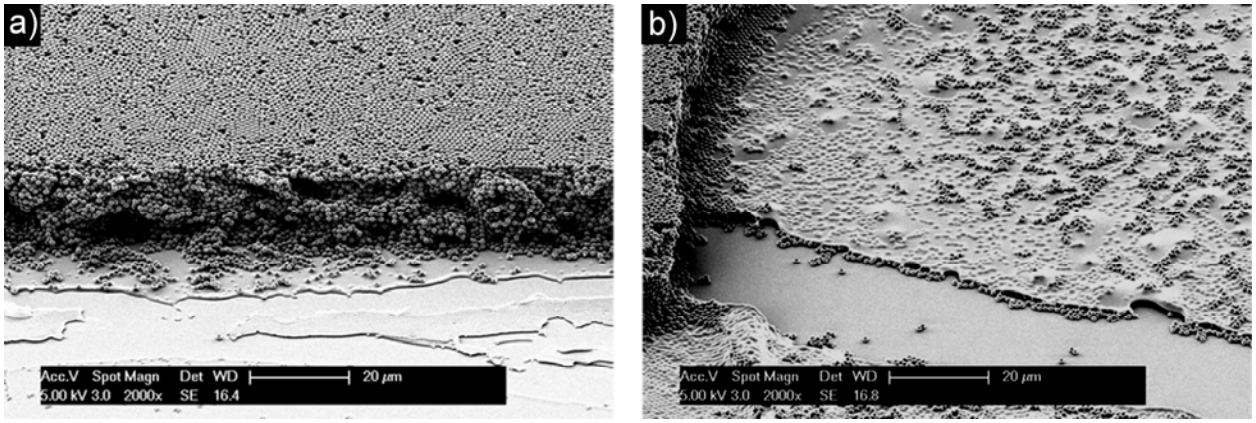

Figure 5. 5. SEM images of PS colloids on PIBMA film. (a) Cross-sectional image of PS colloidal crystal on PIBMA film. (b) Aqueous PS colloid solution wetted the bottom glass resulting colloid aggregation underneath the PIBMS film.

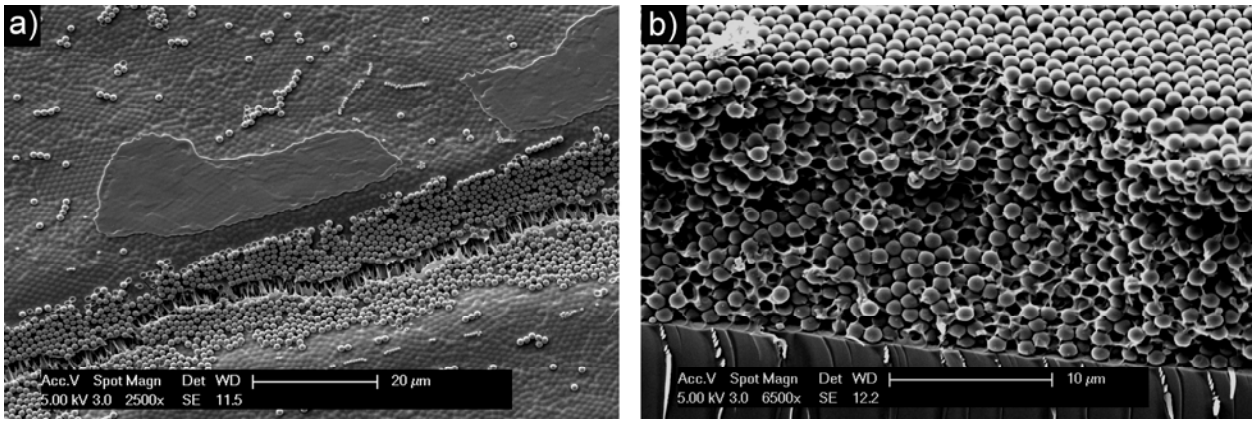

Figure 5. 6. SEM images of a top glass with hydrogel and PS colloids after photopolymerization, (a) top surface and (b) cross-section. In (a), PIBMA film remained on the hydrogel surface and part of the PS colloids is localized at the interface between PIBMA film and the bottom glass. In (b), a single layer of PS colloids localized underneath the PIBMA film is observed.

To minimize wettability of the bottom glass with the aqueous colloid solution and the monomer mixture, the surface of the bottom glass underneath the PIBMA coating should be

relatively hydrophobic. The surface was chemically modified by growing PMMA brushes in order to obtain a more hydrophobic surface. Generally, octadecyltrichlorosilane (OTS) chemistry has been widely used to obtain highly hydrophobic surfaces [13, 14]. However, it was not practical to coat PIBMA film on an OTS functionalized surface due to the poor wettability of PIBMA solution on this surface (despite using various organic solvents). The contact angle measurements of monomer mixture on various surfaces were summarized in Figure 5. 7. The smaller contact angle values suggest that aqueous monomer mixture wetted a hydrophilic surface more easily than a hydrophobic surface.

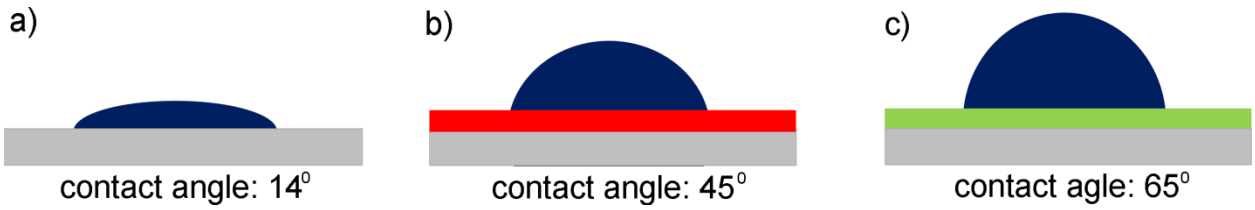

Figure 5. 7. Schematic representation of wetting of the monomer mixture (blue) of (a) a hydrophilic surface (piranha cleaned), (b) a hydrophobic surface with PMMA brush functionality (red), (c) a PIBMA film (green).

Apart from the surface chemistry of the bottom glass, uniformity of the PIBMA coating played a vital role in templating the PS colloids and generating defect free porosity at the hydrogel surface. Any defect or non-uniformity in the PIBMA coating would yield nonporous regions at the hydrogel surface. We also observed that the solvent selection for spin-casting the PIBMA film was extremely critical in obtaining a uniform PIBMA film on PMMA brushes. Figure 5. 8a shows the surface of the PIBMA film that was cast using chloroform solution. The coating was non-uniform with many circular regions due to fast solvent evaporation. When such coating was used in porous hydrogel preparation, non-uniformity in PIBMA film coating was transferred onto the hydrogel surface topography as depicted in Figure 5. 8b.

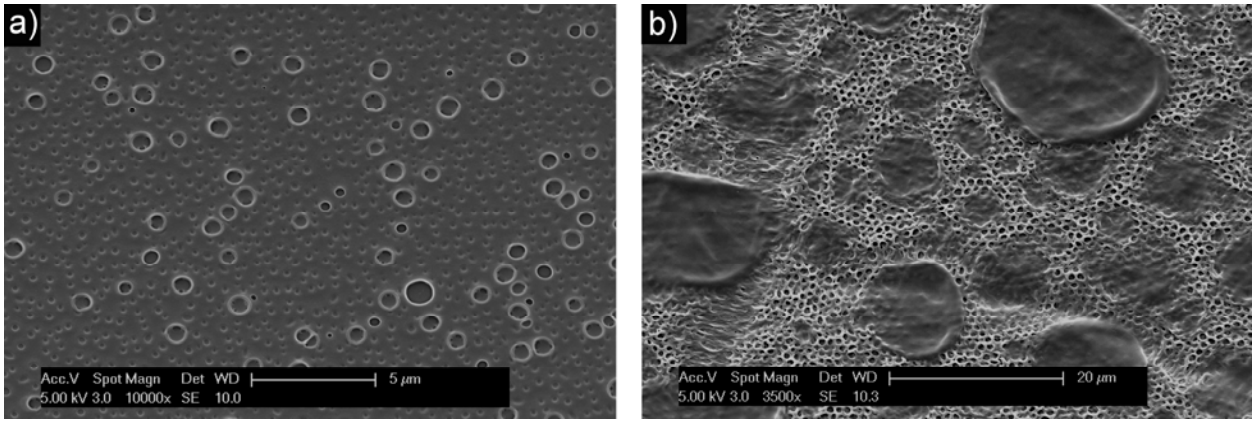

Figure 5. 8. SEM images of (a) the PIBMA film that was spun-cast from chloroform solution and (b) the surface of the hydrogel that was replicated from an uneven PIBMA coating (from chloroform solution).

The best solvent we have tested was toluene resulting in flat and uniform PIBMA film surfaces. The first layer of the PS colloids in the crystal was successfully templated on the PIBMA film (regions inside the red circles in Figure 5. 9). Figure 10 shows SEM images of successful PS colloid crystals on PIBMA film. In Figure 5. 11, cross-sectional SEM images of crosslinked hydrogels in PS colloidal crystals with various particle diameters (450 nm, 1 μm, and 4 μm) were shown. Once colloids were washed away with organic solvent, we obtained 3D porous hydrogels with uniformly porous surfaces (Figure 5. 12).

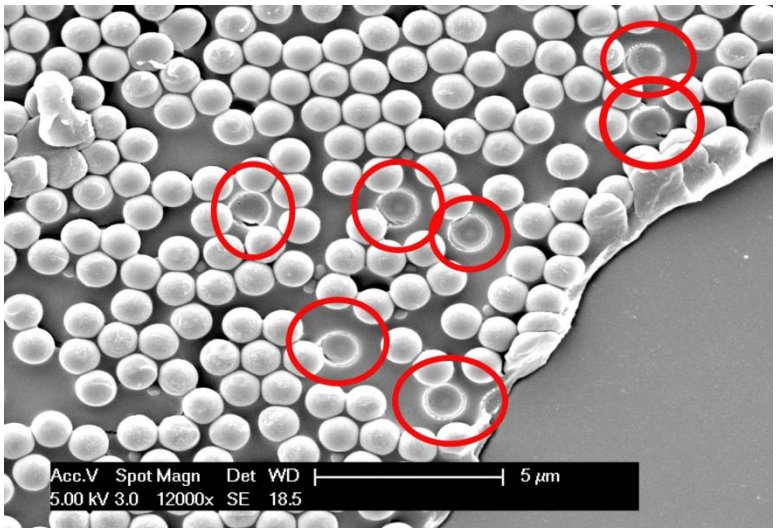

Figure 5. 9. SEM image of 1 μm PS colloids templated on the PIBMA film after annealing.

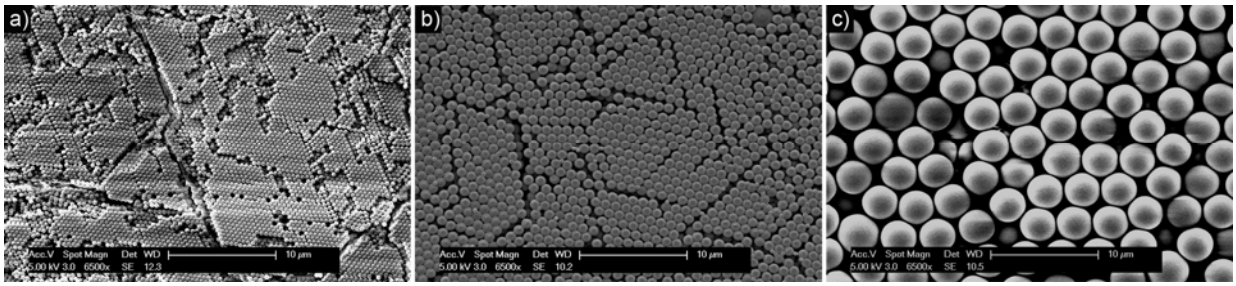

Figure 5. 10. SEM images (top view) of PS colloidal crystals with (a) 450 nm, (b) 1 μm, and (c) 4 μm diameter particles.

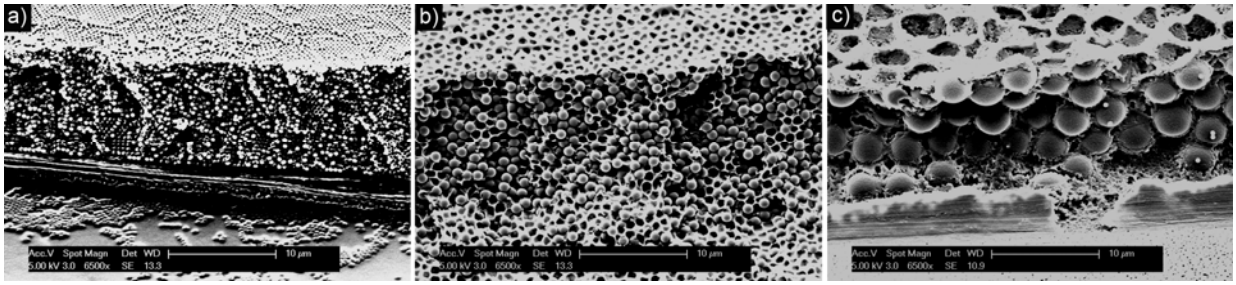

Figure 5. 11. SEM images of crosslinked hydrogels in PS colloidal crystal with (a) 450 nm, (b) 1 μm, and (c) 4 μm diameter particles (in cross-section).

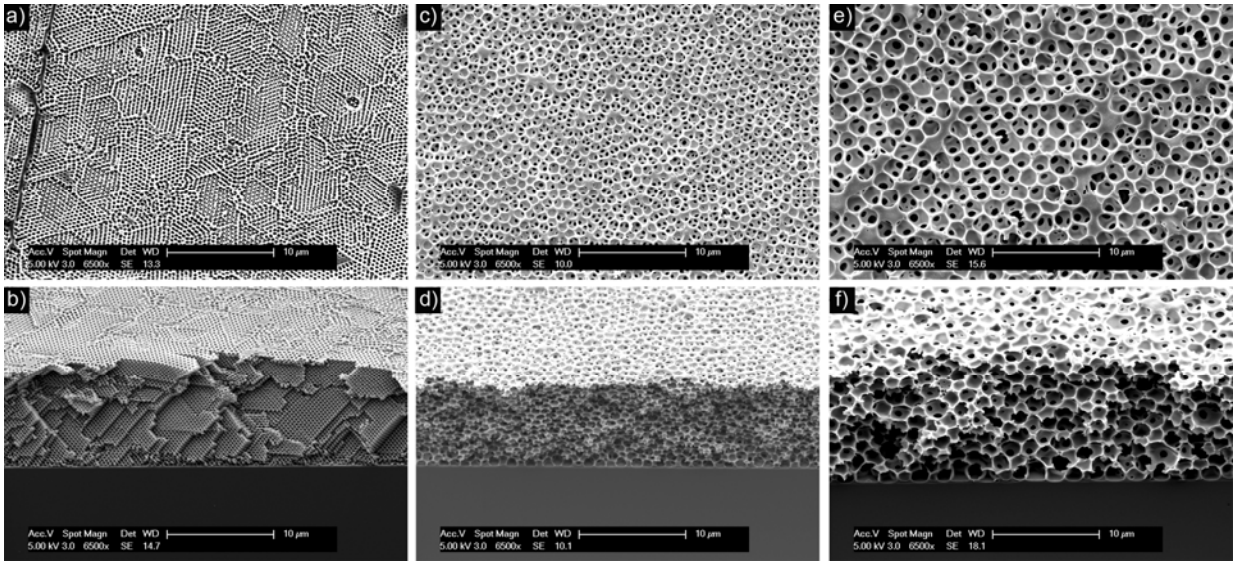

Figure 5. 12. SEM images of 3-D hydrogel structures with uniformly porous surfaces (top row) and cross-sections (bottom row) with (a, b) 450 nm, (c, d) 1 μm, and (e, f) 4 μm pore sizes.

5.3.2 HCECs Behavior as a Function of Pore Size of 3D Porous Biomaterials

Topographic cues have been shown to control cell behavior by many research groups along with other external stimuli. In order to better understand the effect of the topography of the

human corneal basement membrane on HCECs function, HCECs were cultured on 3D porous PAAm hydrogel surfaces with surface porosity ranging between 450 nm and 4 μm. Control experiments were performed on non-porous (flat) PAAm hydrogels.

Figure 5. 13 demonstrates that porous PAAm hydrogels supported HCECs adhesion. The flat PAAm samples also provided a nice platform for initial cell attachment and area studies. The HCECs adhesion on such surfaces was promoted by incorporation of acrylamidopropyl trimethyl ammonium chloride to the hydrogel structure [15]. The fluorescence images showed deep cracks on the 450 nm porous hydrogel whereas 1 μm porous PAAm was much more stable and crack free throughout the cell culture studies (Figure 5. 13 c-f). Even though the crosslinking densities and the monomer compositions in both materials were the same, the resulting difference in the hydrogel stability can be explained by variation in elastic properties due to different pore sizes.

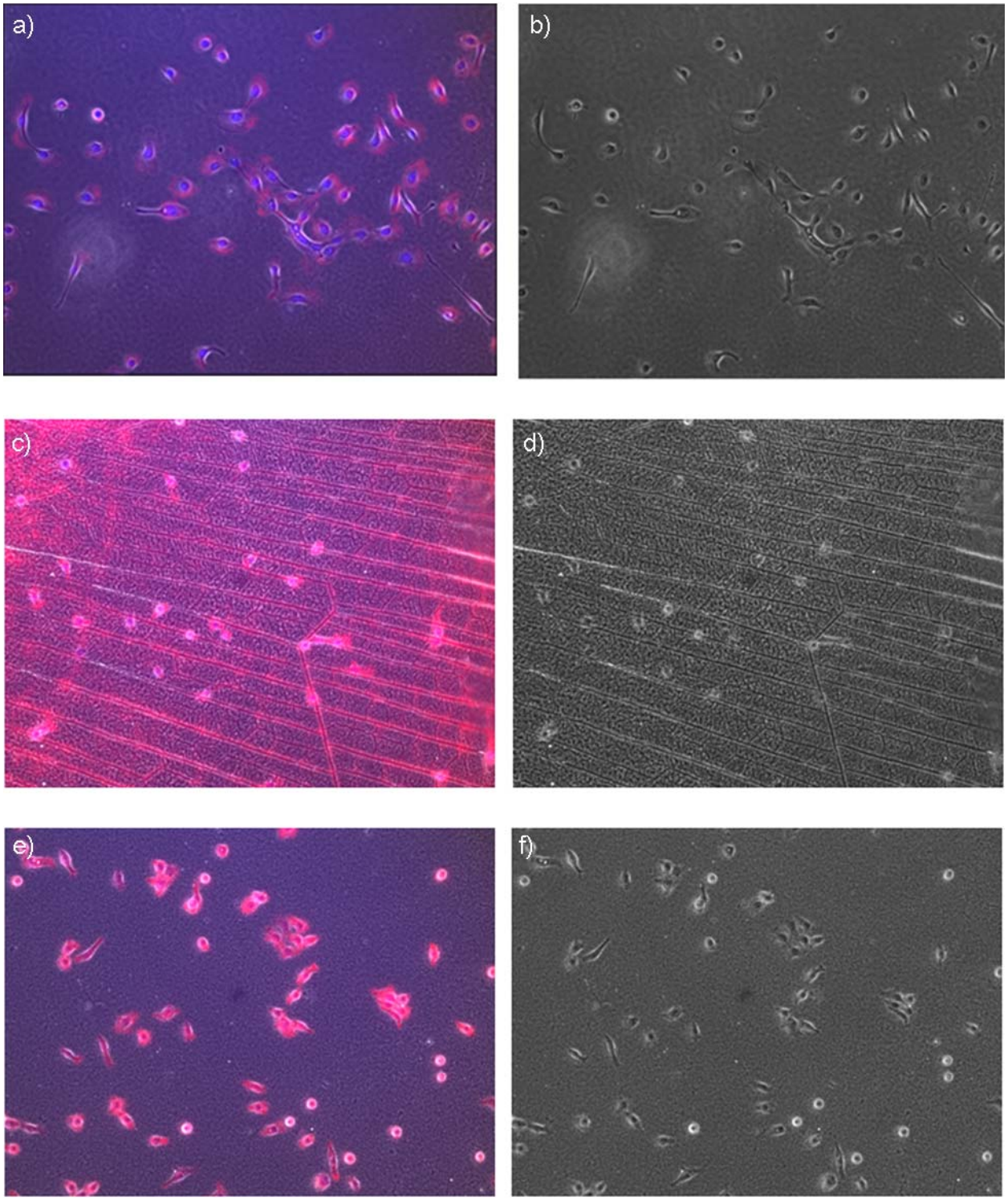

Figure 5. 13. Fluorescence images of HCECs plated on (a, b) flat, (c, d) 450 nm, and (e, f) 1 μm porous hydrogels. Nuclei were stained with DAPI and the cytoskeleton was stained with actin-phalloidin (a) or rhodamine (c, d). Phase images (b, d, and f) of the same regions are shown on the right panels.

We investigated HCECs morphology on porous surfaces. SEM images revealed that HCECs possessed elongated cell morphology on all types of pore size (Figure 5. 14). Cell extensions, lamellipodia, penetrated through the depth of the structure to some extent, although the SEM imaging was limited in identifying the depth of the lamellipodia interaction within the thickness of the hydrogel. The surface topography of 450 nm porous hydrogel was extensively distorted during the sample preparation. Similar but less prominent deformation of the 4 μm porous sample was also observed.

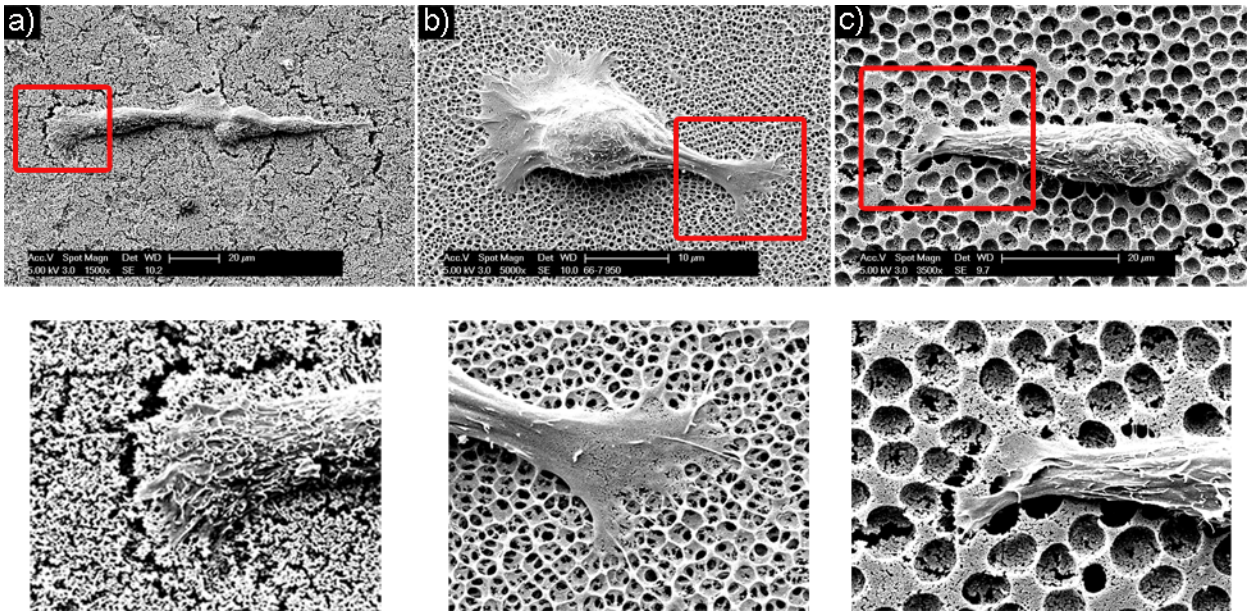

Figure 5. 14. SEM images of HCECs morphologies on 3D porous hydrogels with (a) 450 nm, (b) 1 μm, (c) 4 μm pore size. Images at the bottom row show the red box region at a higher magnification.

HCECs attachment behavior in terms of average cell number and the area on porous hydrogels was studied by using 3 different sample sets. We obtained very similar results from each test. Representative images are shown in Figure 5. 15. HCECs count and total cell area on various surfaces did not show a significant difference as a function of surface porosity. 450 nm porous surfaces were slightly prone to support lower number of cells compared to surfaces that consist of larger pore size and non-porous (flat) controls. This finding is not in good agreement with the porosity range of human corneal epithelial basement membrane where

porosity ranges between 21 nm and 191 nm. Earlier work has demonstrated that the topographical cues were in conjunction with soluble factors [16, 17]. Clearly, more detailed investigations taking the soluble factors into account are required in the future. Furthermore, further studies on the proliferation rate of HCECs as a function of pore dimension will be notable to demonstrate topography influence on HCECs behavior.

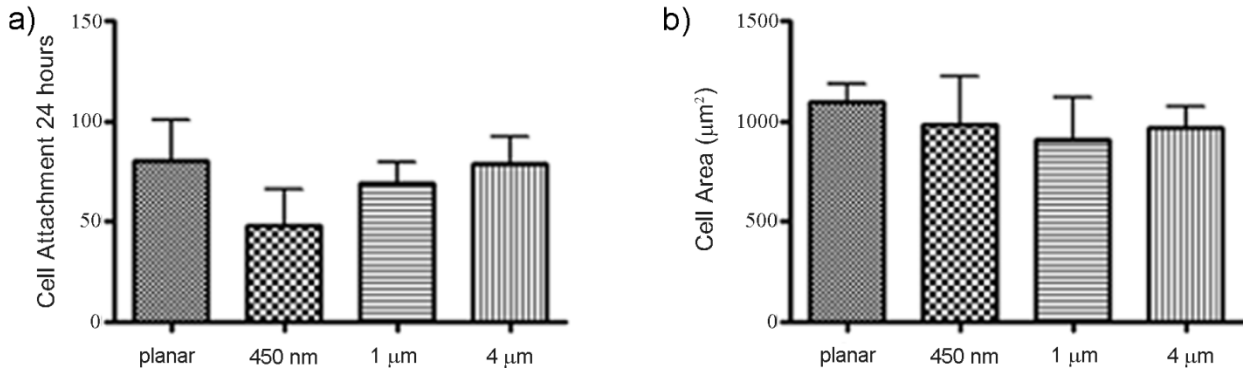

Figure 5. 15. HCECs behavior response on porous surfaces as (a) average number of cells and (b) average area that cells spread.

5.4 Conclusions

In conclusion, we have demonstrated that 3D porous hydrogels can be fabricated by the colloidal crystal templating method. Defects at the surface of the porous materials appearing as closed surface topography were eliminated by templating the first layer of colloids in a thin polymer film. The hydrogel porosity ranging from 450 nm to 4 μm was obtained by using colloidal particles with various sizes. PAAm chemistry was found to be non-toxic and provide a good support for HCECs growth. HCECs grew on porous PAAm surfaces assumed an elongated form. Finger like cell extensions, lamellipodia, were observed to penetrate into the porous surface. However, HCECs did not show any notable difference in cell counts and cell spread area as a function of substrate pore size. The future direction of this work is the study of HCECs function on surfaces with smaller pore size.

5.5 References

1. Lee, J., Cuddihy, M. J., Kotov, N. A., Tissue Eng. Part B-Rev., 2008, 14, 1, 61.
2. Phillips, J. A., Vacanti, C. A., Bonassar, L. J., Biochem. Biophys. Res. Commun., 2003, 312, 3, 725.
3. Dar, A., Shachar, M., Leor, J., Cohen, S., Biotechnol. Bioeng., 2002, 80, 3, 305.
4. Hutmacher, D. W., Ng, K. W., Kaps, C., Sittinger, M., Klaring, S., Biomaterials, 2003, 24, 24, 4445.
5. Whitesides, G. M., Ostuni, E., Takayama, S., Jiang, X. Y., Ingber, D. E., Annu. Rev. Biomed. Eng., 2001, 3, 335.
6. Teixeira, A. I., Abrams, G. A., Murphy, C. J., Nealey, P. F., J. Vac. Sci. Technol. B, 2003, 21, 2, 683.
7. Lu, Y., Yin, Y. D., Gates, B., Xia, Y. N., Langmuir, 2001, 17, 20, 6344.
8. Moh, L C H., Langmuir, 2011, 27, 7, 3698.
9. Robertson, D. M., Li, L., Fisher, S., Pearce, V. P., Shay, J. W., Wright, W. E., Cavanagh, H. D., Jester, J. V., Invest Ophthalmol. Vis. Sci. 2005, 46, 2,470.
10. Allenhoffmann, B. L., Rheinwald, J. G., Proc. Natl. Acad. Sci. USA, 1984, 81, 24, 7802.
11. Sabatini, L. M., Allenhoffmann, B. L., Warner, T. F., Azen, E. A., In Vitro Cellular & Developmental Biology, 1991, 27, 12, 939.
12. Barry, R. A., Wiltzius, P., Langmuir, 2006, 22, 3, 1369.
13. Rabinovich, Y. I., Yoon, R. H., Langmuir, 1994, 10, 6, 1903.
14. Flinn, D. H., Guzonas, D. A., Yoon, R. H., Colloid Surf. A-Physicochem. Eng. Asp., 1994, 87, 3, 163.
15. Pelham, R. J., Wang, Y. L., Proc. Natl. Acad. Sci. U.S.A., 1997, 94, 25, 13661.
16. Tocce, E. J., Smirnov, V. K., Kibalov, D. S., Liliensiek, S. J., Murphy, C. J., Nealey, P. F., Biomaterials, 2010, 31, 14, 4064.

17. Teixeira, A. I., McKie, G. A., Foley, J. D., Berticsc, P. J., Nealey, P. F., Murphy, C. J., Biomaterials, 2006, 27, 21, 3945.

CHAPTER 6

CONCLUSIONS

In this thesis, solid surfaces were modified with patterned and non-patterned polymer brushes as well as 3D porous biomaterials. Each class of functional surfaces was utilized to direct the transportation of chemical species and to guide the motility of biological species.

Diffusive transport of 8-hydroxypyrene-1,3,6-trisulfonic acid trisodium salt (HPTS) was directed by patterns of poly(oligoethylene glycol) acrylate (POEGA) brushes in a molecular device with the singular channel μfluidic. A non-lithographic fabrication method for building the μfluidic device improved control over the directed HPTS diffusion along the POEGA patterns. HPTS concentration was found to have a huge impact on imaging analysis. Calculations of HPTS diffusivity in the POEGA brushes revealed that HPTS had a much slower diffusion in the swollen brushes than for free diffusion in solution.

Similar molecular device set up was adapted to study directed diffusive transport of $AuCl_4^-$, and Cu^{2+} ions. In this device, two μfluidic channels were fabricated so that one can support metal ion solution while the other can be reservoir for the reducing agent solution which was $NaBH_4$. Directed diffusion of two reactive ions, metal ion and reducing agent, was obtained in the direction of coming towards one another along the linear pattern of POEGA brushes. Dark field microscopy further proved the presence of nanoparticles as a result of the reduction reaction of metal ions with reducing agent.

Poly(*N*-isopropylacrylamide) (PNIPAM) brushes were fabricated on solid surfaces via surface-initiated atom transfer radical polymerization technique. Protein adsorption characteristics of PNIPAM brushes were studied as a function of grafting density, molecular weight and temperature. Ellipsometry and contact angle measurements revealed that PNIPAM exhibit collapsed configuration above its LCST for dense PNIPAM chains but does not show this

configuration change for lower grafting densities. Protein adsorption on the most hydrophobic and most dense PNIPAM brushes was not observed above its LCST by ellipsometry measurements. These findings were in agreement with qualitative fluorescence microscopy images. Adsorption studies with the use of isotope labeled protein indicated very small amount of protein adsorption on the dense PNIPAM brushes above its LCST. Interestingly, higher amount of protein adsorption was found on the least dense PNIPAM brushes above its LCST. This suggests that very small amount of protein adsorption on PNIPAM brushes above its LCST takes place as the protein molecules penetrate into the PNIPAM brushes rather than the collapsed configuration.

3D porous polyacrylamide hydrogels were prepared by colloidal crystal templating technique. A fabrication method which was templating colloids on a thin polymer film was developed to improve closed surface topographies. Thus, a uniform surface porosity across the surface of the 3D porous hydrogel was obtained. The porosity variation in the polyacrylamide hydrogel was generated by using various sized colloidal particles. Human corneal epithelial cells (HCECs) were grown on the porous polyacrylamide surfaces. Fabricated porous materials were non-toxic for HCECs and cell morphologies on these hydrogels were found to be elongated form. Cell attachments and cell area studies as a function of the pore size showed that pore size does not have a significant effect on these cell behaviors.

AUTHOR'S BIOGRAPHY

Nihan Yonet-Tanyeri was born on March 21, 1981 in Istanbul-Turkey. She grew up in Istanbul and graduated from Fatih University with a B.S. in Chemistry in 2002. She attended the Istanbul Technical University for her graduate education and received her Master's degree in Polymer Science and Technology in 2004. She continued to pursue her Ph. D. education at the same university until she made the biggest change in her life to marry Melikhan Tanyeri and decided to move to Illinois in May 2006. She was fortunate enough to start her graduate education in Prof. Paul V. Braun's group at University of Illinois at Urbana-Champaign in June 2006. Upon completion of her graduate degree, she will be a postdoctoral research fellow in the Chemical and Biomolecular Engineering Department at the University of Illinois at Urbana-Champaign to work with Prof. Hyunjoon Kong.